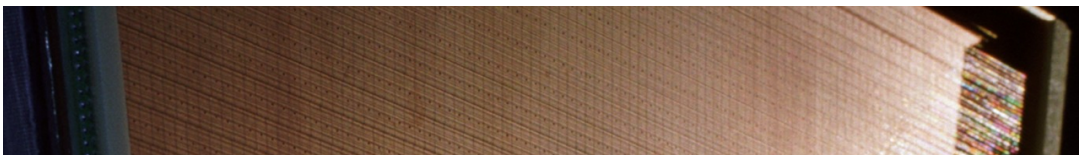

Studies and Mitigation of Space-Charge Distortions in the ALICE TPC in LHC Run 2

Dissertation
zur Erlangung des Doktorgrades
der Naturwissenschaften

vorgelegt beim Fachbereich Physik
der Johann Wolfgang Goethe-Universität
in Frankfurt am Main
von

Ernst Hellbär
aus Dshambul, Kasachstan

Frankfurt am Main 2023
(D 30)

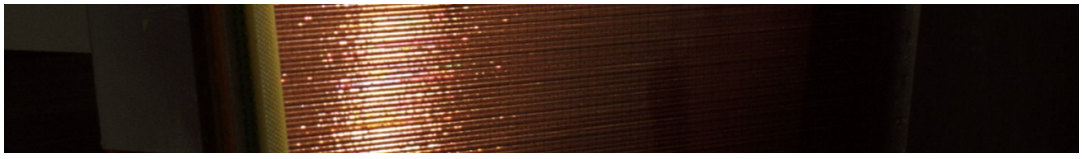

Vom Fachbereich Physik der

Johann Wolfgang Goethe-Universität als Dissertation angenommen.

Dekan:

Prof. Dr. Roger Erb

Gutachter:

Prof. Dr. Harald Appelshäuser

Prof. Dr. Christoph Blume

Datum der Disputation: 18.12.2023

Zusammenfassung

Die Forschung von ALICE (*A Large Ion Collider Experiment*) am CERN (*Conseil Européen pour la Recherche Nucléaire*) befasst sich mit der Untersuchung stark wechselwirkender Materie unter extremen Bedingungen, wie sie nur wenige Mikrosekunden nach dem Urknall existierten. Hierbei handelt es sich um Temperaturen, die mehr als neun Größenordnungen höher sind als die Oberfläche unserer Sonne. Unter solchen Bedingungen wird ein Übergang zu einem Zustand erreicht, in dem die Konstituenten von Nukleonen, die sogenannten Quarks und Gluonen, nicht mehr zu Hadronen gebunden sind, sondern sich frei in einem Quark-Gluon-Plasma (QGP) bewegen können.

Die Bausteine und Wechselwirkungen aller bis heute bekannten Materie werden vom Standardmodell der Teilchenphysik mit erstaunlicher Präzision beschrieben. Hierbei unterteilt man die Elementarteilchen in die zwei Kategorien Fermionen und Bosonen. Die Vektorbosonen sind die Austauschteilchen der fundamentalen physikalischen Kräfte. Die starke Wechselwirkung wird über das masselose Gluon (g) vermittelt, die elektromagnetische Wechselwirkung über das masselose Photon (γ) und die schwache Wechselwirkung über die massiven $W^{\pm}$ und Z Bosonen. Für hohe Energieskalen zeigt sich, dass die elektromagnetische und die schwache Wechselwirkung zwei Aspekte derselben sogenannten elektro-schwachen Wechselwirkung sind. Die elektro-schwache Wechselwirkung wird durch vier masselose Bosonen vermittelt, die sich auf Grund von spontaner Verletzung der elektro-schwachen Symmetrie über den Higgs-Mechanismus bei alltäglichen Energieskalen zu den von uns beobachteten Austauschteilchen manifestieren. Der Higgs-Mechanismus, und das daraus hervorgehende Higgs-Boson, verleiht allen massiven Elementarteilchen ihre Masse. Die Fermionen werden in zwei weitere Kategorien unterteilt. Die Quanteneigenschaften von Quarks ermöglichen es ihnen an allen drei Wechselwirkungen teilzunehmen. Leptonen hingegen wechselwirken nur schwach und elektromagnetisch, wie z.B. das Elektron (e), oder ausschließlich schwach, wie das Elektron-Neutrino (ν_e). Insgesamt enthält das Standardmodell sechs Quarks und sechs Leptonen, die jeweils in drei Familien unterteilt werden, sowie die entsprechenden Antiteilchen. Die Quantenfeldtheorie der starken Wechselwirkung heißt Quantenchromodynamik (QCD) und ist in Analogie zur Quantenelektrodynamik (QED) entwickelt worden. Für die starke Ladung der starken Wechselwirkung, analog zur elektrischen Ladung der elektromagnetischen Wechselwirkung, wurde ein anschauliches Konzept eingeführt, das sie als Farbladung beschreibt, die die drei Werte rot, grün und blau annehmen kann. Jedes Quark trägt somit eine Farbladung und jedes Antiquark eine Antifarbladung. Die QCD weist im Vergleich zur QED mehrere Besonderheiten auf. Zum einen tragen Gluonen auch Farbladung und können somit mit sich selbst wechselwirken. Zum anderen variieren die Stärke der starken Kopplungskonstante und des Potentials zwischen zwei Quarks mit dem Impulsübertrag oder dem Abstand der Quarks. Daraus geht hervor, dass Quarks in der Natur zu farbneutralen Objekten (Baryonen oder Mesonen) gebunden sind und einzeln nicht beobachtet werden können. Bei extremen Energien oder extrem kleinen Abständen können sich Quarks und Gluonen jedoch quasi-frei bewegen. Diese Bedingungen sind in einem QGP erfüllt, sodass dessen Erforschung über weitere Eigenschaften und Details der grundlegenden Prozesse der starken Wechselwirkung Aufschluss geben kann.

Am CERN LHC (*Large Hadron Collider*) werden Blei-Ionen auf relativistische Energien

von bis zu 2,68 TeV pro Nukleon beschleunigt und an festen Punkten zur Kollision gebracht. Auf Grund der hohen Nukleondichte von Schwerionen, wie z.B. Blei, und der extrem hohen Schwerpunktsenergie der Kollision wird die Energie in Teilchen und Masse umgewandelt, wobei ein extrem heißes Medium mit verschwindender Netto-Baryon-Dichte entsteht. Dieser Anfangszustand ist geprägt von Fluktuationen der an der Kollision teilnehmenden Nukleonen und Partonen aus den Bleikernen. Durch Prozesse mit niedrigem Impulsübertrag verschmieren die Fluktuationen und es bildet sich nach weniger als $1\,\mathrm{fm}\,c^{-1}$ ein QGP aus. Die Partonen im QGP bewegen sich allerdings nicht komplett frei, sondern wechselwirken stark mit dem Medium. Daher führen ursprüngliche Fluktuationen und Asymmetrien in der Energiedichteverteilung zu Druckgradienten, die die Expansion und Abkühlung des QGPs einleiten und vorantreiben. Erreicht das QGP nach einigen $\mathrm{fm}\,c^{-1}$ die kritische Übergangstemperatur zum Hadrongas von ungefähr 155 MeV, hadronisieren die Partonen durch Fragmentation von Jets oder Koaleszenz, wobei der Übergang kontinuierlich ist. Nachdem sich die finalen Teilchenverhältnisse und Impulsverteilungen eingestellt haben, können sich die Teilchen im Endzustand frei weiterbewegen. Ihre kinetischen Eigenschaften werden über ihre Flugbahn von Detektoren bestimmt, die um den Kollisionspunkt herum konzipiert und aufgestellt sind, wie z.B. dem Detektor des ALICE Experiments. Anhand aufwändiger Analysen dieser Daten und Vergleichen zu Modellen lassen sich die physikalischen Eigenschaften des QGP und die Prozesse beim Übergang zum Hadrongas rekonstruieren.

Der ALICE Detektor besteht aus mehreren kleineren Detektorsystemen, deren Informationen für die Datenanalysen kombiniert werden. Die Detektorsysteme im zentralen Teil von ALICE sind zylindrisch um die Strahlachse herum in radialen Lagen angeordnet und befinden sich innerhalb des L3 Solenoids, der ein nominelles Magnetfeld von 0,5 T entlang der Strahlachse erzeugt. Zu diesen zentralen Detektoren gehören, von innen nach außen, das ITS (*Inner Tracking System*), die TPC (*Time Projection Chamber*), der TRD (*Transition Radiation Detector*) und der TOF (*Time-Of-Flight*) Detektor, die gemeinsam für die Rekonstruktion von Teilchenspuren und Identifikation der Teilchenspezies bei mittleren Rapiditäten genutzt werden. Zudem gibt es noch mehrere Kalorimeter, mit denen u.a. Zerfälle von neutralen Teilchen gemessen werden können. Auf einer Seite des Kollisionspunktes in Vorwärtsrichtung befindet sich das Myon Spektrometer zur Messung verschiedener Resonanzen, die in den $\mu^+\mu^-$-Kanal zerfallen. Es besteht aus mehreren Detektorlagen zur Spurrekonstruktion und einem passiven Absorber, der davor im Solenoid plaziert ist und Hadronen und Photonen absorbiert. Weiterhin gibt es in Vorwärtsrichtung noch einige kleinere Detektoren, die zur Selektion von Kollisionen und zur Bestimmung der Teilchenmultiplizität verwendet werden.

Die TPC ist eine zylindrische Spurendriftkammer mit einer Länge von 5 m, die Radien zwischen 84,8 cm und 246,6 cm aktiv abdeckt. Damit ist sie der wichtigste Detektor von ALICE zur Spurrekonstruktion und Teilchenidentifikation. Das aktive Gasvolumen der TPC von $88\,\mathrm{m}^3$ wird von zwei Zylindern eingeschlossen und von der zentralen Hochspannungselektrode in der Mitte in A und C Seite unterteilt. Um ein nominelles Driftfeld von $400\,\mathrm{V\,cm}^{-1}$ zu erzeugen, werden an der zentralen Elektrode $-100\,\mathrm{kV}$ angelegt. Ein sehr fein segmentierter Feldkäfig mit 165 Streifen pro Seite, deren Potentiale mit dem Driftfeld abfallen, sorgt für eine extrem hohe Homogenität des Driftfeldes im gesamten Volumen der TPC. An den Endkappen auf beiden Seiten sind die Auslesekammern montiert, deren dem Driftvolumen zugewandten Elektroden auf dem Potential des Driftfeldes liegen. Die Auslesekammern sind in azimuthaler Richtung in 18 Sektoren angeordnet und in jedem Sektor in eine innere (IROC) und äußere (OROC) Kammer unterteilt. Als Auslesekammern werden Vieldrahtproportionalkammern (*Multi-Wire Proportional Chambers*, MWPCs) verwendet, die aus mehreren Lagen von Drahtebenen und einer segmentierten Ausleseebene bestehen. Über der Ausleseebene

befinden sich die Anodendrähte, darüber wiederum versetzt die Kathodendrähte. An die Anodendrähte wird eine Hochspannung von 1 bis 2 kV angelegt, wodurch ein starkes radiales elektrisches Feld mit hohen Gradienten erzeugt wird. Über der Kathodenebene befindet sich eine weitere Drahtebene, das sogenannte *Gating Grid* (GG), auf dessen Drähte im geschlossenen Zustand ein zusätzliches alternierendes Störpotential gelegt wird, um es von beiden Richtungen undurchlässig für Elektronen und positive Ionen zu machen. Im offenen Zustand ist das Potential auf einem konstanten negativen Wert, sodass volle Transparenz für Elektronen aus dem Driftvolumen gewährleistet ist. Die Drähte aller Drahtebenen werden auf entsprechenden Halterungen an den Rändern der Auslesekammern fixiert und außen abgeschnitten. Eine zusätzliche Lage von Epoxidharz am äußeren Kammerrand sorgt für elektrische Isolation der Drahtpotentiale gegenüber dem Feld im offenen Driftvolumen. Das Volumen der TPC war in LHC *Run 1* (2009 bis 2013) mit Gasgemischen von Ne-CO_2 (90-10) bzw. Ne-CO_2-N_2 (90-10-5) gefüllt, mit denen die Auslesekammern mit Hochspannungen betrieben werden mussten, die nah an der Grenze zur Instabilität liegen. Um die Zuverlässigkeit der Auslesekammern in *Run 2* (2015 bis 2018) zu erhöhen wurde die Gasmischung zu Ar-CO_2 (88-12) geändert. Lediglich 2017 wurde noch einmal Ne-CO_2-N_2 (90-10-5) verwendet.

Die Funktionsweise einer Spurendriftkammer beruht auf dem Energieverlust durch Ionisation der hindurchfliegenden geladenen Teilchen im Gas und der Drift von Elektronen, d.h. deren Bewegung im elektrischen ($\boldsymbol{E}$) und magnetischen ($\boldsymbol{B}$) Feld. Wenn ein geladenes Teilchen das Driftvolumen der TPC durchquert, verliert es einen Teil seiner kinetischen Energie durch Kollisionen mit den Gasatomen, die zu deren Ionisation führen können. Somit hinterlässt das Teilchen entlang seiner Spur eine bestimmte Anzahl von Ionisationselektronen und positiven Ionen, die von der Geschwindigkeit des Teilchens, seiner Ladung und den Eigenschaften des verwendeten Gases abhängt. Der spezifische Energieverlust von geladenen Teilchen pro Wegstrecke wird durch die Bethe-Bloch Formel beschrieben. Die Ionisationselektronen driften mit konstanter Geschwindigkeit entlang des homogenen elektrischen Feldes im Driftvolumen auf geraden Bahnen zu den Auslesekammern. Durch die hohen elektrischen Felder in unmittelbarer Nähe der Anodendrähte werden die Ionisationselektronen dort durch Gasverstärkungsprozesse um Größenordnungen vervielfacht, um die Signalamplitude für die Ausleseelektronik zu erhöhen und sichtbar zu machen. Hierbei entstehen auch positive Ionen, die dem elektrischen Feld zur Ausleseebene sowie zu den Kathodendrähten und zu den GG-Drähten folgen. Auf der segmentierten Ausleseebene wird durch die langsame Bewegung der positiven Ionen ein Signal induziert, das proportional zur ursprünglichen Menge von Ionisationselektronen ist. Durch die Segmentierung der Ausleseebene lassen sich die Signale in der transversalen Ebene lokalisieren und zu sogenannten *Clustern* zusammenfügen. Bei bekannter Driftgeschwindigkeit der Elektronen im Gas kann die dritte Koordinate über die Messung der Driftzeit bestimmt werden. Die drei-dimensionale Spur des geladenen Teilchens kann somit mit Spurrekonstruktionsalgorithmen durch Kombination mehrerer *Cluster* ermittelt werden. Da sich der zentrale Teil von ALICE in einem Solenoid befindet, lässt sich auch die Krümmung der Teilchenspur und darüber ihr Impuls bestimmen. Über die registrierten Signale an der Ausleseebene lässt sich zudem die Menge von Ionisation bestimmen, die entlang der Teilchenspur deponiert wurde, was in Kombination mit der Impulsmessung die Identifikation des geladenen Teilchens ermöglicht.

Die präzise Rekonstruktion der Spurpunkte setzt das genaue Wissen über Inhomogenitäten des elektrischen und magnetischen Feldes voraus, da diese die Driftwege der Ionisationselektronen beeinflussen. Im Idealfall sind diese Inhomogenitäten kleiner als die Auflösung der Spurpunkte. Der Driftgeschwindigkeitsvektor und der Driftweg von Elektronen und positiven Ionen in elektrischen und magnetischen Feldern lässt sich über

die Langevin-Gleichung berechnen. Die Lösung der Langevin-Gleichung liefert dementsprechend auch die Abweichungen des nominellen Driftwegs auf Grund von Verzerrungen des elektrischen und magnetischen Feldes. Das nominelle $\boldsymbol{E}$-Feld der ALICE TPC verläuft entlang der Strahlachse und ist parallel zum $\boldsymbol{B}$-Feld. Globale und lokale Verzerrungen der Feldstärke allein führen zu einer Änderung der Driftgeschwindigkeit, was sich auf die Rekonstruktion der Koordinate in Driftrichtung auswirkt. Toleranzen in der Genauigkeit beim Ausrichten der einzelnen Elektroden, die das Driftfeld definieren, können zu diesem Effekt führen. Außerdem ändert sich die Driftgeschwindigkeit stetig mit äußeren Bedingungen, wie Luftdruck, Temperatur und der genauen Gaskomposition. Technische Limitierungen, z.B. die endliche Zahl von Feldkäfigstreifen, kann zusätzlich zu unvermeidbaren Verzerrungen des $\boldsymbol{E}$-Feldes in der Größenordnung von 10^{-4} führen. Die Inhomogenitäten des $\boldsymbol{B}$-Feldes betragen bis zu 1 %, was durch $\boldsymbol{E}\times\boldsymbol{B}$-Effekte den Driftvektor in radiale und azimuthale Richtung beeinflusst und die gemessene Position der Spurpunkte positionsabhängig um bis zu mehrere mm verzerrt. Gelangen positive Ionen in das Driftvolumen der TPC, z.B. Ionen von Primärionisation oder Ionen von Gasverstärkungsprozessen in den Auslesekammern, können signifikante Raumladungsdichten entstehen, da die Driftzeit der positiven Ionen um etwa einen Faktor 1000 größer ist als die von Elektronen. Die Raumladungsverzerrungen auf Grund einer beliebigen Raumladungsdichte können mit numerischen Methoden mit der Kalibrierungs- und Analysesoftware von ALICE berechnet werden. Die Korrektur von Spurpunktsverzerrungen geschieht entweder über Parametrisierungen, z.B. vom $\boldsymbol{B}$-Feld, oder durch die Messung der Verzerrungen in Daten. Hierbei werden die Detektoren ITS, TRD und TOF als Referenzen angenommen und deren Spursegmente werden ins Volumen der TPC interpoliert. Die mittlere Differenz der Referenzpunkte zu den TPC *Clustern* wird für ca. 400.000 kleine Raumelemente gemessen und zu einer Korrektur parametrisiert, die während der Rekonstruktion auf die TPC *Cluster* angewandt wird.

Nach dem Wechsel zu Ar-CO_2 zu Beginn von *Run 2* sind in der TPC in den ersten pp Daten bei hohen Interaktionsraten (>100 kHz) unerwartet große Spurpunktsverzerrungen von bis zu mehreren cm beobachtet worden, die nur an den Sektorgrenzen zwischen bestimmten IROCs an bestimmten Radien auftreten. Deren Ursache und Herkunft war zunächst ungeklärt, da sie aus *Run 1* mit Ne-CO_2 und niedrigeren Interaktionsraten nicht bekannt waren. Weiterhin traten ebensogroße Verzerrungen in OROC C06 auf, wo bekannterweise der Kontakt von zwei aufeinanderfolgenden GG-Drähten unterbrochen war und somit kein Potential auf den Drähten definiert werden konnte. Diese Arbeit beschäftigt sich mit der systematischen Untersuchung dieser Verzerrungen, um die Effekte zu bestimmen, die für sie verantwortlich sind, und um daraufhin Strategien zu entwickeln, mit denen man die Verzerrungen minimieren kann.

Erste Analysen der Verzerrungen in den IROCs als Funktion ihrer Position weisen eine lineare Abhängigkeit als Funktion der Driftlänge auf, was auf Raumladung im Driftvolumen hindeutet. Vergleiche mit Simulationen machen deutlich, dass die Raumladung die Form eines schmalen Zylinders hat, der an den Sektorgrenzen um einen kleinen radialen Bereich herum lokalisiert ist und sich von den Auslesekammern über die gesamte Driftstrecke zur zentralen Elektrode hin erstreckt. Die einzige Quelle für solche Mengen von positiven Ionen, die nur an den Auslesekammern erzeugt werden, ist Gasverstärkung an den Anodendrähten. Die Abhängigkeit der Verzerrungen mit Ar-CO_2 von der Interaktionsrate stellt sich als linear heraus, was in in erster Näherung mit der Annahme von Raumladung kompatibel ist. Allerdings fällt auch auf, dass in vielen Sektoren der lineare Zusammenhang bei den höchsten Interaktionsraten in Pb−Pb Kollisionen nicht mehr gegeben ist, da die Steigung mit der Interaktionsrate abnimmt und die Verzerrungen einen Sättigungseffekt zeigen. Weiterhin ändert sich die Größe der

Verzerrungen systematisch in allen Sektoren, wenn die Orientierung des $\boldsymbol{B}$-Feldes umgekehrt wird. Das relative Ausmaß der Änderung ist jedoch von Sektor zu Sektor unterschiedlich. Daten bei den höchsten Interaktionsraten aus *Run 1*, als die TPC mit Ne-CO_2 gefüllt war, wurden neu rekonstruiert, um zu prüfen, ob diese lokalen Verzerrungen bereits in *Run 1* vorhanden waren. Zudem wurde die TPC für ein Jahr in *Run 2* (2017) nochmals mit Ne-CO_2-N_2 betrieben, um die Messungen mit Daten aus *Run 1* zu bestätigen. Die Analyse dieser Daten zeigt, dass die lokalen Verzerrungen bereits in *Run 1* an genau denselben Positionen auftraten, allerdings waren sie um etwa eine Größenordnung kleiner als mit Ar in *Run 2*. Die Ergebnisse der *Run 1* und *Run 2* Daten mit Ne sind innerhalb systematischer Unsicherheiten konsistent. Der Unterschied in der Größe der Verzerrungen zwischen Ne und Ar ist signifikant höher, als man durch Inbetrachtnahme der grundlegenden Gaseigenschaften, wie Menge an gesamter Ionisation pro Wegstrecke (Faktor 2 kleiner in Neon) oder Ionenmobilität (Faktor 1.7 größer in Neon), erwartet. Vergleicht man die Abhängigkeit der Verzerrungen von der Interaktionsrate, erkennt man, dass die Verzerrungen mit Ne einen exponentiellen Anstieg aufweisen. Die beobachteten Effekte sind vereinbar mit der Annahme eines schmalen Zylinders von Raumladung im Driftvolumen. Bei relativ geringen Mengen von Ionisation, die in einer begrenzten Region an den Auslesekammern durch Gasverstärkung vervielfacht wird, wachsen die Verzerrungen exponentiell mit der Interaktionsrate, da die Raumladungsdichte sowohl auf Grund der steigenden Menge an Ionisation als auch auf Grund der damit wachsenden Verzerrungen zunimmt. Die wachsenden Verzerrungen lenken zusätzliche Ionisationselektronen in die Region, in der Gasverstärkung auftritt und Raumladung entsteht, was in Summe ein exponentielles Wachstum zur Folge hat. Ab einer gewissen Raumladungsdichte werden die $\boldsymbol{E} \times \boldsymbol{B}$-Effekte so groß, dass keine neue Ionisation von außerhalb mehr hinzukommt bzw. Ionisation aus der Verstärkungsregion verdrängt wird, sodass der exponentielle Verlauf in einen linearen Verlauf übergeht, der ab bestimmten Interaktionsraten saturiert. Weitere Studien demonstrieren eine Abhängigkeit der Verzerrungen von der Hochspannung an den Anodendrähten. Die Verzerrungen steigen exponentiell mit der Hochspannung, allerdings ist die Steigung kleiner als die des herkömmlichen Gasverstärkungsprozesses. Weiterhin können durch systematisches Ausschalten der Hochspannung an einzelnen Kammern diejenigen IROCs identifiziert werden, die für die Produktion der Raumladung verantwortlich sind. Die Verifizierung der Zuverlässigkeit des GG sowie parametrische Fits der Verzerrungen mit einem physikalischen Modell, basierend auf einer Linienladungsdichte, beweisen letztendlich, dass die Raumladung in dem Volumen zwischen zwei IROCs erzeugt wird, und nicht in der aktiven Ausleseregion. Dies deutet darauf hin, dass einzelne Enden von Anodendrähten nicht vollständig durch die Schicht von Epoxidharz am äußeren Kammerrand isoliert werden, da sie entweder ins Epoxidharz hineinragen oder teilweise sogar hinausragen. Eine abschließende Untersuchung der Auslesekammern mit einem Elektronenmikroskop während des *Long Shutdowns 2* (2019–2021) bestätigt diese Hypothese. Noch während *Run 2* wird eine Strategie entwickelt, um die Verzerrungen zu minimieren. Das Potential der *Cover*-Elektroden, die auf den Vorrichtungen zur Befestigung der Drähte angebracht sind, kann so verstellt werden, dass die Menge von Ionisation, die in das Volumen zwischen zwei Auslesekammern gelangt, signifikant verringert wird. Elektro-statische Simulationsstudien bestätigen und quantifizieren den erwarteten Effekt als Funktion des *Cover*-Elektroden-Potentials. Basierend auf den Studien werden bestimmte Potential-Einstellungen auch mit dem Detektor getestet. Es stellt sich heraus, dass eine Erhöhung des *Cover*-Elektroden-Potentials von $-180\,\mathrm{V}$ auf $+180\,\mathrm{V}$ am effektivsten funktioniert und die Verzerrungen auf durchschnittlich 30 % reduziert.

Die Verzerrungen in OROC C06 werden durch Raumladung aus dem Verstärkungsbereich der Auslesekammer erzeugt, die durch den fehlenden Kontakt der beiden GG-Drähte in

das Driftvolumen gelangen. Es wird untersucht, wie sich die Verzerrungen als Funktion der Hochspannung an den Anodendrähten sowie als Funktion der Potentiale an den noch funktionierenden GG-Drähten verändern. Da die Hochspannung sich direkt auf den Gasverstärkungsfaktor auswirkt, können die Verzerrungen ebenfalls um einen Faktor 2 verringert werden, indem der Gasverstärkungsfaktor um einen Faktor 2 gesenkt wird. Eine Erhöhung des alternierenden Störpotentials des GG von 90 V auf 120 V hat eine weitere Reduzierung der Verzerrungen um 34 % zur Folge. Insgesamt werden so die Verzerrungen in OROC C06 um einen Faktor von mehr als 3 verringert.

Die Untersuchungen und Studien, die in dieser Arbeit präsentiert werden, haben es ermöglicht, die lokalen Raumladungsverzerrungen in der ALICE TPC, die zu Beginn von *Run 2* mehrere cm betrugen, um ein Vielfaches zu reduzieren. Bei den höchsten Interaktionsraten der letzten Pb−Pb Strahlzeit von *Run 2* wurden maximale Raumladungsverzerrungen von unter 1 cm gemessen, die sich auf einen minimalen Anteil des Volumens der TPC beschränken. Somit konnte die intrinsische Auflösung der Spurrekonstruktion in der TPC wieder gewährleistet werden.

Contents

1 Introduction

The standard model is the modern theory of particle physics, which was developed in the 1960s and 1970s. It provides a fundamental understanding of elementary particles and their interactions. The fermions make up matter as we know it today, while the strong, weak and electromagnetic interactions are carried out by an exchange of gauge bosons associated to the gauge symmetry group $SU(3) \times SU(2) \times U(1)$. The electromagnetic and the weak interactions are different manifestations of the same force and they are unified within the standard model to the electroweak force at temperatures above the order of 100 GeV. In big bang cosmology, such temperatures were present up to the end of the electroweak era roughly a tenth of a nanosecond after the big bang. The symmetry groups $SU(2)$ and $U(1)$ yield the massless gauge bosons of the electroweak force with the corresponding quantum numbers, $\mathrm{W}^{1,2,3}$ with the third component of weak isospin T_3 and B with weak hypercharge Y. The physical force carrier of the electromagnetic force, the massless photon γ, and the ones of the weak force, the massive $\mathrm{W}^{\pm}$ and Z^0 bosons, emerge from the massless electroweak bosons by spontaneous breaking of the electroweak symmetry in the ground state via the Higgs mechanism. This effect led to the prediction of the scalar Higgs field and the discovery of the associated spin-zero Higgs boson at the Large Hadron Collider (LHC) in 2012 [2, 3]. The remaining unbroken symmetry of the electromagnetic interaction $U_{\mathrm{em}}(1)$ generates the corresponding quantum number of electric charge Q which is defined by the weak isospin and weak hypercharge via the relation $Q = T_3 + \frac{1}{2}Y$. The strong force is mediated by the massless gluons belonging to the group $SU(3)$. Particles which couple to the strong interaction carry the quantum number color which can assume the three states red, green, blue and the corresponding opposites for anti-particles. According to the $SU(3)$ symmetry, there are eight gluons carrying one color and one anti-color each, which means that gluons can interact with each other. The fundamental fermions are distinguished by their property of taking part in the strong interaction. The six leptons e, μ, τ, ν_{e}, ν_μ and ν_τ do not interact strongly. The charged electron-like leptons (e, μ, τ) interact both electromagnetically as well as weakly while the neutrino-like leptons (ν_{e}, ν_μ and ν_τ) have no electric charge and they only take part in weak interactions. The elementary hadrons, which are the particles interacting strongly, are called quarks and they appear in six flavors (u, d, c, s, t, b). They carry both color and electric charge and they also transform via the weak interaction. Due to intrinsic properties of the strong interaction discussed in the next paragraph, the hadrons observed in nature are composite objects of two or three (anti-)quarks. The so-called mesons are bound states of a quark and antiquark while the baryons are composed of three quarks [4].

The quantum theory which describes all phenomena of the strong interaction, similarly as Quantum Electrodynamics (QED) does for the electromagnetic force, is called Quantum Chromodynamics (QCD). However in contrast to QED, the coupling constant of QCD (α_{s}) is of the order of one and it depends on the momentum transfer (Q^2):

$$\alpha_{\mathrm{s}}(Q^2) \propto \frac{1}{\ln(Q^2/\Lambda^2)} \,, \tag{1.1}$$

where Λ is the scale constant. For hard collisions, which correspond to large Q^2 or small distances far below the nucleon radius, α_{s} takes small values and perturbative calculation methods are applicable. For soft collisions (small Q^2) or distances close to the nucleon radius, these dynamical calculations get non-perturbative and numerical methods like

lattice QCD have to be used. The complexity of the non-perturbative calculations can be appreciated by writing down the QCD Lagrangian [5]

$$\mathcal{L}_{QCD} = -\frac{1}{4}\sum_a F^a_{\mu\nu}F^{\mu\nu a} + i\sum_q \bar{\psi}^i_q \gamma^\mu (D_\mu)_{ij}\psi^j_q - \sum_q m_q \bar{\psi}^i_q \psi_{qi} \ , \tag{1.2}$$

where

$$F^a_{\mu\nu} = \partial_\mu A^a_\nu - \partial_\nu A^a_\mu + g_\mathrm{s}[A_\mu, A_\nu]^a \tag{1.3}$$

and

$$(D_\mu)_{ij} = \delta_{ij}\partial_\mu + i\frac{g_\mathrm{s}}{2}\sum_a \lambda^a_{i,j} A^a_\mu \ . \tag{1.4}$$

The first term of Eq. (1.2) represents the eight vector potentials A^a_μ of the the gluon fields with color index $a = 1, 2, ..., 8$ as well as the self-interaction of gluons (third term in Eq. (1.3)). The color charge g_s relates to α_s by $\alpha_\mathrm{s} = g_\mathrm{s}/4\pi$. The second term of Eq. (1.2) describes the interaction between quarks and gluons, where ψ^i_q are the quark fields of color i and flavor q and $\lambda_{i,j}$ (Eq. (1.4)) are the representations of the $SU(3)$ group. Finally, the third term of Eq. (1.2) adds the self-interaction of quarks. A phenomenological potential $V(r)$ between a quark and an antiquark shows a characteristic property of QCD, which is called confinement:

$$V(r) = -\frac{\alpha}{r} + \sigma r \ . \tag{1.5}$$

The constant α in the Coulomb term is proportional to α_s. In addition, there is a positive term which increases linearly with the separation distance r, i.e. the attractive force between the quark-antiquark pair increases with their distance so that they cannot be separated. In fragmentation models, a new quark-antiquark pair is produced when the separation energy is higher than two quark masses, rather than separating the two quarks. Consequently, free quarks cannot be directly observed in nature or experiments. They are confined in color-neutral objects, i.e. either in mesons, where the color and the corresponding anti-color of the quark-antiquark pair cancel, or in baryons, where the sum of all three different colors adds to color-neutral. On the other hand at very short distances between two quarks, they behave as free particles as α_s approaches very small values, which is called asymptotic freedom or deconfinement in QCD. This particular feature results in a phase transition from hadronic matter to a Quark-Gluon Plasma (QGP) at very high temperatures or baryon densities, suddenly increasing the number of degrees of freedom from 3 for a classical pion gas to 47.5 for a three-flavor QGP [5]. First measurements by experiments at the Relativistic Heavy-Ion Collider (RHIC) [6, 7, 8, 9] indicate that the properties of the QGP resemble those of an ideal fluid. Furthermore, lattice QCD calculations demonstrate that the energy density at temperatures far above those at the phase transition are about 20 % lower than the Boltzmann limit for an ideal non-interacting gas [10]. The remaining coupling of the QGP matter and its emerging properties are of strong interest to many research programs. The phase diagram of strongly-interacting matter is schematically shown in Fig. 1.1 as a function of the temperature and the baryochemical potential μ_B. The phase boundary is indicated by the data points obtained from different experiments and the solid line calculated by lattice QCD. At vanishing μ_B, a rapid cross-over takes place at the critical temperature (T_c) of about 155 MeV [10], corresponding to an energy density of around $1\,\mathrm{GeV\,fm^{-3}}$. At low temperatures and high baryochemical potential, models predict a first-order phase transition which should end in a second-order phase transition at the critical point when μ_B is decreased. In the context of the standard model, phase transitions in elementary quantum fields at characteristic energy densities involve the breaking of fundamental symmetries of nature. According to big bang cosmology, the universe experienced a series of phase transitions predicted by the standard model, evolving from some initial state through a rapid expansion and cooling. One direct consequence of such a symmetry breaking is the emergence of particle mass via the Higgs

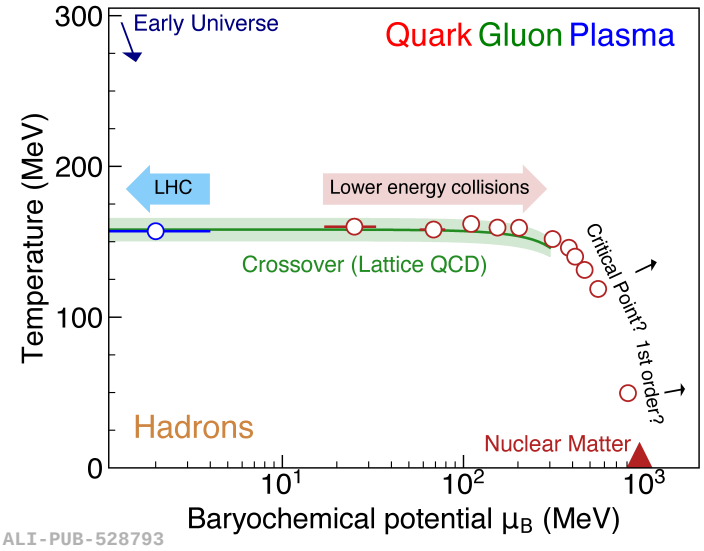

Figure 1.1: A schematic of the phase diagram of stongly-interacting matter as function of temperature and baryochemical potential (μ_B). Results from experiments (data points) and lattice QCD calculations (solid line) indicate the phase boundary between hadronic matter and the QGP [10].

mechanism. In the case of the QCD phase transition to a QGP, chiral symmetry is approximately restored, i.e. quark masses assume their small bare values instead of their large effective values in hadronic matter [11]. As it is believed that the early universe was in a state of deconfined strongly-interacting matter just microseconds after the big bang, theoretical and experimental studies of the phase transition and the QGP provide a deeper fundamental knowledge and understanding of nature and the evolution of the universe.

In the laboratory, a QGP is formed in collisions of heavy ions at relativistic energies. First experiments with ion beams were performed at the Lawrence Berkeley Laboratory (LBL) and the Joint Institute for Nuclear Research (JINR). By the end of the 1980s, research programs were set up at the Brookhaven National Laboratory (BNL) and at Conseil Européen pour la Recherche Nucléaire (CERN), dedicated to the observation of QGP signatures and the phase transition. At the Alternate Gradient Synchrotron (AGS) at BNL, fixed-target experiments studied heavy-ion collisions using a beam of silicon ions with energies of up to 15 A GeV or gold (Au) ions with energies of up to 11 A GeV. At the Super Proton Synchrotron (SPS) at CERN, lead (Pb) ions were accelerated to up to 158 A GeV. Much higher center-of-mass collision energies ($\sqrt{s_{\mathrm{NN}}}$) could be achieved at the first heavy-ion collider RHIC at BNL in 2000, which is able to collide Au ions at $\sqrt{s_{\mathrm{NN}}}$ of up to 200 GeV. The net-baryon density of the collision fireball at such energies is close to zero while extreme temperatures and energy densities are achieved, creating similar conditions as in the early universe. Another step in collision energy was achieved when the LHC [12] at CERN started to take data in 2009. Pb ions (or protons) at energies of 177 A GeV (450 GeV) are injected from the SPS into the two accelerator rings of the LHC where they are further accelerated to the final collision energy of up to 2.68 TeV (6.8 TeV). Four experiments are located at four collision points along the 27 km circumference of the LHC. ATLAS and CMS are designed for high-luminosity pp collisions and precision studies of the Higgs boson. LHCb's research focuses on studies of CP violation and hadrons containing b quarks. While these three experiments have also developed heavy-ion physics programs [10], ALICE is specifically built and designed to study the properties of the QGP and the phase transition at vanishing baryochemical potential with heavy-ion collisions.

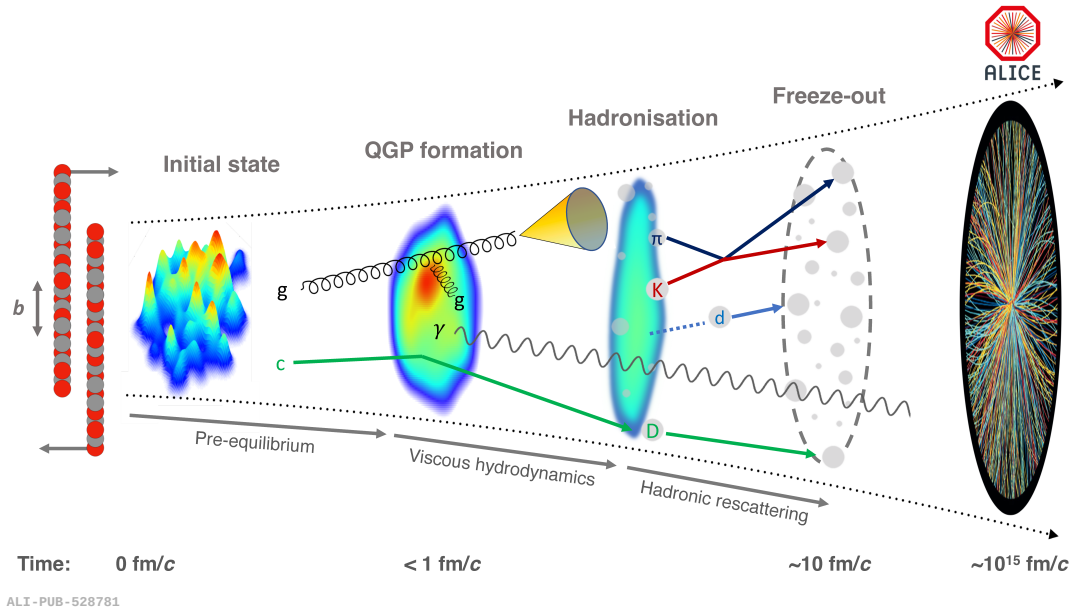

Figure 1.2: A schematic of the evolution of a heavy-ion collision at LHC energies [10].

1.1 Ultra-Relativistic Heavy-Ion Collisions

Extremely hot and dense matter with energy densities above the QGP threshold of $1\,\mathrm{GeV\,fm^{-3}}$ can be created in experiments by colliding heavy ions at (ultra-)relativistic energies. The energy of the colliding Lorentz-contracted nuclei is deposited in their overlap region where a variety of hard and soft QCD processes lead to particle production and to the formation of a rapidly expanding and cooling fireball. In contrast to the expansion of the early universe in the deconfined state of matter which had time scales of the order of µs, the expansion time of below $10^{-23}\,\mathrm{s}$ ($10\,\mathrm{fm}\,c^{-1}$) of the QGP created in heavy-ion collisions at LHC energies is small even on hadronic time scales [13]. On the other hand, the large projectile energies at LHC enable us to study the deconfined phase of matter and the phase transition to a hadron gas at zero net-baryon number, very similar as in the early universe, as the fragments of the colliding nuclei exit the collision zone and carry away the remaining baryon number before the QGP is formed.

Between the time of the collision and the moment when the final state particles reach the detectors surrounding the collision point, the created hot and dense medium evolves through several different stages which are defined by characteristic physical processes. The evolution of a heavy-ion collision at LHC energies is illustrated in Fig. 1.2. As the nuclei collide, soft inelastic interactions of the partons of participating nucleons determine the initial energy density profile [10]. Fluctuations in this initial state originate from fluctuations in the distributions of nucleons and partons in the nuclei. Following the initial collision, the weakly coupled pre-equilibrium phase is governed by soft interactions which lead to further production of soft partons, eventually resulting in the formation of a strongly coupled QGP after less than $1\,\mathrm{fm}\,c^{-1}$. High momentum gluons as well as high momentum and high mass quarks are created by hard QCD processes in parton-parton collisions. These particles are subject to radiative or elastic energy loss while they interact with other gluons or quarks in the medium. The formation of quarkonia is suppressed due to screening by the color charges in the medium but for QGPs with larger abundances of heavy quarks, the increased probability for recombination of heavy quarks which interact with the medium partially compensates for the suppression. Furthermore, parton fragmentation processes of high energy gluons and quarks can lead to jets of hadrons observed in the detectors. When the strongly-coupled QGP is formed, soft

interactions dominate the expansion and cooling stage. Non-uniformities in the initial energy density result in pressure gradients which smooth out initial fluctuations over time and drive the expansion of the QGP after $1\,\mathrm{fm}\,c^{-1}$. As the length scales of these gradients are larger than the mean free path of the partons in the medium, the evolution of the strongly-coupled QGP follows the principles of viscous hydrodynamics. The higher pressure in the center of the QGP is transformed into a radial flow and spatial anisotropies in the initial state, e.g. in semi-central collisions, are observed as momentum anisotropies as a consequence of anisotropic flow. Thermal photons and di-lepton pairs are produced at all stages of the evolution and they provide information about the temperature of the QGP because they do not take part in the QCD processes of the medium. Since the QGP temperature is also higher than the mass of strange quarks, strangeness is easily produced in the medium, mostly by gluon interactions. When regions of the QGP cool down to T_c, the partons in these regions hadronize via jet fragmentation or coalescence. As the energy density in the outer part of the medium is different from the inner parts and as the transition is expected to be a smooth cross-over, hadronization can start at different times in different regions. The emerging hadrons may still interact inelastically and change the particle composition, if the energy density is sufficient, until the temperature drops to the chemical freeze-out temperature when all particle abundances are fixed. Elastic interactions take place until the kinetic freeze-out temperature is reached at roughly $10\,\mathrm{fm}\,c^{-1}$, fixing also the particle momenta. The final state particles, part of which may further decay weakly, are then free to propagate to the detectors where they are measured by their hit points, trajectories and kinetic properties. The research of heavy-ion physics, specifically with ALICE at the LHC, addresses a broad range of questions covering thermodynamic and hydrodynamic properties of the QGP, effects of the QGP on parton propagation, hadron formation and the strong force, novel QCD effects, and many more [10].

1.2 A Large Ion Collider Experiment (ALICE)

ALICE is the dedicated heavy-ion experiment at the CERN LHC. It is designed as a general-purpose detector and provides excellent tracking and particle identification (PID) over a wide momentum range ($\approx$100 MeV c^{-1} up to 100 GeV c^{-1}) as well as event characterization. The detector design handles charged-particle densities ($\mathrm{d}N_{ch}/\mathrm{d}\eta$) of up to 8000 at mid-rapidity, which makes it well-suited for the environment in Pb$-$Pb collisions delivered by the LHC at center-of-mass collision energies ($\sqrt{s_\mathrm{NN}}$) of up to 5.36 TeV. The studies performed by ALICE address all stages of the collision as a broad range of observables is accessible on an event-by-event basis, which also allows to study correlations and non-statistical fluctuations. The initial conditions, e.g. collision geometry, initial energy density or impact parameter, are measured by global event features like multiplicity or transverse and zero-degree energy distributions. Properties of the plasma phase like parton kinematics and energy loss are probed via heavy-flavor production or jet fragmentation, while elliptic flow is sensitive to the equation of state (EoS). Quarkonia production probes deconfinement and parton recombination. Critical phenomena at and around the phase transition are reflected in multiplicity fluctuations. Interferometry provides access to the space-time evolution of the collision and the freeze-out radius and particle ratios and transverse momentum spectra are sensitive to the evolution of the hadronic phase [14, 15]. In addition to the Pb$-$Pb data, pp and p$-$Pb collisions as well as collisions of lighter ions (e.g. Xe$-$Xe) provide benchmarks for the interpretation of the heavy-ion results and, by themselves, allow to study further interesting properties of QCD. For more details, the extensive physics program of ALICE is described in the ALICE Physics Performance Reports [11, 16] while [10] provides a review of all major physics results of ALICE in LHC Run 1 and Run 2.

1.3 Outline

The following chapters lead towards the main topic of this thesis, which is the investigation of space-charge effects in the ALICE Time Projection Chamber (TPC) observed in LHC Run 1 and Run 2. A general overview of the ALICE detector system is given in Chapter 2. Some of the fundamental principles applied in the detection of particles with gaseous drift detectors, such as the TPC, are introduced in Chapter 3. The TPC is one of the central ALICE detector sub-systems. It uniquely combines the ability to precisely follow particle trajectories, contributing to the global momentum measurement, with the identification of the particle species, and it is a corner stone for a major fraction of physics analyses in the mid-rapidity region. Chapter 4 provides an overview of the ALICE TPC layout, it touches the basics of space-point and particle trajectory measurement techniques and it covers potential sources of distortions of these measurements, including the corresponding correction procedures. In first high-luminosity data at the beginning of LHC Run 2 in 2015, significant distortions of the space-point measurement w.r.t to the design specifications of the TPC for Run 1 and Run 2 were observed in specific local regions of the TPC phase space and they were not understood at first. Extensive studies were performed and they are summarized in Chapter 5. The investigations focus on characteristic dependencies of the observed distortions on collision and detector parameters, leading to the development of a physical model which helped to fully understand the effect and its origin. A mitigation strategy was identified and optimized with detector simulations as well as with real data. A summary of the research presented in this thesis is given in Chapter 6 followed by an outlook relating the topic of space charge in the TPC to the upgrade of the detector for LHC Run 3 and Run 4.

2 The ALICE Detector

The ALICE apparatus can be subdivided into a central barrel part around mid-rapidity, a forward muon-spectrometer and several smaller forward and trigger detector systems. A sketch of the detector is shown in Fig. 2.1 while the coordinate system employed for the experiment is explained in Appendix A. The following sections give an overview of the detector subsystems as they were employed during LHC Run 1 and 2.

For LHC Run 3, major upgrades of several ALICE sub-detectors, the trigger and readout system as well as the calibration and analysis software [17, 18, 19, 20, 21, 22] will provide significantly improved vertexing and tracking performance at low transverse momentum. The upgrades are motivated by the substantial increase in luminosity of the LHC. Continuous data readout at interaction rates of 50 kHz in Pb−Pb collisions will allow to collect much larger statistics, while the particle identification capabilities of the previous detector setup are preserved. The heavy-ion physics program of ALICE in Run 3 will focus on rare probes including heavy-flavor and quarkonia production, low-mass dileptons, jet measurements and the search for possible bound states and production of light (hyper-)nuclei [23].

2.1 Central Barrel Detectors

The central barrel consists of several tracking detectors, detectors for PID and calorimeters. While most of the tracking and PID detectors cover almost two units in pseudorapidity (η) and have full azimuthal acceptance, the calorimeters cover only part of the pseudorapidity range and azimuth. The L3 solenoid magnet surrounds the central barrel and provides a nominal magnetic field of 0.5 T along the beam axis. Dedicated data taking periods with low magnetic field (0.2 T) allow the measurement of charged particles with transverse momentum (p_{T}) well below 100 MeV c^{-1} and the separation of muons from pions in this low-p_{T} region [24, 25]. Good p_{T} resolution over the full dynamical momentum range is achieved by very low material thickness (13 % of the radiation length (X_0) up to the outer radius (r) of the TPC) to minimize multiple scattering at low-p_{T} and a large tracking lever arm of 3.68 m [15].

Inner Tracking System (ITS)

The Inner Tracking System (ITS) [26] is the inner-most detector of the central barrel and surrounds the beam pipe. The six cylindrical layers of silicon detectors are located at radii between 3.9 cm and 43 cm. The first two layers consist of Silicon Pixel Detectors (SPD), the two middle layers of Silicon Drift Detectors (SDD) and the two outer layers of double-sided Silicon Strip Detectors (SSD). They provide the ability to reconstruct space points with a precision in $r\varphi$ of 12 µm, 35 µm and 20 µm, respectively, resulting in a primary vertex resolution of better than 60 µm. Due to the very low total material budget of 7.26 % X_0, a relative momentum resolution of better than 2 % for pions with p_{T} between 100 MeV c^{-1} and 3 GeV c^{-1} is achieved. In addition, the SDD and SSD are equipped with analogue readout and can be used for particle identification via specific energy loss per unit path length ($\mathrm{d}E/\mathrm{d}x$) measurement down to the lowest momenta. Further tasks of the ITS are the reconstruction of secondary vertices from weakly-decaying particles and improving the momentum and angle resolution of tracks reconstructed by the TPC.

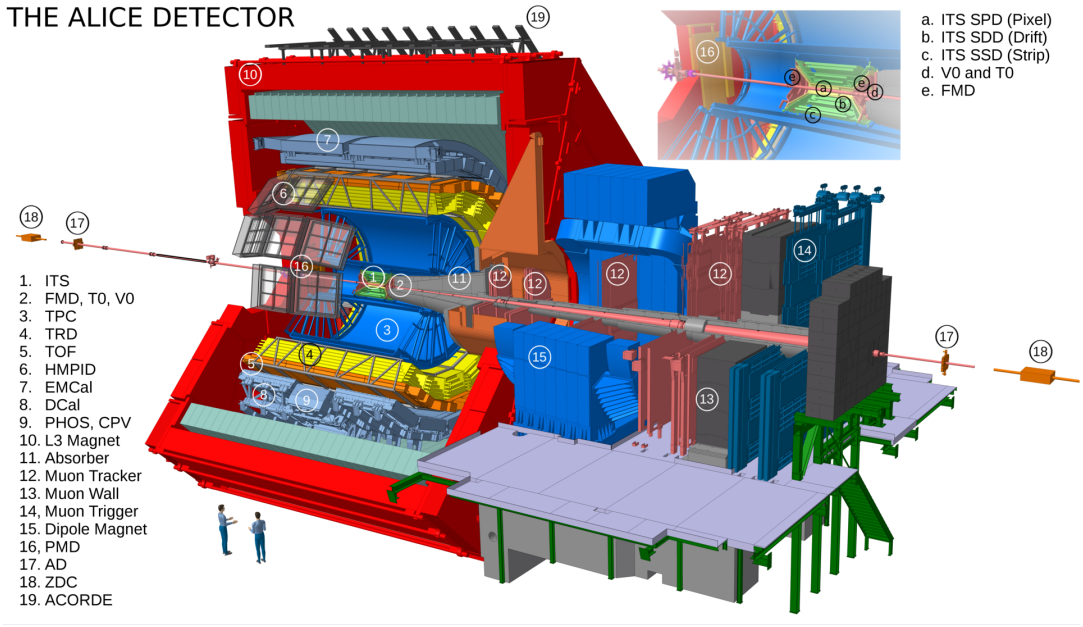

Figure 2.1: A schematic overview of the ALICE detector.

Time Projection Chamber (TPC)

The Time Projection Chamber (TPC) [27] is used for tracking, momentum measurement of charged particles in the magnetic field with good two-track separation, particle identification via the measurement of the specific energy loss per unit path length in the detector gas and vertex determination. It is a cylindrical detector with a length of 5 m, separated into two equal parts by the central high-voltage electrode (CE). At both ends of the cylinder, Multi-Wire Proportional Chambers (MWPCs) with segmented pad readout collect the signals from charged particles traversing the drift volume. The active area covers radii between 84.8 cm and 246.6 cm. The position resolution of reconstructed space points is around 800–1100 µm in pad direction ($r\varphi$) and 1100–1250 µm in drift direction (z), resulting in an intrinsic track resolution of 200 µm. With up to 159 space points and $\mathrm{d}E/\mathrm{d}x$ samples per track, a $\mathrm{d}E/\mathrm{d}x$ resolution of 5–7 % is achieved. The detector layout of the TPC is discussed in detail in Chapter 4.

Transition Radiation Detector (TRD)

The Transition Radiation Detector (TRD) [28] is arranged in 18 super modules along the azimuthal angle (φ), each consisting of five stacks in z with an active length of 7 m and six layers in radial direction at positions between 290 cm and 368 cm. Each detector element is based on a MWPC of 7 mm thickness with a 30 mm drift section. The segmented pad readout has been optimized to achieve a space-point resolution of about 400 µm in $r\varphi$ and 2 mm in z, resulting in a stand-alone relative momentum resolution of around 3 % at a particle momentum of 1 GeV c^{-1}. Therefore, the TRD complements the global tracking and improves the overall momentum resolution, which is better than 7 % up to momenta of about 100 GeV c^{-1}. The measurement of the specific energy loss per unit path length in the Xe-CO_2 (85-15) gas mixture provides PID information. In addition, each detector element is equipped with a carbon fibre laminated Rohacell / polypropylene fibre sandwich radiator of 48 mm thickness. Electrons with momenta above 0.5 GeV c^{-1} (Lorentz factor (γ) $\approx$ 1000) produce Transition Radiation (TR) of on average 1.45 X-ray photons in the radiator material. Detecting on average 1.25 of those TR photons in the counting gas, the TRD extends the electron-pion separation capabilities provided by the TPC up to momenta of 1–6 GeV c^{-1}, with a pion suppression better than 100 at

an electron efficiency of 90 %. Furthermore, the TRD serves as a fast Level-1 trigger for high-momentum particles and jets, electrons and nuclei [29].

Time-Of-Flight detector (TOF)

The Time-Of-Flight detector (TOF) [30, 31] modules are set up into 18 sectors in φ and five segments in z with an inner and outer radius of 370 cm and 399 cm, respectively. The active area has a length of 741 cm in z, covering a pseudorapidity of $|\eta| < 0.9$. Each module consists of a group of 10-gap double-stack Multi-gap Resistive-Plate Chamber (MRPC) strips with segmented pad readout and an intrinsic time resolution of better than 40 ps. The time-of-flight measurement with the TOF provides particle identification in the intermediate momentum range (below 2.5 GeV c^{-1} for pions and kaons and up to 4 GeV c^{-1} for protons) with a π/K and K/p separation better than 3σ.

High-Momentum Particle Identification Detector (HMPID)

The High-Momentum Particle Identification Detector (HMPID) [32] is placed at a radius of 5 m and covers a region of $|\eta| < 0.6$ and $1.2° < \varphi < 58.8°$. It is based on proximity-focusing Ring Imaging Cherenkov (RICH) detectors consisting of a 15 mm thick low-chromaticity C_6F_{14} liquid radiator and a MWPC with a thin layer of CsI deposited on its pad cathode as a photon counter. The HMPID is optimized for the detection of high-momentum charged particles, extending the usable momentum ranges for π/K and K/p separation provided by the $\mathrm{d}E/\mathrm{d}x$ and time-of-flight measurement up to 3 GeV c^{-1} and 5 GeV c^{-1}, respectively.

Photon Spectrometer (PHOS)

The Photon Spectrometer (PHOS) [33] is designed as a single-arm high-resolution high-granularity electromagnetic spectrometer for the measurement of low-p_{T} direct photons and high-p_{T} π^0 and γ-jet correlations, studying the thermal and dynamical properties of the initial phase of the collision and jet quenching. It has an acceptance of $|\eta| < 0.12$ and $250° < \varphi < 320°$ [34] at a radial distance of 460 cm from the interaction point. The highly-segmented electromagnetic calorimeter (PHOS) provides high energy and spatial resolution and a time resolution of a few ns by using dense scintillator material ($PbWO_4$) and a fast preamplifier, identifying photons by shower topology analysis and time-of-flight measurement. On top of the PHOS, a charged-particle veto (CPV) detector, based on MWPCs with a charged-particle detection efficiency of better than 99 %, is used to discriminate photons from charged hadrons.

Electromagnetic Calorimeter (EMCal)

The Electromagnetic Calorimeter (EMCal) [35] is a two-arm Pb-scintillator sampling calorimeter, with the second arm installed during the first long shutdown of the LHC and referred to as Di-Jet Calorimeter (DCal) [36]. Both are located at radii of 428 cm and positioned roughly opposite to each other in azimuth. The EMCal has an acceptance of $|\eta| < 0.7$ and $80° < \varphi < 187°$, while the DCal covers a pseudorapidity of $0.22 < |\eta| < 0.7$ at $260° < \varphi < 320°$ and $|\eta| < 0.7$ at $320° < \varphi < 327°$. The EMCal and DCal allow to measure electrons from heavy-flavor decays and spectra of direct photons and neutral mesons as well as to study jet quenching and hadron-jet and di-jet correlations, using also the PHOS to close the acceptance window at central rapidity.

ALICE Cosmic Ray Detector (ACORDE)

The ALICE Cosmic Ray Detector (ACORDE) [37] sits on top of the L3 magnet at $-60° < \varphi < 60°$ and covers $|\eta| < 1.3$. It consists of plastic scintillator counters and is used to trigger on cosmic muons for the commissioning, calibration and alignment of the

tracking detectors. It also provides the possibility to study atmospheric muon spectra in a wide momentum range with very high precision.

2.2 Muon Spectrometer

The ALICE Muon Spectrometer [38, 39] is specifically designed to measure the complete spectrum of heavy-quark vector-meson resonances in the $\mu^+\mu^-$ channel and the unlike-sign dimuon continuum up to masses around $10\,\mathrm{GeV}\,c^{-2}$ in the pseudorapidity range of $-4.0 < |\eta| < -2.5$. It consists of ten planes of cathode pad chambers arranged in five stations, two of which are placed in front, one inside and two behind a large dipole magnet. A spatial resolution of 100 µm of the tracking chambers and a nominal magnetic field integral of 3 T m allow measurements of the invariant mass with a resolution of $100\,\mathrm{MeV}\,c^{-2}$ in the Υ mass region. A large passive absorber made out of carbon and concrete is placed inside the solenoid magnet in front of the first tracking station to absorb hadrons and photons from the interaction vertex. Further protection for the tracking chambers is provided by a dense absorber tube built along the full spectrometer length around the beam pipe. Behind the last tracking chamber, a muon filter wall made out of iron protects the four layers of trigger chambers arranged in two stations. They are based on position-sensitive MRPCs, operated in streamer mode, with a position resolution of better than 1 cm.

2.3 Forward Detectors

Zero Degree Calorimeter (ZDC)

The Zero Degree Calorimeter (ZDC) [40] is a set of position-sensitive calorimeters to measure the energy of spectator nucleons. It provides information about the geometry of heavy-ion collisions, which can also be used as a Level-1 trigger to select central, semi-central and minimum-bias events, and can also be used to estimate the reaction plane. Two quartz-fibres sampling hadronic calorimeters are located at 112 m on each side of the interaction point. The compact Zero Degree Neutron Calorimeter (ZN) is placed between the two beam pipes to detect spectator neutrons, while the Zero Degree Proton Calorimeter (ZP) is placed externally to the outgoing beam pipe as the spectator protons are separated from the neutrons by the LHC magnets. At 7 m from the interaction point opposite to the muon arm, the Zero Degree Electromagnetic Calorimeter (ZEM) measures the energy of particles emitted in the forward region ($4.8 < |\eta| < 5.7$), complementing the hadronic ZDCs. This measurement provides the possibility to discriminate between very peripheral and central events when the charge-to-mass ratio of the spectator fragments from very peripheral events is similar to those of Pb ions, making them stay in the beam pipe and not being detected by the ZP and ZN.

Photon Multiplicity Detector (PMD)

The Photon Multiplicity Detector (PMD) [41, 42] is a pre-shower detector at a distance of 3.64 m from the interaction point, consisting of two planes of highly-granular gas proportional counters and a three radiation length thick converter in-between. The first detection plane in front of the converter is used as a charged-particle veto (CPV), the second one provides photon identification from the pre-shower data. The PMD measures the multiplicity and spatial distributions of photons in the forward region of $2.3 < |\eta| < 3.7$.

Forward Multiplicity Detector (FMD)

The Forward Multiplicity Detector (FMD) [43] is used for the measurement of the charged-particle multiplicity and event-by-event multiplicity fluctuations, the estimation of the reaction plane and the analysis of flow. It consists of three planes of segmented silicon sensor rings. Two of them are located close to the ITS on either side of the primary vertex and a third one is placed at $z = 3.2\,\mathrm{m}$ on the opposite side of the muon arm, covering a pseudorapidity range of $-3.4 < |\eta| < -1.7$ and $1.7 < |\eta| < 5.0$.

V0 detector (V0)

The V0 detector (V0) [43] consists of two detectors, V0A and V0C, located on either side of the interaction point at 3.4 m and in front of the muon absorber at 0.9 m, respectively. Both consist of four rings of scintillator counters and cover a pseudorapidity range of $2.8 < |\eta| < 5.1$ and $-3.7 < |\eta| < -1.7$, respectively. The V0 provides minimum-bias, multiplicity, semi-central and central triggers for the central barrel detectors and is used for the centrality determination in heavy-ion collisions. It can also reject background events from interactions of protons with the beam gas and false triggers from the muon trigger chambers.

T0 detector (T0)

The T0 detector (T0) [43] consists of Cherenkov counters placed on each side of the collision vertex. The T0A covers $4.61 < |\eta| < 4.92$ at $z = 3.75\,\mathrm{m}$ while the T0C covers $-3.28 < |\eta| < -2.97$ and is located at $z = -72.7\,\mathrm{m}$. It is designed to provide a start time for the TOF, measuring the collision time with a precision of 37 ps, to issue a L0 trigger when the collision is within the predefined z range, measuring the vertex position with an accuracy of 1.5 cm, and to generate minimum-bias and multiplicity triggers.

AD0 detector (AD0)

The AD0 detector (AD0) [44], included into the data taking in Run 2, improves the detection sensitivity for diffractive events and is able of expanding the pseudorapidity coverage of the minimum-bias and centrality trigger. It consists of two scintillator counters, positioned on either side of the interaction point at $z = 18\,\mathrm{m}$ ($4.8 < |\eta| < 6.3$) and at $z = -20\,\mathrm{m}$ ($-7.0 < |\eta| < -4.9$).

3 Fundamentals of Gaseous Drift Detectors

Drift chambers are used for the precise measurement of space points and trajectories of traversing particles in particle physics experiments since the early 1970s. While the geometry and properties of drift chambers are optimized for individual applications, they all rely on the same principles. A common type of drift detector consists of a drift volume and a readout part. The drift volume is usually filled with a mixture of a noble gas, e.g. Ar, and a quencher, for instance CO_2. The traversing particles lose a small fraction of their energy, typically of the order of a few $\mathrm{keV\,cm^{-1}}$, in collisions with the gas atoms which can be ionized in these collisions. The created ionization electrons drift along the electric field applied across the drift volume towards the readout part of the drift chamber. The readout is based on sensitive electrodes, e.g. MWPCs with a segmented readout, where the ionization electrons are multiplied in high electric fields by gas amplification. The measurement of the induced signal provides the 2-dimensional information of the position of the space point in the transverse plane. The third coordinate can be derived by measuring the arrival time of the ionization electrons in combination with the time of the initial event. All involved processes require detailed knowledge about the drift, diffusion and amplification of electrons in a gas mixture due to electric and possibly magnetic fields. Today, large TPCs with radii of up to 2.5 m are used in heavy-ion experiments. Their low material budget and their capability to measure space-points with highest precision makes them excellent particle-tracking devices. In addition, they provide particle identification by the measurement of the deposited charge per unit of length of the particle track if simultaneously measuring the momentum via the curvature of the track in a magnetic field, e.g. inside a solenoid. The physics fundamentals of all those processes are introduced in this chapter, specifically w.r.t. the working principle of TPCs and those relevant for the research presented in this thesis. A more complete and more detailed collection can be found in [45].

3.1 Energy Loss of Charged Particles in Matter

When fast charged particles travel through a drift chamber, they lose a small fraction of their kinetic energy in collisions with the gas atoms in the drift volume. A certain fraction of the energy loss is spent in ionization of the gas atoms. The number of ionizing collisions over a given length is random, following a Poisson distribution, and it is characterized by the mean free flight path λ, the ionization cross section σ_I per electron and the electron density N in the gas ($\lambda = \frac{1}{N\sigma_\mathrm{I}}$). Primary ionization is defined as the ionization electrons directly released in collisions of the fast particles and the gas atoms. Primary electrons themselves lose their total kinetic energy in collisions with further gas atoms. Ionization electrons from such collisions are called secondary electrons or secondary ionization. The distance from the trajectory of the fast particle covered by primary electrons until they are fully stopped depends on the gas properties and the energy of the primary electron and it is of the order of tens to hundreds of µm for common gas mixtures. Another process for secondary ionization is called Penning effect, where a gas atom (in a mixture, it is usually the noble gas) is excited in a collision with the traversing particle or a primary electron and ionizes another gas atom (from the quencher) in a subsequent collision. The average total number of ionization electrons $\langle N_\mathrm{I} \rangle$ from all processes along the trajectory of the fast

charged particle relates to its total mean specific energy loss per unit path length ($\langle \frac{\mathrm{d}E}{\mathrm{d}x} \rangle$) by

$$W\langle N_\mathrm{I} \rangle = L \left\langle \frac{\mathrm{d}E}{\mathrm{d}x} \right\rangle \ , \tag{3.1}$$

where L is the length of the trajectory and W is the average amount of energy spent to create one ionization electron.

The measurement of the specific energy loss per unit path length ($\mathrm{d}E/\mathrm{d}x$) provides the means for particle identification with drift chambers. The first calculation of $\mathrm{d}E/\mathrm{d}x$ was performed by Bethe in 1930, using a quantum theory of collisions between fast charged particles and single atoms and integrating the energy lost to all individual atoms in the gas, which lead to the Bethe-Bloch formula. Over time, the initial version of the formula was extended with correction terms to account for additional quantum effects and it was modified to be generally applicable for drift chambers, independent of different kinematic limits of particles with largely different masses. The modified Bethe-Bloch formula [45] can be written as

$$\frac{\mathrm{d}E}{\mathrm{d}x} = \frac{4\pi N e^4}{mc^2} \frac{1}{\beta^2} z^2 \left[\ln \frac{\sqrt{2mc^2 E_\mathrm{max}}\beta\gamma}{I} - \frac{\beta^2}{2} - \frac{\delta(\beta)}{2} \right] \ . \tag{3.2}$$

The number density of electrons in the gas mixture is denoted by N, e is the elementary charge and mc^2 is the rest energy of the electron. The velocity of the particle relative to the speed of light c is expressed by β, $\gamma = 1/(1-\beta^2)$ and z is the charge of the particle. $\delta(\beta)$ is a correction term which depends on the medium and which accounts for the coherent effect of the surrounding polarizable atoms shielding the field of the traveling particle. The mean excitation energy I of the gas atoms is obtained from fits to the measurement of the ionization energy loss. The factor E_max is an effective cut-off energy for statistical processes with an extremely high energy loss which are insignificant or have a vanishing probability to occur in drift chambers. Eq. (3.2) is valid in this form only in the range of $\beta\gamma$ where E_max is smaller than the kinematic limit and where $\gamma^2 \gg E_\mathrm{max}/mc^2$. Therefore, it can be applied for massive particles as well as for electrons and it only depends on the velocity β of the particle. There are four characteristic regions of Eq. (3.2) as a function of $\beta\gamma$. At small $\beta\gamma$, $\mathrm{d}E/\mathrm{d}x$ decreases with $1/\beta^2$ as $\beta\gamma$ is increased until it reaches a minimum at about $\beta\gamma = 4$. Particles at the minimum are called minimum ionizing particles (MIPs). Beyond the MIP region, the energy loss increases again in the region of the relativistic rise dominated by the logarithmic term of Eq. (3.2) until it saturates at the Fermi-plateau defined by $\delta(\beta)$.

3.2 Drift of Electrons and Ions

The performance of drift chambers is determined by the drift and diffusion properties of ionization electrons and ions in the drift gas. These properties are characteristic for every gas or gas mixture and they can change significantly with the exact gas composition, temperature and pressure. In addition, they strongly depend on the electric and magnetic fields applied in the drift or amplification region.

In microscopic theory, the motion of electrons with kinetic energy much bigger than their thermal energy is described by random collisions with gas atoms along their drift path, defining τ as the average time between two collisions. Due to their small mass, the electrons fully lose the momentum they had before the collision as they scatter isotropically and pick up a random velocity and direction. Between two collisions, the electrons are accelerated by the electric field and they gain extra velocity in the direction of the electric field, which is lost on average in the next collision. Therefore on average, a balance between kinetic energy lost in collisions and gained from the field is established.

On the macroscopic scale, the average velocity picked up by the electrons between collisions is the drift velocity u which is defined by the acceleration along the field E and τ as

$$u = \frac{eE}{m}\tau = \mu E \,, \tag{3.3}$$

where e and m are the electric charge and the mass of the electron and the scalar mobility μ is defined as the ratio of the drift velocity over the electric field in the absence of a magnetic field ($\mu = \frac{e}{m}\tau$). Due to the random scattering processes, the direction of the instantaneous drift velocity vector deviates from the direction of the field. Assuming isotropic diffusion in all three spatial dimensions, a point-like cloud of electrons will assume a Gaussian distribution after some drift time t. The width of the distribution in any direction x is defined by the diffusion constant D as $\sigma_x^2 = 2Dt$. The drift properties of ions are significantly different from those of electrons due to their much larger mass and their chemical reactions [45, 46]. In similar fields, ions lose a bigger fraction of their acquired energy in collisions with gas atoms and their motion is much less random. As a consequence, the mobility and the diffusion of ions is orders of magnitude smaller than those of electrons.

The drift of electrons and ions at large drift times t can be well approximated macroscopically using the equation of motion in an electric field ($\boldsymbol{E}$) and a magnetic field ($\boldsymbol{B}$) by Langevin [45]:

$$m\frac{\mathrm{d}\boldsymbol{u}}{\mathrm{d}t} = e\boldsymbol{E} + e\left(\boldsymbol{u}\times\boldsymbol{B}\right) - K\boldsymbol{u} \,. \tag{3.4}$$

The drift velocity vector is denoted as $\boldsymbol{u}$ and K is a frictional force originating in the interactions with the gas. Here, $\tau = m/K$ is defined as a characteristic time compared to the microscopic picture where τ is the time between two collisions. The solution of Eq. (3.4) for $t \gg \tau$ can be written as

$$\boldsymbol{u} = \frac{e}{m}\tau|\boldsymbol{E}|\frac{1}{1+\omega^2\tau^2}\left[\hat{\boldsymbol{E}} + \omega\tau\left(\hat{\boldsymbol{E}}\times\hat{\boldsymbol{B}}\right) + \omega^2\tau^2\left(\hat{\boldsymbol{E}}\cdot\hat{\boldsymbol{B}}\right)\hat{\boldsymbol{B}}\right] \,, \tag{3.5}$$

where $\hat{\boldsymbol{E}}$ and $\hat{\boldsymbol{B}}$ are the unit vectors of the directions of the electric and magnetic fields and $\omega = \frac{e}{m}|\boldsymbol{B}|$ is the cyclotron frequency of the electron. In the presence of a magnetic field, the components of the drift vector along $\hat{\boldsymbol{B}}$ and perpendicular to $\hat{\boldsymbol{E}}$ and $\hat{\boldsymbol{B}}$ are determined by the Lorentz angle ($\omega\tau$). Special cases of particular interest for drift chambers include those where the magnetic field $\boldsymbol{B} = B_z$ is nearly parallel to the electric field $\boldsymbol{E} = E_z$, having only small perturbations in the other two dimensions x and y, and those where the magnetic field is perpendicular to the electric field ($\boldsymbol{B} = B_x$, $\boldsymbol{E} = E_z$). Furthermore, disturbances of the nominal electric field, e.g. caused by positive ions in the drift volume, lead to distortions of the drift vector and the arrival points of the electrons. For small disturbances E_{dist} perpendicular to or in line with the nominal field E_{drift}, the distortion of the drift path dx can be calculated by

$$dx = L\frac{E_{\mathrm{dist}}}{E_{\mathrm{drift}}} \,, \tag{3.6}$$

where L is the drift length. A more general and practical way to calculate the distortions of electron drift paths due to additional $\boldsymbol{E}$ and $\boldsymbol{B}$-field components is derived in [47], assuming small perturbations of the order of less than 10 % and expanding Eq. (3.5) up to second order. The solutions for distortions of $\boldsymbol{u}$ in the transverse plane with the nominal $\boldsymbol{E}$ and $\boldsymbol{B}$-fields parallel and in z-direction are obtained as

$$\frac{u_x}{u_z} = c_0\frac{E_x}{E_z} + c_1\frac{E_y}{E_z} - c_1\frac{B_y}{B_z} + c_2\frac{B_x}{B_z} \,, \tag{3.7}$$

$$\frac{u_y}{u_z} = c_0 \frac{E_y}{E_z} - c_1 \frac{E_x}{E_z} + c_1 \frac{B_x}{B_z} + c_2 \frac{B_y}{B_z} \ . \tag{3.8}$$

The distortions of the fields in each dimension are scaled by the constants c_0, c_1 and c_2 which are defined as

$$c_0 = \frac{1}{1 + T_2^2 \omega^2 \tau^2} \ , \ c_1 = \frac{T_1 \omega \tau}{1 + T_1^2 \omega^2 \tau^2} \ , \ c_2 = \frac{T_2^2 \omega^2 \tau^2}{1 + T_2^2 \omega^2 \tau^2} \ . \tag{3.9}$$

They contain the parameter $\omega\tau$, which is sensitive to the gas composition, and the correction terms T_1 and T_2 which account for the tensor terms of the drift velocity leading to different drift velocities in different directions [45]. For a gas mixture of Ne-CO_2-N_2, both correction terms are measured to be very close to one [47]. The distortions in z-direction are given by

$$\frac{u_z}{v_0} = \frac{v(E)}{v_0} - \frac{1}{2}\left(\hat{E}_x^2 + \hat{E}_y^2\right) + c1\left(\hat{E}_x \hat{B}_y - \hat{E}_y \hat{B}_x\right) + c_2\left(\hat{E}_x \hat{B}_x + \hat{E}_y \hat{B}_y - \hat{B}_x^2 - \hat{B}_y^2\right) \ , \tag{3.10}$$

where v_0 is the nominal drift velocity. The drift velocity $v(E) = \mu(E)E$ is a function of the electric field and it can be expanded up to second order around E_0 to $v(E) = v_0 + v'(E)(E - E_0) + v''(E)\frac{(E-E_0)^2}{2}$. The distortions of the electron drift path are calculated with Eqs. (3.7), (3.8) and (3.10) by integrating over the full drift path dL. The final distortions can be written as

$$\mathrm{d}x = \int \left(c_0 \frac{E_x}{E_z} + c_1 \frac{E_y}{E_z} - c_1 \frac{B_y}{B_z} + c_2 \frac{B_x}{B_z} \right) \mathrm{d}L \ , \tag{3.11}$$

$$\mathrm{d}y = \int \left(c_0 \frac{E_y}{E_z} - c_1 \frac{E_x}{E_z} + c_1 \frac{B_x}{B_z} + c_2 \frac{B_y}{B_z} \right) \mathrm{d}L \ , \tag{3.12}$$

$$\begin{aligned} \mathrm{d}z = \int \Bigg(& \frac{v'(E)}{v_0}(E - E_0) + \frac{v''(E)}{v_0}\frac{(E - E_0)^2}{2} - \frac{E_x^2 + E_y^2}{2E_z^2} + \\ & c_1 \frac{E_x B_y - E_y B_x}{E_z B_z} + c_2 \left[\frac{E_x B_x + E_y B_y}{E_z B_z} - \frac{B_x^2 + B_y^2}{B_z^2} \right] \Bigg) \mathrm{d}L \ . \end{aligned} \tag{3.13}$$

For small distortions, the integral can be calculated as a straight line from the point of origin of the electron. In this case, each contribution is independent and the sum can be calculated in any given order. If there are large gradients of the distortions on the other hand, the integral has to be along the real drift path in order to account for significant variations of the electric and magnetic fields as a function of the position in the drift volume. While the transverse distortions only contain a linear combination of first order terms, second order and mixed terms remain for the distortions in drift direction. A simple dimensional analysis can determine if these higher order terms are negligible, in which case the distortions in z reduce to the first derivative of the drift velocity w.r.t to the $\boldsymbol{E}$-field around E_0. Eqs. (3.11) to (3.13) can also be rotated to a cylindrical coordinate system, which becomes very useful for cylindrical TPCs. The coordinates (x, y) are mapped to (r, φ) while the fields and distortions transform from (E_x, E_y) and $(\mathrm{d}x, \mathrm{d}y)$ to (E_r, E_φ) and $(\mathrm{d}r, r\mathrm{d}\varphi)$.

3.3 Gas Amplification in Multi-Wire Proportional Chambers

The ionization created along the particle trajectory needs to be amplified in order to be able to measure it with common readout electronics. Readout chambers with amplification structures provide a simple way to multiply the primary and secondary ionization electrons by large amounts. MWPCs are widely applied as such amplification technologies although more recently, the application of Gas Electron Multiplier (GEM) foils is increasingly studied and readout chambers with an array of GEMs become more

popular as operational experience increases.

In very high electric fields, the ionization electrons collect, along one mean free path between two collisions with gas atoms, more energy than necessary to create another electron-ion pair in the second collision. Once a region with such high electric fields is reached, an avalanche of electrons is started and the charge of the initial ionization is multiplied by factors of usually several thousand. In MWPCs, the amplification takes place at the grid of anode wires (also called sense wires in literature) at positive high voltage which is mounted between the readout plane and another grid of cathode wires (or zero grid) at ground potential. The analytical description of the $\boldsymbol{E}$-field of multiple wire planes is derived in [45]. The electric field in the vicinity of an anode wire is a radial field with

$$E = \frac{\lambda}{2\pi\varepsilon_0}\frac{1}{r}\,, \tag{3.14}$$

where r is the radius at which the field is evaluated, λ is the linear charge density on the wire and ε_0 is the vacuum permittivity. The gradient of the field strongly increases as the ionization electrons radially approach the wire. For the electric fields necessary for amplification, the wires need to be as thin as a few tens of µm and potentials of the order of 1 kV need to be applied. The longitudinal extent of an avalanche usually covers $\mathcal{O}(100\,\mu\mathrm{m})$ before all electrons reach the wire surface. Several physical processes take place during an avalanche, including single and multiple ionization, optical and metastable excitations, recombination and energy transfer by collisions between atoms [45]. MWPCs are operated in proportional mode, i.e. the measured signal is proportional to the number of electrons starting the avalanche multiplied by the gain factor. This holds as long as the charge density of the avalanche is much smaller than the charge density of the anode wire so that the electric field from the avalanche is negligible compared to the field imposed by the wire. When the amplification is increased beyond the proportional mode, several effects may take place. The cloud of positive ions reduces the field between the avalanche and the wires, leading to decreased amplification for the subsequent intervals, which is also called the region of limited proportionality. On the other side of the avalanche however, the additional positive ions increase the electric field for any following multiplication processes. If the photon absorption cross section of the quencher is high, the photons in the avalanche can only start new avalanches near their origin, for which the probability is increased in the region of higher fields at the back of the initial avalanche. Therefore, backward moving multiplication processes start where the starting point moves further and further away from the wire. This effect is called limited streamer. Between the limited proportional mode and the limited streamer mode, the amplification can suddenly jump by one order of magnitude [45].

For an initial number of ionization electrons N_0 traveling a distance $\mathrm{d}s$ over which amplification takes place, the number of additional electrons $\mathrm{d}N$ created via amplification can be written as

$$\mathrm{d}N = N_0\alpha\mathrm{d}s\,, \tag{3.15}$$

where $\alpha = f(E/\rho)\rho$ is the Townsend coefficient which is proportional to the gas density ρ. The Townsend coefficient also depends on $\boldsymbol{E}$, the excitation and ionization cross sections of electrons as well as on the different ionization mechanisms discussed in Section 3.1. Therefore, it has to be measured for every gas mixture. The gain factor G is obtained by integration of Eq. (3.15) starting at the point $s_{\min}$ where the field is sufficient for amplification and ending at the wire radius a:

$$G = \frac{N}{N_0} = \exp\int_{s_{\min}}^{a}\alpha(s)\mathrm{d}s = \exp\int_{E_{\min}}^{E(a)}\frac{\alpha(E)}{\mathrm{d}E/\mathrm{d}s}\mathrm{d}E\,. \tag{3.16}$$

The integral over $\mathrm{d}s$ can be replaced by the integral over $\mathrm{d}E$ when using the gradient of the $\boldsymbol{E}$-field $\mathrm{d}E/\mathrm{d}s$, the minimum $\boldsymbol{E}$-field required for multiplication $E_{\min}$ and the field at

the wire $E(a)$. Using Eq. (3.14) to replace $\mathrm{d}E/\mathrm{d}s$ in Eq. (3.16), the logarithm of the gain factor is in first approximation proportional to the charge density λ and, therefore, to the potential applied at the anode wire [45].

4 ALICE Time Projection Chamber

The TPC [48] is the most important detector for tracking and PID in ALICE. The reconstruction and identification of particles traversing the detector volume relies on the measurement of their specific energy loss per unit path length in the detector gas and the determination of their momentum from their curvature in the magnetic field. The design is optimized to perform well in the environment of heavy-ion collisions at LHC, as charged-particle densities of up to $\mathrm{d}N_{\mathrm{ch}}/\mathrm{d}\eta = 8000$ were expected at the time of the development, achieving a $\mathrm{d}E/\mathrm{d}x$ resolution below 7 %. A relative momentum resolution of below 7 % at $p_{\mathrm{T}} = 10\,\mathrm{GeV}\,c^{-1}$ is measured using cosmic rays. The TPC is part of the ALICE upgrade project for LHC Run 3. It has been equipped with completely new readout chambers based on GEMs as well as new readout electronics, providing continuous readout of Pb−Pb collision data at interaction rates of 50 kHz [18, 19, 49].

The layout of the TPC is described in Section 4.1. Sections 4.2 to 4.4 deal with the measurement of the trajectories of charged particles and their specific energy loss per unit path length in the TPC. Possible sources for distortions of the drift field are discussed in Section 4.5, followed by an outline of detector calibration procedures in Section 4.6.

4.1 Layout

A 3D drawing of the TPC is shown in Fig. 4.1. It consists of a large cylindrical volume of about $88\,\mathrm{cm}^3$ filled with a Neon- or Argon-based gas mixture. The active volume has a length of 499.4 cm along z and covers radii between 84.8 cm and 246.6 cm. The resulting acceptance for tracks of full radial length corresponds to $|\eta| < 0.9$. The central high-voltage electrode (CE) in the center of the cylinder divides the TPC into the A and C side. A voltage of −100 kV at the CE is required to provide a uniform electric field of $400\,\mathrm{V\,cm}^{-1}$ between the end caps on both sides and the CE, which keeps the electron drift time at 91–94 µs for the full drift length, depending on the exact gas composition. A finely-segmented field cage at the inner and outer radius of the gas volume guarantees the homogeneity of the electric field across the full volume, resulting in field distortions below a factor 10^{-4} according to electrostatic calculations. The readout chambers (ROCs) are mounted at both ends of the cylinder. They are divided into 18 trapezoidal sectors in φ and, motivated by the change of the track density with the radius, into an inner and outer part covered by the Inner Readout Chambers (IROCs, $84.8\,\mathrm{cm} < r < 132.1\,\mathrm{cm}$) and Outer Readout Chambers (OROCs, $134.6\,\mathrm{cm} < r < 246.6\,\mathrm{cm}$), respectively. Each sector is defined by an index, where the index runs from 0 to 35, giving the sectors on the A side the indices 0 to 17 and those on the C side the indices 18 to 35. In addition, each IROC and each OROC are uniquely identified, using the name of the side in combination with an index running from 00 to 17, e.g. IROC A07. The Front-End Electronics (FEE), the readout and the services are mounted in the service support wheel in front of each end plate to relieve the readout chambers from additional gravitational forces.

4.1.1 Field Cage

The TPC is composed of four cylindrical vessels made of a light, rigid and gas-tight composite structure. The two field cage vessels define the gas volume of the detector and are surrounded by two containment vessels which isolate the inside of the TPC from the rest of the experiment. The surfaces of the latter are covered with 50 µm thick aluminum

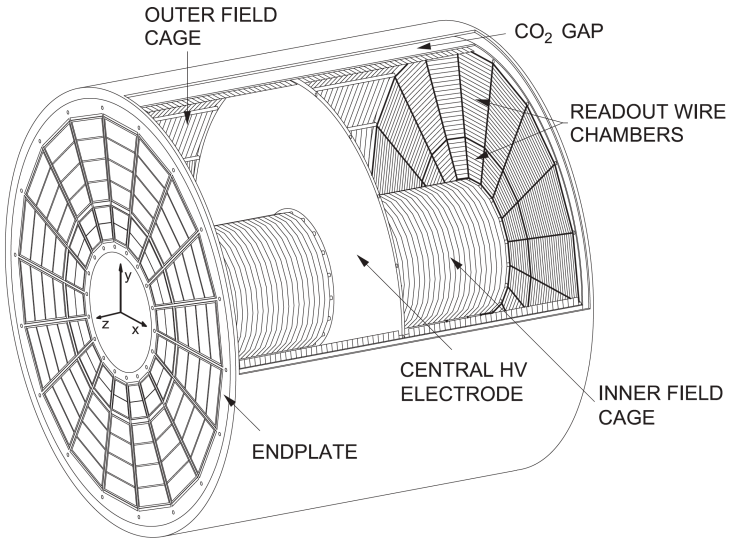

Figure 4.1: A sketch of the ALICE TPC, showing the field cage structure, the CE and the end plates with the readout chambers [48].

foil to provide good ground. A gap between the field cage vessels and the containment vessels, flushed continuously with CO_2, serves as insulation between the potentials of the field cage and the grounded containment wall. The CE is located inside the field cage vessels. It is a 23 µm thick aluminized Mylar foil glued onto a set of inner and outer aluminum rings after stretching. On both sides of the field cage walls, a set of coarsely-segmented guard rings made of 13 mm wide aluminum tape avoids charge build-up on the surfaces of the vessels. Their potentials are defined by an independent resistor chain, matching the potential gradient of the field cage. Both the inner and the outer field cage consist of 165 aluminized Mylar strips on either side of the TPC, each strip having a width of 13 mm. They are wrapped around a set of 18 rods with a pitch of 15 mm between two strips. The 166th strip close the the CE is left out due to mechanical considerations. The rods are Makrolon® tubes equally spaced at the inner and outer field cage walls between the corners of the ROCs. On each side, one of the inner and one of the outer rods houses the resistor chain providing the potentials to the field cage strips. The high-voltage cable to the CE is placed into one of the outer rods, with a spare contact in the one on the other side. Six of the outer rods per side contain the optics for the laser calibration system. The rest of the inner rods is used for gas inlets and the rest of the outer rods for gas outlets, providing a radial gas flow. As there is a gap between the OROCs and the last outer field cage strip, additional skirt electrodes minimize the field distortions in these regions. The gas-tight end plates align the field cage vessels, hold the ROCs and provide feed-throughs and flanges for gas, laser and electrical connections.

4.1.2 Readout Chambers

The readout chambers are based on MWPCs with cathode pad readout, optimized for rate capability in the high track-density environments of heavy-ion collisions. The main elements are the wire planes, which have a slightly different geometry in the IROCs and OROCs due to the radial dependence of the track density, the pad plane and the aluminum frame (Al-body).

The wires run along the azimuthal direction. There are three wire planes consisting of a plane of anode wires at high voltage to provide gas amplification of ionization electrons and a plane of cathode wires at grounded potential to separate the drift volume from the amplification region. In addition, a gating grid (GG) wire plane controls the passage of

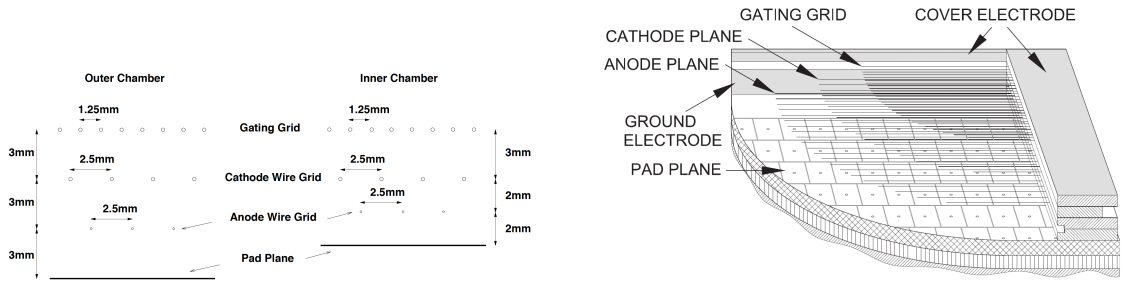

Figure 4.2: *Left:* Wire geometries applied in the IROCs and OROCs. *Right:* A schematic cross section of a ROC showing the pad plane, wire planes and the ground and cover electrodes [48].

electrons and positive ions between the drift volume and the amplification region. The constant offset voltage of the gating grid (V_{G}) of $-70\,\mathrm{V}$ in the IROCs and $-155\,\mathrm{V}$ in the OROCs is applied in the open mode, e.g. when a trigger is received, to provide full transparency for electrons from the drift region. In the absence of a trigger, the alternating bipolar bias potential of the gating grid (ΔV) is applied on top of the offset voltage, rendering the GG opaque for both electrons from the drift region and positive ions from the amplification region. Measurements of the GG efficiency show a transparency below 10^{-4} in the closed mode. The anode wires are made of gold-plated tungsten and have a diameter of 20 µm while 75 µm thick copper-beryllium wires are used for the cathode wires and gating grid. Fig. 4.2 shows the wire geometry in the IROC and OROC and a cross-section of a readout chamber. The spacing between the anode wires and the pad plane and cathode wires, respectively, is chosen to be 2 mm in the IROCs and 3 mm in the OROCs. The GG wires are mounted 3 mm above the cathode wires in both cases. The anode wire pitch corresponds to 2.5 mm to minimize the charge accumulated per unit length of wire. The cathode wires have the same pitch as the anode wires while a pitch of 1.25 mm between the GG wires allows to keep the bias voltages low. The anode and GG wires are staggered with respect to the cathode wires. The wires are stretched and glued to printed circuit board (PCB) ledges. Their ends are soldered onto copper tape strips. The cross section of an IROC shown in Fig. 4.3 indicates the different soldering points and wire ledges which are glued on top of each other as the wire grids are positioned. The soldering points for the anode and cathode wires are on opposite sides. For the GG wires, a dedicated ledge with two buses for the alternating bias potential is used. On top of the last ledge, a 1 mm thick fully metalized PCB serves as a cover electrode. The potential is adjusted to minimize distortions of the drift field at the edges of the readout chambers. The gaps for the soldering points are filled with epoxy and an extra layer (0.5 mm) of epoxy is applied as insulation of the high electric fields generated by the wire tips at the outer walls of the ledges. The total width of the wire ledges corresponds to 12 mm. Adding the gap of 3 mm between two readout chambers, there is a dead zone of 27 mm in $r\varphi$ between two ROCs. At the edges of the readout chambers in radial direction, additional ground and cover electrode strips (Fig. 4.2) are necessary to minimize drift field distortions and to prevent a leakage of amplification ions into the drift volume.

A 3 mm thick halogen-free FR4 PCB is used for the pad plane. The pad size is optimized for occupancy, signal-to-noise ratio and position resolution. There are 63 pad rows (0–62) in the IROC and 96 pad rows (63–159) in the OROC, yielding a total of 159 pad rows. Along with the particle density decreasing with the radius, the pad size also changes with the radius. All pads in the IROCs have a size of $4 \times 7.5\ \mathrm{mm}^2$ ($r\varphi \times r$). The OROCs are

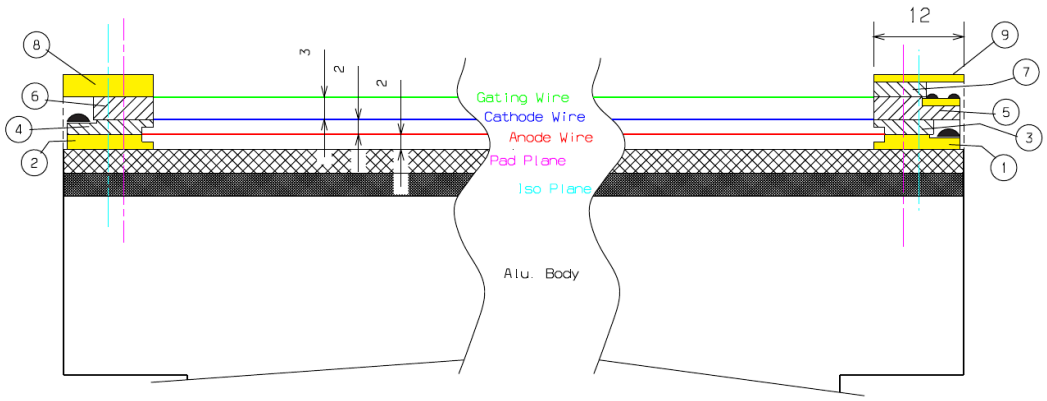

Figure 4.3: A schematic cross section of an IROC along the wires [15]. The soldering points for anode ① and cathode wires ④ are on opposite sides. Two buses for the alternating bias potential are used for the soldering of the GG wires ⑤. On top of the last ledge, metalized PCBs are used as cover electrodes ⑧ ⑨.

divided into two pad regions, OROC medium ($6 \times 10\,\mathrm{mm}^2$) and OROC long ($6 \times 15\,\mathrm{mm}^2$). On top of the pad plane, a 3 mm thick strong back made from fiberglass-epoxy and the Al-body provide stiffness against deformation due to mechanical forces and gas tightness.

4.1.3 Front-End Electronics and Readout

A total number of 557,568 pads on the pad planes are sensitive to the signals induced by the amplification of ionization electrons in the ROCs. The collected signals are transported to the Front-End Cards (FECs) for further processing via flexible Kapton cables connected to the back of the pad planes. On the FECs, the signals are amplified by a charge-sensitive amplifier with a conversion gain of 12 mV/fC followed by a semi-Gaussian pulse shaper, integrated in a custom-made chip called PASA (PreAmplifier and ShAper). The output signal of the PASA is digitized and processed in the custom-made ALTRO (Alice Tpc ReadOut) chip. The ALTRO consists of a 10 bit 25 MSPS analog-to-digital converter (ADC) operated at 10 MHz and a data processor to perform baseline subtraction, tail cancellation, zero suppression and formatting. In addition, a multi-event buffer (MEB) with four entries keeps the data stream of a full electron drift time in memory after a Level-1 trigger. Upon the arrival of a Level-2 trigger, the data is either frozen in memory, until it is fully read out, or discarded. On each FEC, there are eight PASA and eight ALTRO chips with 16 channels, respectively, resulting in a total of 4356 FECs for the full TPC. They are connected to 216 Readout Control Unit (RCU2) cards [50] providing the interface to the ALICE trigger system (CTP), Data Acquisition (DAQ) and Detector Control System (DCS).

4.1.4 Gas Mixture

The gas is the detection medium of the TPC. The choice of gas components and composition determines the ionization and transport properties of electrons and positive ions in the drift volume and the readout chambers. Therefore, the gas mixture plays a crucial role regarding the performance of the detector. The choice of the main gas component is between Ne and Ar while the only quencher which comes into question for the TPC is CO_2, excluding hydrocarbons and CF_4 due to aging effects in the MWPCs and concerns with material compatibility.

The diffusion of electrons along their drift path strongly impacts the position resolution

of the detector. Around the nominal value of the electric field of 400 V/cm, the diffusion coefficients and especially the drift velocity still depend on the electric field for mixtures of the chosen gas components. More so, they strongly depend on the exact composition, in terms of fraction of each component, as well as temperature and pressure. Primary and total ionization are driven by the ionization potentials and radiation length (X_0) of the main gas component as it is much more abundant than the quencher. The gas gain depends mainly on the Townsend coefficient but also on the Penning fraction which can change with the concentration of quencher. The ionization quantities are higher by about a factor of two in Ar, potentially increasing the position and $\mathrm{d}E/\mathrm{d}x$ resolution. However, the radiation length of Ar is three times smaller compared to Ne. As a result, the contribution of multiple scattering to the resolution is about 70 % bigger as it is proportional to $1/\sqrt{X_0}$ [45]. The ion mobility of the gas mixture is a relevant factor for the amount of positive ions which accumulate in the drift volume as space charge. The uniformity of the drift field is distorted by high amounts of positive ions (Section 4.5), leading to a deterioration of the position resolution. The mobility of the ions drifting in a Ar-CO_2 90-10 mixture is lower by a factor of about 1.72 compared to a Ne-CO_2 90-10 mixture [51]. In total, the space-charge density from primary ionization is almost 3.5 times higher in Ar-CO_2 (90-10). It is discussed in [46] that the drifting ions actually are $CO_2{}^+$ ions respectively $CO_2{}^+$-ion clusters as the Ne^+ or Ar^+ ions transfer their charge to CO_2 molecules on time scales much shorter than the ion drift time.

Throughout LHC Runs 1 and 2, the gas composition in the TPC was adapted several times for different reasons. The design gas mixture Ne-CO_2-N_2 (90-10-5) was used in 2010. The CO_2 concentration is chosen by the resulting electron drift velocity to achieve drift times below 100 µs. The addition of a small fraction of N_2 decreases the electron drift velocity by about 5 % but allows a more stable operation of the ROCs at high gain, having slightly better quenching capabilities at the excitation energies of Ne than CO_2. The N_2 was removed in 2011 to 2013, following discharges which caused damage to the preamplifiers. The actual reason for the damage were filter capacitors in the high-voltage distribution, which were also removed. High currents and chamber trips remained during the operation with Ne-CO_2 (90-10). After careful evaluation of space-charge effects due to primary ionization and $\mathrm{d}E/\mathrm{d}x$ and tracking performance, the main gas component was changed from Ne to Ar for the start of LHC Run 2. The gas mixture of Ar-CO_2 (88-12) has very similar electron transport properties as the Ne-based mixtures but about twice as much primary and total ionization per unit length [18]. This allows to operate the ROCs at lower gain for the same signal-to-noise ratio. A much more stable operation without any significant chamber trips was observed during the years 2015 and 2016. However with the use of Ar, large space-charge distortions appeared in localized regions of the TPC, which is extensively discussed in Chapter 5. These distortions are smaller by about an order of magnitude with the Ne-based gas mixtures, going unnoticed during the data taking at generally lower interaction rates in LHC Run 1. A change to Ne-CO_2-N_2 (90-10-5) in 2017 allowed to gain a better understanding of the mechanisms behind the large local space-charge distortions, but high currents and high-voltage trips re-occurred as a consequence. After developing a strategy to mitigate the space-charge distortions, the gas was changed back to Ar-CO_2 (88-12) in 2018 to guarantee stable operation at unprecedented collision rates during the last heavy-ion period of LHC Run 2.

The exact gas composition is monitored at all times with a precision of 0.1 % of absolute content in the gas mixture. The diagnostic tools include a gas chromatograph and the drift velocity measurement from the laser system. The gas is wetted with about 100 ppm of water to avoid charging-up of insulators, while the oxygen content typically is around 1–2 ppm minimizing the probability for electron attachment. The ambient temperature

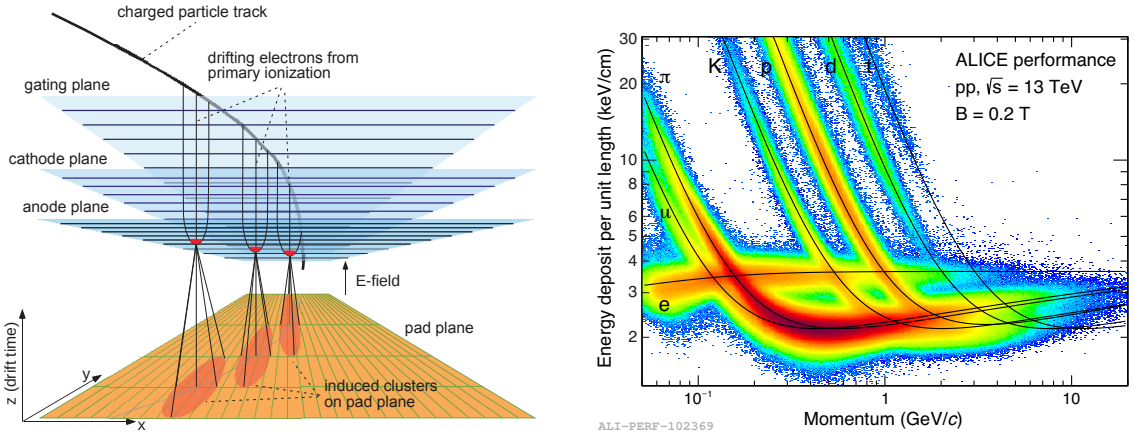

Figure 4.4: *Left:* The sketch shows the measurement technique of a TPC. Ionization electrons created along the trajectory of a charged particle in the active gas volume drift along the electric field towards the ROCs. Passing the GG and cathode wires, they are amplified at the anode wires, which induces a signal on the pads. The reconstructed clusters and the reconstructed trajectory in the (local) xy-plane are indicated on the pad plane. The z-coordinates is derived from the drift time of the ionization electrons. *Right:* The energy deposit per unit length $\mathrm{d}E/\mathrm{d}x$ of particles in the ALICE TPC as a function of the particle momentum, measured in pp collisions at $\sqrt{s} = 13$ TeV with a magnetic field of $B = 0.2\,\mathrm{T}$ [25]. The black lines represent the parameterization in Eq. (4.5)

and pressure inside the TPC are also monitored and the signals are calibrated accordingly.

4.2 Operating Principle

The schematic drawing on the left of Fig. 4.4 outlines the measurement of a charged particle with the TPC. Particles emitted from the interaction vertex traverse the active gas volume of the TPC. They lose energy in collisions with the gas atoms according to the Bethe-Bloch equation, ionizing them and creating primary ionization electrons and positive gas ions. The specific energy loss per unit path length $\mathrm{d}E/\mathrm{d}x$ of particles in matter is discussed in Section 3.1. It depends on the particle velocity and on the material, i.e. the gas, and is of the order of keV/cm in the gas mixtures used in the ALICE TPC. Depending on the energy of the primary ionization electron, it can ionize several other gas atoms, creating a cloud of primary and secondary ionization electrons. The positive ions move along the uniform electric field towards the CE while the ionization electrons drift towards the ROCs. The motion of electrons and ions in a gas under influence of electric and magnetic fields is described in Section 3.2. The mobility μ of electrons in the TPC gas mixtures is about three orders of magnitude larger than for ions, resulting in corresponding differences in the drift velocity and in the deflection due to magnetic field components not parallel to the electric field. In addition, the diffusion of electrons along their drift path is relevant w.r.t. the intrinsic space-point resolution of the TPC. If a positive trigger signal is received the gating grid is opened for a time period equivalent to the maximum electron drift time. The ionization electrons reach the region inside of the ROCs and are multiplied by gas amplification at the anode wires (Section 3.3). As the amplification takes place at high electric fields close to the anode wires, the avalanche electrons are quickly absorbed by the wires. The amplification ions remaining in the vicinity of the wires induce a fast-rising positive signal on the pads and drift towards the pad plane, cathode wires or gating grid, depending on their initial position and the exact field configuration. The movement of

the ions induces a long signal tail with an amplitude much smaller than the one of the original signal and a length of $\mathcal{O}(10\text{–}100\,\mu s)$ corresponding to the time until the ions reach the different electrodes [52]. The wire and pad geometry is chosen such that the induced signal is usually spread over three pads and three time bins. In each pad row, a software cluster finder identifies signals from adjacent pads and time bins which belong together and groups them to one cluster. The position of the cluster on the pad plane and in drift direction (z) is calculated via its center of gravity, using the time of the collision to convert the drift time of the electron to its initial z-position. Each cluster contains information about the integrated charge and the maximum amplitude of the signal, which respectively, after normalization, can be used to derive the specific energy loss per unit path length. After combining clusters from the same particle trajectory at different pad rows (Section 4.3), the specific energy loss per unit path length of the reconstructed track can be calculated from up to 159 samples (Section 4.4), corresponding to the total number of pad rows. In addition to the $\mathrm{d}E/\mathrm{d}x$ measurement, the curvature of the reconstructed track in the magnetic field provides information about the momentum of the particle, allowing to separate the different particle species as shown in the right plot of Fig. 4.4.

4.3 Tracking

The track finding in the TPC is performed in the local coordinate system of the corresponding sector and follows the Kalman-filter approach, a method for simultaneous track recognition and fitting [27]. The trajectories of charged particles can be parameterized by a helix as they are bent by the magnetic field. The following set of five parameters is chosen to define the state vector $\boldsymbol{x}^{\mathrm{T}}$ of a track at each x:

$$\boldsymbol{x}^{\mathrm{T}} = (y, z, \sin\varphi, \tan\lambda, \frac{q}{p_{\mathrm{T}}}) \,, \tag{4.1}$$

where x, y and z represent the track position in the local coordinate frame, $\sin\varphi = \frac{x_{\mathrm{local}} - x_0}{R}$ is the inclination angle of the momentum vector with respect to the pad row, defined by the x-position x_0 of the helix center and the radius R of the track curvature, $\tan\lambda = \frac{p_z}{p_{\mathrm{T}}}$ is the dip angle, defined by the transverse and z-component of the momentum vector, and $\frac{q}{p_{\mathrm{T}}} = \frac{1}{BR}$ is proportional to the inverse product of the magnetic field B and the curvature radius. The helix is then parameterized by

$$\begin{aligned} y(x) &= y_0 - R\sqrt{1 - \sin^2\varphi} \,, \\ z(x) &= z_0 + \tan\lambda\, R\, \sin\varphi \,, \end{aligned} \tag{4.2}$$

where y_0 and z_0 are the positions of the helix center [53].

The Kalman filter requires the reconstruction of cluster positions and uncertainties as well as track seeds to be used as starting points. The high occupancies of up to 40 % (20 %) in the IROCs (OROCs) may lead to a loss of clusters due to tracks overlapping or a displacement of clusters, effectively decreasing the efficiency of the Kalman filter. Therefore, the seeding procedure is performed at the outer pad rows to reduce the combinatorics and to provide seeds with a quality as high as possible. Between two clusters in pad row i and $i - n$, clusters are assigned to the seed if they are found within a defined search road. If the number of assigned clusters for a seed is bigger than $n/2$ the seed is accepted as a good track candidate, otherwise it is rejected [18].

A track hypothesis is assigned to each track candidate. According to the current track hypothesis, the track is propagated inwards and the estimated track parameters and covariance matrix at the next pad row are calculated, accounting for multiple scattering and energy loss under the assumption that the particle is a pion. Within a window

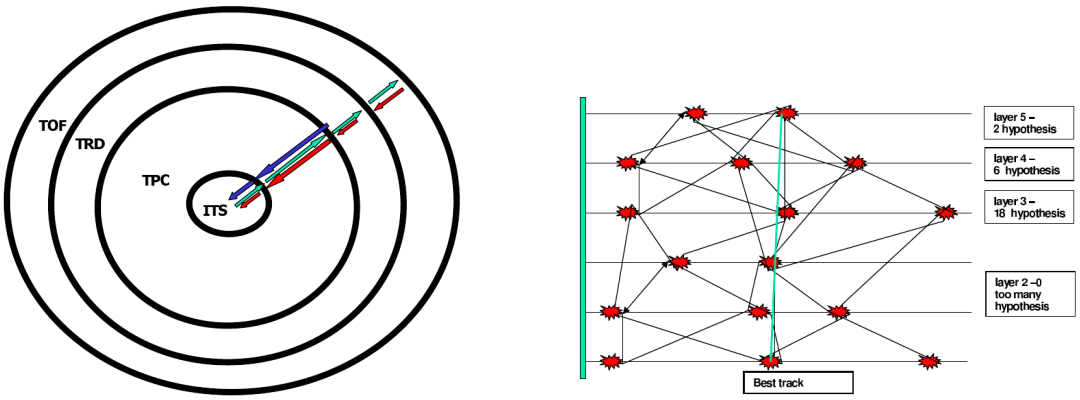

Figure 4.5: *Left:* A schematic sketch of the global tracking procedure. The tracking starts from the outside of the TPC towards the ITS and primary vertex. Then the tracks are propagated back outwards from the ITS to the TOF. In a final refit, the track is propagated from the TOF to the primary vertex again. *Right:* An illustration of the track matching and finding procedure in the ITS. Several track hypothesis are followed through the different ITS layers, selecting only the best one when reaching the innermost layer [54].

defined by the predicted track and cluster errors at the given pad row, the cluster with the smallest χ^2 value is assigned to the track if the square of the residuals in both directions are smaller than the estimated 3σ. The track parameters and covariance matrix are updated with the assigned cluster and the procedure is repeated at the next pad row down to the innermost pad row. The track hypothesis is removed if no clusters are assigned at several consecutive pad rows. In case the fraction of shared clusters between two tracks from different track hypotheses is bigger than a defined threshold, the systematic analysis of the cluster shape and charge can be used to determine if two close tracks overlap or if it is the same track. In the latter case, the track with the smaller χ^2 or significantly larger number of assigned clusters is chosen.

The full reconstruction of tracks is performed in three iterations as is indicated in Fig. 4.5 (left). First, the tracks are followed from the outside of the TPC through the ITS to the primary vertex. In a second iteration, the track is propagated back and updated from the ITS through the TPC and TRD to the TOF. In a final step, a refit of the track is performed propagating from the outside towards the primary vertex. This procedure requires the extrapolation and matching of the tracks in the TPC to the other detectors.

The extrapolation from the TPC to the ITS is difficult because of the distance between the sensitive elements and high track densities in the ITS. In addition, multiple scattering in the TPC field cage and vessels contributes significantly to the extrapolation error. As multiple scattering increases with decreasing momentum, tracks with higher momentum are propagated first. The track finding procedure used in the ITS is illustrated in Fig. 4.5 (right). In contrast to the tracking inside the TPC, not only the cluster with the smallest χ^2 is assigned once the track is propagated to the next ITS layer but a tree of track candidates is built from all clusters with a χ^2 below a given limit. This approach is followed through all the ITS layers, explicitly using a vertex constraint, which leads to an increasing number of track candidates with each layer. Therefore, only the best track candidates are kept according to a χ^2 criterion, choosing the most probable in the end. The best short tracks are also kept as secondary track candidates for

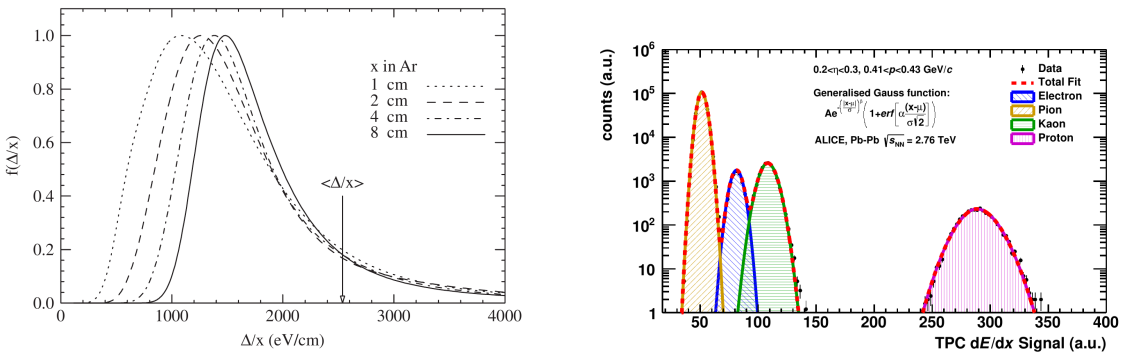

Figure 4.6: *Left:* Calculated straggling functions $f(\Delta/x)$ for particles ($\beta\gamma = 3.6$) traversing Ar [56]. The different lines represent segments of different length x. The mean value $\langle\Delta/x\rangle$ is the same for all x and is indicated by the arrow. The most probable value depends on x and is clearly different from the mean. *Right:* The dE/dx signal measured with the TPC for momenta between 0.41 GeV/c and 0.42 GeV/c [52]. The colored lines represent the fits of the dE/dx signal for different particle species by a generalized Gauss function. The sum of the fits is indicated by the red line which is in very good agreement with the data points.

further V0 analysis [54]. A similar approach is also used for the propagation of the tracks in the TRD [55].

4.4 dE/dx Measurement

The mean specific energy loss per unit path length can be derived from the Bethe-Bloch equation (Section 3.1). In the TPC, the charge deposited along a particle trajectory by ionization of the gas provides the dE/dx information. The charge distribution is described by a straggling function with a long tail towards high values as shown in Fig. 4.6 (left). It is a convolution of the distribution of the number of collisions in a track segment and the energy loss spectra for multiple collisions [56]. Therefore, the most probable value gives a much better estimate of the mean dE/dx than the mean value of the distribution. The TPC dE/dx signal of a particle is calculated via the truncated mean [15]

$$\langle Q\rangle_f = \frac{1}{fn}\sum_{i=1}^{fn} Q_i \,, \tag{4.3}$$

which provides a good approximation of the most probable value, with $f = 0.6$, $Q_i \leq Q_{i+1}$ and the total number of clusters n assigned to the track. The distribution of $\langle Q\rangle_f$ of a particle species with a given momentum perfectly fits the shape of a generalized Gauss function with its mean equal to the mean specific energy loss per unit path length $\langle$dE/d$x\rangle$. Fig. 4.6 (right) shows the $\langle$dE/d$x\rangle$ of different particles in a fixed momentum interval measured with the TPC and the corresponding fits. The dE/dx resolution $\sigma_{\langle \mathrm{d}E/\mathrm{d}x\rangle}$ is defined by the variance of the Gaussian distribution which depends on the number of samples, the pad size and the gas pressure. The dE/dx resolution at the MIP position can be used as a reference for the dE/dx performance of the TPC. Another way to quantify the dE/dx performance at a given momentum is the separation power S of two particle species A and B [57]:

$$S_{\mathrm{A,B}} = \frac{\langle \mathrm{d}E/\mathrm{d}x\rangle_{\mathrm{A}} - \langle \mathrm{d}E/\mathrm{d}x\rangle_{\mathrm{B}}}{0.5\cdot(\sigma_{\langle \mathrm{d}E/\mathrm{d}x\rangle_{\mathrm{A}}} + \sigma_{\langle \mathrm{d}E/\mathrm{d}x\rangle_{\mathrm{B}}})} \,. \tag{4.4}$$

In Eq. (4.3), the value Q_i represents the charge of cluster i of the sample of n clusters assigned to the track. Either the total charge of the TPC cluster (Q_{tot}) or the maximum amplitude of the charge signal of the TPC cluster (Q_{max}) can be used as an estimator for the $\mathrm{d}E/\mathrm{d}x$. In general, Q_{tot} is the more precise estimator as it takes into account the total charge deposited in the cluster. However, the probability of clusters overlapping increases in high-density environments like central Pb−Pb collisions, which affects the Q_{tot} measurement of a single cluster. A better performance is achieved using the Q_{max} estimator in Pb−Pb collisions [27] while Q_{tot} is used to calculate the $\mathrm{d}E/\mathrm{d}x$ in low multiplicity environments like pp collisions.

The $\mathrm{d}E/\mathrm{d}x$ measurement with the TPC in pp collisions and with a magnetic field of $B = 0.2\,\mathrm{T}$ is shown by the plot on the right of Fig. 4.4. The additional information of the momentum allows to separate the different particle species. The ALEPH parameterization of the Bethe-Bloch equation (Eq. (3.2)) is used for the $\mathrm{d}E/\mathrm{d}x$ measurement with the ALICE TPC [45, 15]:

$$f(\beta\gamma) = \frac{P_1}{\beta^{P_4}} \left(P_2 - \beta^{P_4} - \ln\left(P_3 + \frac{1}{(\beta\gamma)^{P_5}} \right) \right) , \tag{4.5}$$

with $\beta = v/c$, $\gamma = 1/(1-\beta^2)$ and five free parameters P_i.

4.5 Space-Point Distortions

The electric field inside the active gas volume of the TPC is defined by the potential at the CE, the potentials at the field cage strips of the inner and outer field cage and the potentials at the ROCs, i.e. at the wires, cover and skirt electrodes. The voltages of the different electrodes are chosen to set the nominal drift field to $400\,\mathrm{V/cm}$ which, in the ideal case, is homogeneous in the whole volume, parallel to the z-axis and aligned with the B-field. Ionization electrons drift with a constant drift velocity along straight lines to the ROCs where their point of origin in the r-$r\varphi$ plane and in z can be precisely reconstructed.

A bias in the space-point measurement has implications on the accuracy of the $\mathrm{d}E/\mathrm{d}x$ and momentum measurement as they essentially rely on the reconstruction of the space points along the particle trajectories (Sections 4.3 and 4.4). Inhomogeneities and distortions of the $\boldsymbol{E}$ and $\boldsymbol{B}$-fields cause distortions of the ideal drift path and changes of the drift velocity and the diffusion of the ionization electrons. Furthermore, the drift velocity and the diffusion are subject to inhomogeneities (in the volume) and variations (in time) of the environmental conditions, i.e. temperature, pressure and gas composition. Due to those effects, the reconstructed position of clusters can suffer distortions in radial direction ($\mathrm{d}r$), distortions in azimuthal direction ($\mathrm{d}r\varphi$) and distortions in drift direction ($\mathrm{d}z$), according to Eqs. (3.11) to (3.13). Consequently, the position resolution can deteriorate and the track reconstruction, momentum resolution and the track length $\mathrm{d}x$ in the calculation of the specific energy loss per unit path length are affected.

4.5.1 Influence of Environmental Conditions

The dependence of the drift velocity and diffusion on the gas composition and the homogeneity of the temperature inside the TPC drift volume have been extensively studied in [58]. The drift velocity changes by about 6 % (1 %) per 1 % change in the CO_2 (N_2) concentration. The temperature gradients can be monitored by several temperature

sensors inside the TPC and turn out to be of the order of 0.1 K within the full volume, which is the required value to reach the desired space-point precision of 200 µm [15]. The exact gas composition, the temperature inside the TPC and the cavern pressure are continuously monitored and the respective values are stored in the offline conditions database (OCDB) with a time granularity of $\mathcal{O}(1\,\text{min})$. Furthermore, the laser calibration system provides fast feedback about the drift velocity, which allows to compensate variations due to pressure changes by adjusting the concentration of the gas components. The most precise method to calibrate the drift velocity is based on the differences between the track parameters of TPC tracks and the corresponding ITS tracklets, which is described in Section 4.6.1.

4.5.2 Design Imperfections

The design of the field cage and the ROCs has been carefully optimized, as described in Section 4.1, in order to keep distortions of the drift field due to mechanical imperfections to a minimum. Still, unavoidable local inhomogeneities of the electric field are caused by the finite width of the field cage strips and the distance between them. It is shown in [58] that the resulting relative deviations in the active volume are of the order of 10^{-4} and below while increasing up to 10^{-2} close to the strips. Distortions at the edges of the readout chambers caused by the space between the last field cage strips and the ROCs as well as by the space between the ROCs themselves are minimized by the additional cover and skirt electrodes. The field generated by the high voltage of the anode wires can reach into the drift volume due to the finite pitch of the GG wires. The global homogeneity of the drift field is unaffected by this and the field itself can be tuned by setting the voltages of the GG wires accordingly. The field distortions due to the imperfections described in this subsection are constant in time and considered as static distortions.

4.5.3 Imperfections of the Magnetic Field

Since the TPC is located inside the L3 magnet, deviations from the ideal magnetic field, which is aligned with the nominal electric field in z-direction, deflect the ionization electrons from their original drift path. When there are $\boldsymbol{B}$-components perpendicular to the electric field, the $\boldsymbol{E}\times\boldsymbol{B}$ term in the solution of the Langevin equation (Eq. (3.5)) leads to electron velocity components in the corresponding $\boldsymbol{E}\times\boldsymbol{B}$-direction, as described in Section 3.2. The magnitude of the deflection then scales with the Lorentz angle which is proportional to $\boldsymbol{B}$ and the electron mobility in the gas mixture and with the drift length if there is a global misalignment of the $\boldsymbol{B}$ and $\boldsymbol{E}$-vectors. The Lorentz angle calculated with Magboltz [59] for $\boldsymbol{B}\perp\boldsymbol{E}$ takes values of 0.32, 0.34 and 0.36 for Ne-CO_2-N_2 (90-10-5), Ne-CO_2 (90-10) and Ar-CO_2 (88-12), respectively [60]. The magnetic field has been measured at several points inside the magnet and a parameterization of this survey is implemented in the ALICE calibration software. The inhomogeneities are within 2 % as shown in Fig. 4.7. The resulting distortions in radial and azimuthal direction are plotted in Fig. 4.8 and are of the order of several mm [58]. Small asymmetries of the $\boldsymbol{B}$-field components between A and C side due to the inhomogeneities of the solenoid and due to minor contributions from the dipole on the C side lead to the step at $z = 0$ and to differences of the distortions which are usually below 100 µm. As the magnetic field is expected to be constant over time, the distortions due to its inhomogeneities contribute to the static distortions.

4.5.4 Misalignment of Potentials

A uniform drift field requires perfect alignment of the defining elements, i.e. the CE, the field cage and the ROCs. A misalignment due to, for example, a shift of one of these elements corresponds to a shift of its potential at the nominal position, leading to local and global distortions of the electric field [61]. These distortions are considered static as

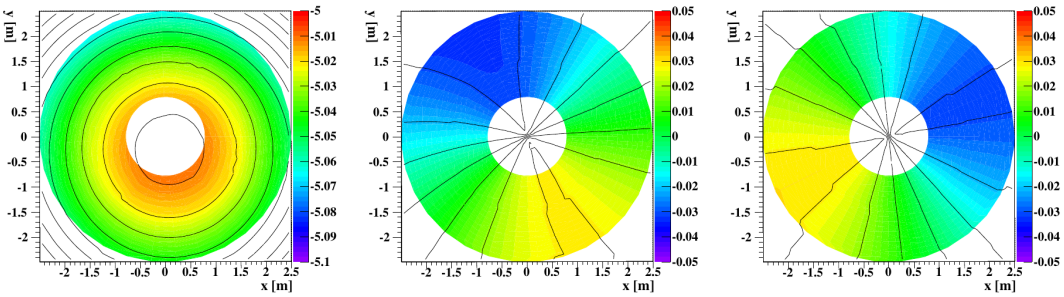

Figure 4.7: The magnetic field components B_z (*left*), B_r (*middle*) and B_φ (*right*) in the TPC volume in kGauss (color scale) as a function of the x- and y-position close to the CE [58]. The solid lines represent equipotentials. Small deviations of B_r and B_φ from zero imply a misalignment to the nominal $\boldsymbol{E}$-field along z, resulting in $\boldsymbol{E}\times\boldsymbol{B}$-effects.

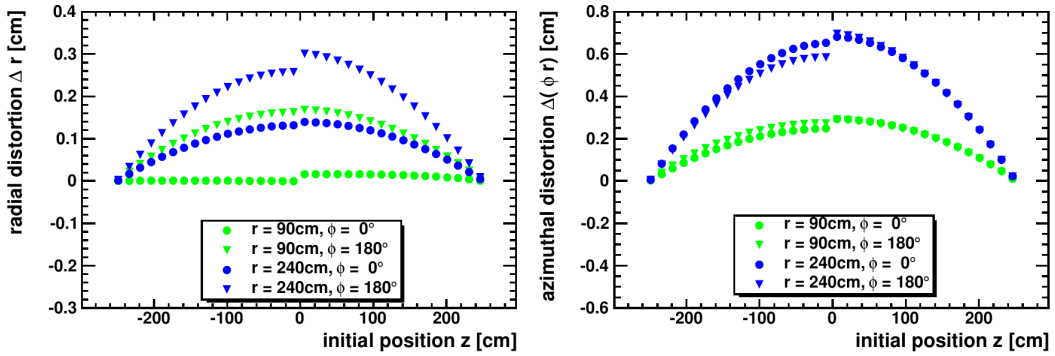

Figure 4.8: Calculated distortions due to the inhomogeneities of the magnetic field as a function of the z-position at fixed r and φ [58]. *Left:* Radial distortions Δr (dr). *Right:* Azimuthal distortions $\Delta(\phi r)$ (d$r\varphi$).

the alignment is fixed once the TPC and the other detectors are installed in the cavern.

A conical deformation, e.g. a shift of the inner field cage vessel with respect to the outer field cage vessel, results in a modification of the nominal boundary potentials since the whole cylinder follows this deformation. This scenario is illustrated in Fig. 4.9 (left). Possible voltage misalignment scenarios at the field cage strips are shown in Fig. 4.9 (right). They can happen due to rotated clips, where both ends of a field cage strip are improperly combined, or due to shifted rods, where also the strips can follow the shift of the rod. The strips themselves were positioned with a precision of 50 µm during the construction of the field cage. Concerning the ROCs, they can be misaligned with respect to the CE due to a linear shift in z or due to a rotation around either or both of their axes (Fig. 4.10). The shifted z-position of the ROCs then implies distortions of the reconstructed cluster position due to a convolution of two effects. First, the modified electric field leads to deviations from the nominal drift velocity and, second, the drift distance deviates from the nominal value. In addition, a misalignment between the chambers themselves leads to local distortions of the electric field at their boundaries. During the mounting procedure of the readout chambers, they were aligned with respect to each other and to the CE with a precision of 250 µm by specially machined shims at three points of each chamber [15]. The resulting distortions of the electric field are of the same order of magnitude as the precision of the ROC alignment [61].

A broken resistor in the resistor chain defining the potentials at the field cage strips or two shorted strips would result in a change of the total resistance of the resistor chain

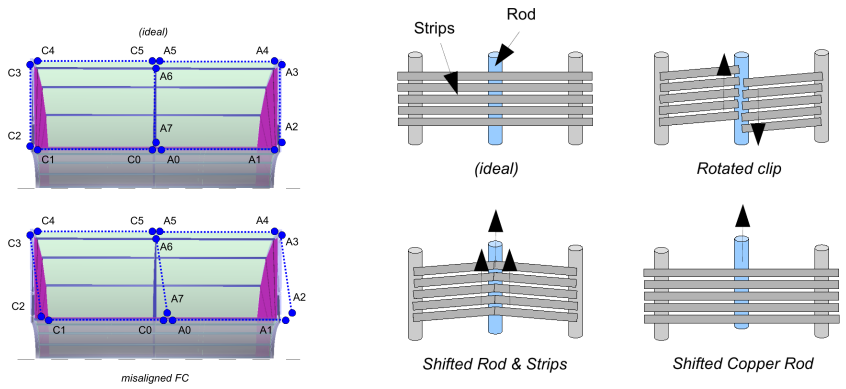

Figure 4.9: *Left:* A shift of the inner field cage vessel with respect to the outer field cage vessel leads to a misalignment of the boundary potentials Ai and Ci. *Right:* A misalignment of the nominal potentials by a rotated clip, a shifted rod or a shifted rod and strips leads to distortions of the electric field [61].

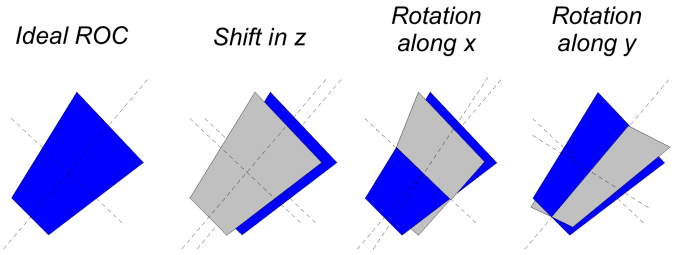

Figure 4.10: The ROCs can be misaligned in z by a constant shift or by a rotation along the x or the y-axis [61].

and a non-linear voltage drop at the respective position. Fig. 4.11 shows that, in case of two shorted strips at z=150 cm, the expected distortions of the measured cluster position are of the order of two time bins (corresponding to ≈5 mm) and close to 1 cm in radial distortion [61].

4.5.5 Charge-Up Effects

There is a possibility that the drifting charges end up at an insulating surface exposed to the active volume. If this is the case, an accumulation of charge on this surface can lead to electric fields high enough to affect the nominal field defined by the electrodes inside the drift volume. In order to avoid such a scenario, the design was optimized to keep the probability for charge-up effects to a minimum, e.g. the guard rings avoid a charge build-up at the walls of the field cage vessels and the surfaces of the outer field cage rods which match the area covered by the field cage strips are coated with copper. A similar situation can arise when an electrode is disconnected from its power source, for example due to a mechanical issue at a contact. Since its potential is then undefined and floating, the nominal electric field is distorted by definition and charge can accumulate on its surface.

Distortions due to charge-up effects have rather long time constants. The surfaces charge up over time until the net-charge accumulation is zero and an equilibrium state sets in. The distortions of the drift field then reach a saturation value, the amplitude of which is

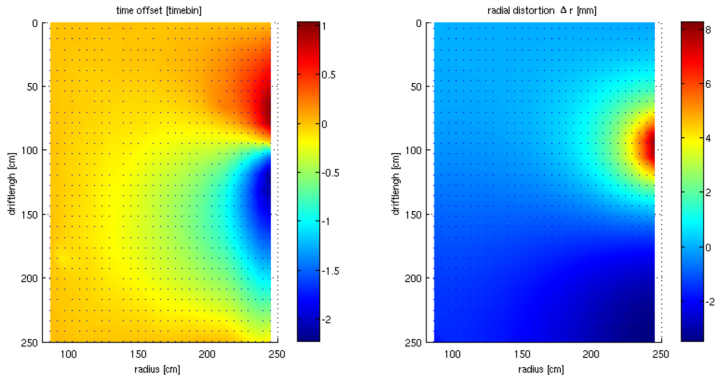

Figure 4.11: The distortions (color scale) of the reconstructed space-point position as a function of the drift length and the radius due to two shorted field cage strips at z=150 cm [61]. *Left:* Distortions in drift direction (time offset) expressed in units of time bins (1 time bin = 100 ns $\approx$ 2.5 mm). *Right:* Distortions in radial direction Δr (corresponding to dr).

determined by the amount of ionization created in the drift volume, i.e. the particle flux from collisions.

4.5.6 Space Charge

The presence of positive ions (space charge) inside the drift volume of the TPC modifies the nominal electric field and distorts the drift path of the ionization electrons. There are three processes that can contribute to the space-charge density in the TPC:

- **Primary ionization:** Ions created inside the drift volume via ionization by traversing particles.
- **Ion feedback:** A fraction of amplification ions from clusters created inside the ROC volume in previous events will enter the drift volume once the gating grid is opened by an event trigger.
- **Ion backflow (IBF):** A constant flow of amplification ions from the ROCs to the CE in case there is no protection by a gating grid.

In general, the ions drift from their point of origin towards the CE, making the ion drift time one of the driving factors of the total space-charge density. The drift time of ions for the full drift length is of the order of 160–200 ms in Ne-CO_2-N_2 (90-10-5) and even higher in Ar-based mixtures. The total space-charge density at any given moment consists of the accumulation of ions from several events. For example, assuming an ion drift time of 200 ms and a typical interaction rate of 8 kHz in Pb−Pb collisions, ions from 1600 events contribute to the space-charge density. Since the mobility of the ions is about 2000 times smaller than the one of electrons, the distribution of space charge in the TPC volume can be assumed to be constant over the drift time of ionization electrons from the same event. Over time scales larger than the electron drift time however, the space-charge density may change according to the interaction rate, the multiplicity and topology of the contributing events, and other quantities which are subject to variations like the charge deposit along a single track. Therefore, the distortions due to space charge are considered as a dynamic problem. The average space-charge density usually changes over time scales of $\mathcal{O}$(min) and larger due to global properties like the interaction rate while there are also fluctuations on time scales much smaller than the ion drift time which can become significant for certain scenarios, e.g. in case of IBF [18].

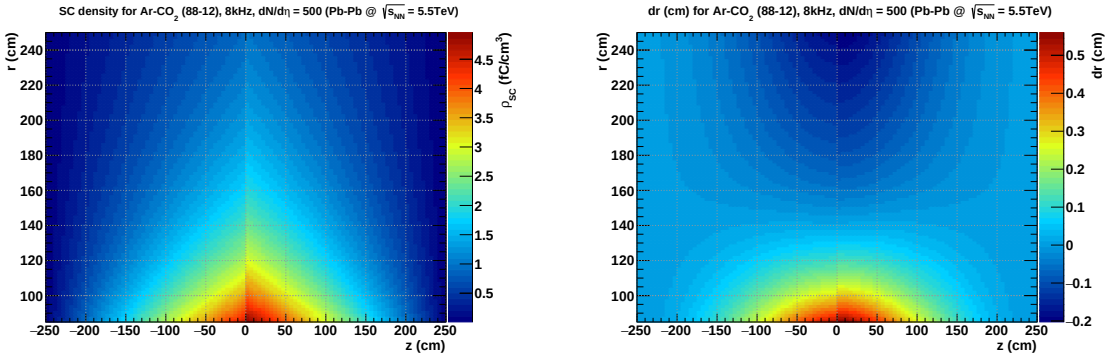

Figure 4.12: The space-charge density ρ_{SC} (*left*) and the corresponding radial distortions dr (*right*) (color scale) as a function of the radius r and z-position [62]. The space-charge density is calculated according to Eq. (4.6) for Pb−Pb collisions at 8 kHz, average charged-particle densities of $\mathrm{d}N_{\mathrm{ch}}/\mathrm{d}\eta = 500$ and a TPC gas mixture of Ar-CO_2 88-12.

The distribution of ions from primary ionization follows the topology of the events and can be parameterized, assuming certain symmetries, by

$$\rho_{\mathrm{SC}}(r,z) = \frac{a - b \cdot |z|}{r^d} \,, \tag{4.6}$$

where a and b are constants depending on the multiplicity, interaction rate and detector geometry, z and r are the positions in the TPC along the drift and radial direction, and the constant d defining the radial dependence is experimentally found to be between 1.5 and 2. While the $\frac{1}{r^d}$-dependence originates in the track density decreasing with the radius, the z-distribution of a single event is flat. Assuming a uniform distribution of collisions in time, the accumulation of space charge due to ions from single events drifting towards the CE and the overlap of several events from different moments in time results in the linear z-dependence of Eq. (4.6) with a maximum close to the CE [63]. The expected space-charge density according to Eq. (4.6) and corresponding radial distortions are shown in Fig. 4.12 for Pb−Pb collisions at the top LHC Run 2 interaction rate of 8 kHz and charged-particle densities of $\mathrm{d}N_{\mathrm{ch}}/\mathrm{d}\eta = 500$. While the distortions are comparable or smaller than the space-point resolution (≈1 mm) in most of the TPC volume, they take values up to 5 mm at the inner part close to the CE. This region shows the biggest space-charge distortions because the charge densities increase with decreasing radius and the distortions are integrated over long drift paths. As the space-charge density from primary ionization on average is symmetric along phi, the resulting electric field only has components in radial and drift direction. Due to the presence of the $\boldsymbol{B}$-field in drift direction however, there are also distortions in azimuthal direction which roughly scale with $\omega\tau$, according to Eqs. (3.11) to (3.13).

The distributions of ion feedback and IBF are essentially the same. They are determined by the event topology, the gain and the transparency of the gating grid in the open mode which depends on the exact voltage configuration. According to electrostatic calculations, 10–15 % of the ions created in an avalanche process drift back into the drift volume when the gating grid is left open [60]. The additional contribution of ion feedback or IBF to the space-charge density from primary ionization (Eq. (4.6)) can be approximated by a constant term which is independent of z and has the same $\frac{1}{r^d}$-dependence. The local variations of the gain and the GG transparency can add additional local variations along φ and r. The magnitude of the IBF is strongly dependent on the particle flux in the TPC volume and the interaction rate as the ionization electrons from every event create a disc

of ions inside the ROCs which is slowly drifting towards the CE. The contribution of ion feedback also depends on the particle flux inside the ROC volume and the interaction rate but, contrary to the IBF, it is limited by the trigger rate or GG opening frequency and time. Therefore, it is much smaller than the contribution from primary ionization.

The deviations from the nominal electric field are given by the electric field generated by the space charge. It can be obtained analytically by

$$\boldsymbol{E} = -\vec{\nabla}\phi \,, \tag{4.7}$$

where ϕ is the electrostatic potential which can be derived from a given space-charge density ρ_{SC} by solving the Poisson equation

$$\nabla^2\phi = -\frac{\rho_{\mathrm{SC}}}{\varepsilon_0} \,, \tag{4.8}$$

where ε_0 is the vacuum permittivity. A multi-grid Poisson relaxation method is implemented in the ALICE offline calibration and analysis framework (AliRoot) [64] to provide a numerical solution of the Poisson equation on a regular grid, which can be used to calculate the $\boldsymbol{E}$-field deviations and space-point distortions due to arbitrary space-charge densities [18].

4.6 Detector Calibration

The TPC $\mathrm{d}E/\mathrm{d}x$ signal is extracted from the signal induced on the pads by ionization electrons. The characteristics of the signal show a dependence on the operational parameters, environmental conditions and other factors related to the track topology and properties of the collision. In addition, variations of the induced signal and the response of the electronics due to manufacturing tolerances, mechanical imperfections or physics effects as well as distortions of the drift field (Section 4.5) have direct impact on the precision of the cluster position and the $\mathrm{d}E/\mathrm{d}x$ signal. In order to achieve the desired precision, all relevant effects and dependencies are corrected and calibrated either online or offline.

The time scales of the different calibrations are quite different as there are time-independent and time-dependent influences. For example, the cluster charge is correlated to the gain of the given pads. The relative gain differences between single readout channels are given by the readout geometry and the electronics response, which are fixed during the construction phase and are constant for a given detector configuration. Calibration intervals are usually in the order of hours, i.e. on the run level, up to yearly. The absolute gain, however, depends on the temperature and pressure of the gas and its composition. As the pressure inside the cavern follows the atmospheric pressure variations, the calibration intervals for the temperature and pressure correction are of the order of minutes (see Section 4.6.2). The dependencies between the calibration parameters themselves require the re-calibration of several parameters after changing one of them. The data to perform the detector calibration are either obtained in dedicated calibration runs, from frequent measurements of the required information during data taking or from the data itself in special calibration passes during the reconstruction. The calibration data is stored in special machines for upload to the electronics and in the OCDB to be applied during offline reconstruction.

Zero suppression is performed on the level of the FEE to reduce the amount of the raw data. The pedestal and noise values of each readout channel are measured in dedicated calibration runs and are defined by the mean and the sigma of the baseline distribution. The average noise corresponds to the design specifications and is below one ADC channel

in all three pad regions. The zero-suppression threshold is set at three sigma of the baseline distribution. Shaping variations of the different electronics channels affect the measurement of the drift time. They are determined in calibration pulser runs, injecting a pulse to the cathode wires and measuring the arrival time distribution of this signal. The width of the distribution corresponds to about 5 ns or approximately 140 µm, which makes this a second order correction compared to the space-point resolution after diffusion [15]. The laser calibration system provides straight laser tracks at well defined positions via two-photon ionization of organic impurities (<1 ppm) in the TPC gas. Furthermore, scattered photons create photo electrons at the CE which themselves create a coincident signal on all pads. Data from special laser runs are used to calibrate the alignment between the ROCs. During collision data taking, a fixed number of laser shots is fired every hour. The arrival time of the CE signal can be used as a first estimate of the drift velocity [65].

The following two subsections outline the procedures for the space point and $\mathrm{d}E/\mathrm{d}x$ calibrations which are essential to obtain the desired detector performance.

4.6.1 Space-Point Calibration

The space-point distortions due to space charge in the TPC drift volume became significant in LHC Run 2 compared to the space-point resolution without space charge, as the interaction rates increased up to 8 kHz in Pb−Pb collisions and the gas mixture was changed to Ar-CO_2. In addition, high amounts of space charge caused distortions of the order of several cm in specific regions of the TPC, which is discussed in Chapter 5. In order to restore the intrinsic space-point resolution (200 µm) of the TPC, a dedicated calibration procedure for space-charge distortions [62] is applied during reconstruction, which is based on the calibration method foreseen for the TPC upgrade [18].

The space-point calibration relies on parameterized correction maps as a function of the local cluster coordinates to correct the measured position of each TPC cluster. The correction maps are calculated from the residuals between the distorted clusters associated to TPC tracks and the track position extrapolated from the corresponding ITS, TRD and TOF tracks. Large distortions imply the risk of wrongly attaching a cluster to a track or missing clusters belonging to a track. In order to assure a good cluster-to-track association in the TPC, an initial correction based on a pre-calculated correction map for a given interaction rate and collision system, which is stored in the OCDB, is performed before the TPC tracking. Since the size of the space-charge distortions depends on the interaction rate, the pre-calculated map is scaled to the current interaction rate measured by the experiment to maximize the precision of the initial correction. Therefore, the time-dependent space-charge distortions have to be disentangled from the static distortions which do not scale with interaction rate. Special runs at very low interaction rates are taken regularly for each configuration, e.g. $\boldsymbol{B}$-field polarity or collision system, as references without space-charge effects to extract the correction maps for the static distortions. These are subtracted from the pre-calculated (high interaction-rate) correction maps used for the initial correction. To first approximation, the resulting corrections then include only the space-charge distortions, for which the scaling with the interaction rate is valid. The final correction is performed by extraction of the residual corrections from the data itself after the initial correction and successful tracking. Besides the space-charge distortions correction, this calibration procedure contains several other components of the space-point calibration, including alignment, T0, drift velocity and $\boldsymbol{E}\times\boldsymbol{B}$-effects.

The procedure to calculate the correction maps is outlined in Fig. 4.13. It starts with the tracking in the TPC with relaxed tolerances for the cluster-to-track association. The

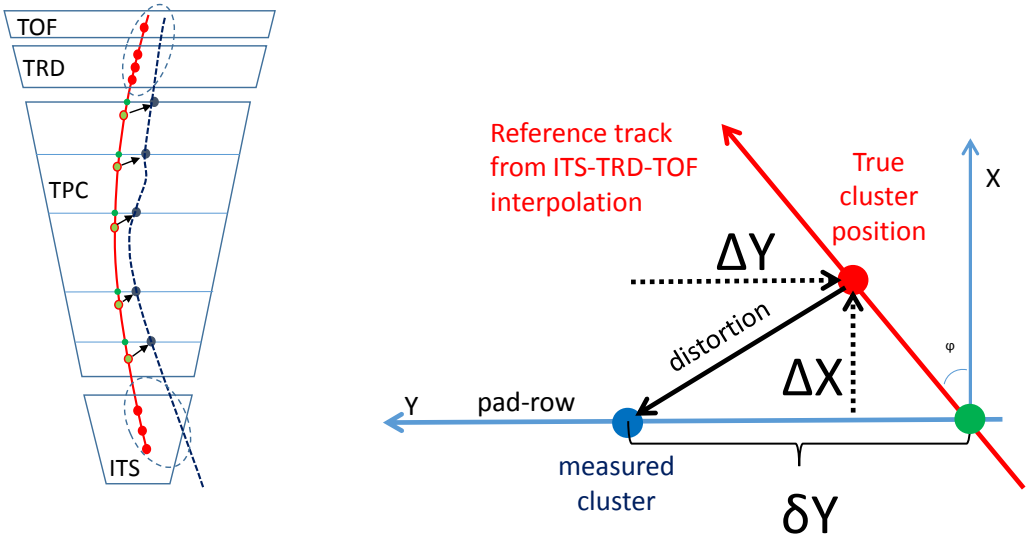

Figure 4.13: The sketch on the *left* illustrates the procedure to calculate the correction maps for the TPC space-point calibration. The ITS, TRD and TOF tracks (red points and line) are matched to the distorted TPC track (blue dotted line) and extrapolated to each TPC pad row to obtain a reference for the non-distorted track position (green points). The residuals between the non-distorted track position and the distorted TPC clusters (blue points) are calculated. The geometrical relations of Eq. (4.9) between the measured cluster residuals δY and δZ and the inclination and dip angles φ and λ provide the real distortions ΔX, ΔY and ΔZ (equal to dr, d$r\varphi$ and dz) to calculate the true position of the TPC clusters (green points with red circles), which is shown for ΔX and ΔY on the *right* [62].

estimated cluster error is artificially increased in addition to the intrinsic position resolution and the widths of the search-roads for clusters are expanded to ensure successful track finding in the presence of large space-charge distortions. Special events with low multiplicity and a cut on the number of primary particles are selected for this procedure in Pb−Pb data to minimize the clusters wrongly attached to tracks. Relaxed tolerances are applied again to match the distorted TPC tracks to tracklets in the ITS, TRD and TOF. The ITS and TRD+TOF points, respectively, are refitted by a Kalman filter. The obtained tracks are extrapolated to each TPC pad row to provide an estimate of the non-distorted track position, using the weighted mean of both extrapolations. The residuals δY and δZ in the local coordinate frame are stored for all clusters of each track and outliers due to wrong cluster-association are removed by a moving median filter. Dividing the volume of each TPC sector into 3-dimensional voxels of pad row, y/x and z/x, δY and δZ are collected for each voxel and the average residuals per voxel are obtained. In the presence of radial distortions, the real corrections in all three dimensions ΔX, ΔY and ΔZ can be calculated from the 2-dimensional residuals δY and δZ according to

$$\begin{aligned} \delta Y &= \Delta Y - \Delta X \tan\varphi \,, \\ \delta Z &= \Delta Z - \Delta X \tan\lambda \,, \end{aligned} \tag{4.9}$$

where φ is the inclination angle of the track with respect to the pad rows and λ is the dip angle. While there are tracks with different inclination angles in each voxel due to different curvatures in the magnetic field, the λ coverage depends on the z/x position and

width. Therefore, the corrections ΔX and ΔY are obtained from the parameters of a robust linear fit of the residuals δY as a function of $\tan\varphi$. Then, ΔZ is calculated by correcting the average residuals $\langle \delta Z \rangle$ for the contribution of ΔX by the average dip angle $\langle \tan\lambda \rangle$ of the voxel. Finally, the corrections extracted in every pad row are smoothed and parameterized by a Chebyshev polynomial interpolation to allow fast querying of the corrections ΔX, ΔY and ΔZ as a function of pad row, y/x and z/x.

The desired precision of the correction maps of below 200 µm determines the required statistics in terms of number of tracks which is needed for their extraction. Depending on the voxel size, collision system, interaction rate and trigger configuration, the time intervals to collect the necessary amount of data are between 20 and 40 min. Regarding the large space-charge distortions, they are subject to large space-charge density fluctuations of the order of 25 % on time scales much shorter than the calibration interval. In order to quantify the effect of fluctuations, a robust estimate of the dispersion of ΔY is also calculated. As distortion fluctuations affect many clusters of each track in a correlated way, the contribution from the estimated distortions added to the cluster error during the TPC tracking underestimates the effect of fluctuations on the track kinematics. Therefore, the correlation terms of the covariance matrix are estimated, assuming 100 % correlation, and added to the covariance matrix of the tracks obtained with uncorrelated errors. While this method is still unable to correct the effects of space-charge density fluctuations on the level of space points, it minimizes their effect on the precision of the track propagation and on the track matching to the external detectors. The performance of the correction procedure can be demonstrated by the bias and resolution of the distance of closest approach (DCA) in the bending plane of TPC tracks to the primary vertex, which is shown in Fig. 4.14. Regions with large distortions are clearly visible for the uncorrected points while the correction of the average distortions restores the intrinsic performance. However, the DCA resolution is still strongly affected by the space-charge distortion fluctuations.

Although the space-point calibration procedure achieves the required performance for the correction of the average distortions for a given calibration interval, its precision is limited by some assumptions and additional effects. As already discussed in the paragraphs above, the statistics requirement and long calibration intervals prevent the distortion correction on time scales of the order of the distortion fluctuations. Other time-dependent effects like charge up of surfaces fall in the same category as they are also averaged over the full calibration interval and can be further smeared out in case of large space-charge distortion fluctuations. Since the relevance of charge-up effects increases with the interaction rate, they are convoluted with the space-charge distortions after subtraction of the correction map for static distortions. This implies that the scaling of the correction map for the initial correction with the interaction rate is invalid because the space-charge distortions depend differently on the interaction rate than the distortions due to charge-up effects. Regarding the space-charge distortions themselves, the scaling with the interaction rate is only applicable within a short interval around the reference interaction rate. They show non-linear behavior over larger ranges and saturate with increasing space-charge density. The saturation originates to some extent from the limit of the distortions due to the boundary conditions but, depending on the actual origin of the space charge, there can be other contributing factors. The linear decomposition of the space-charge distortions and the static distortions assumes that distortions due to boundary effects are far away from regions with space-charge distortions. Once this assumption is broken, the distortions from these two effects are additive only locally.

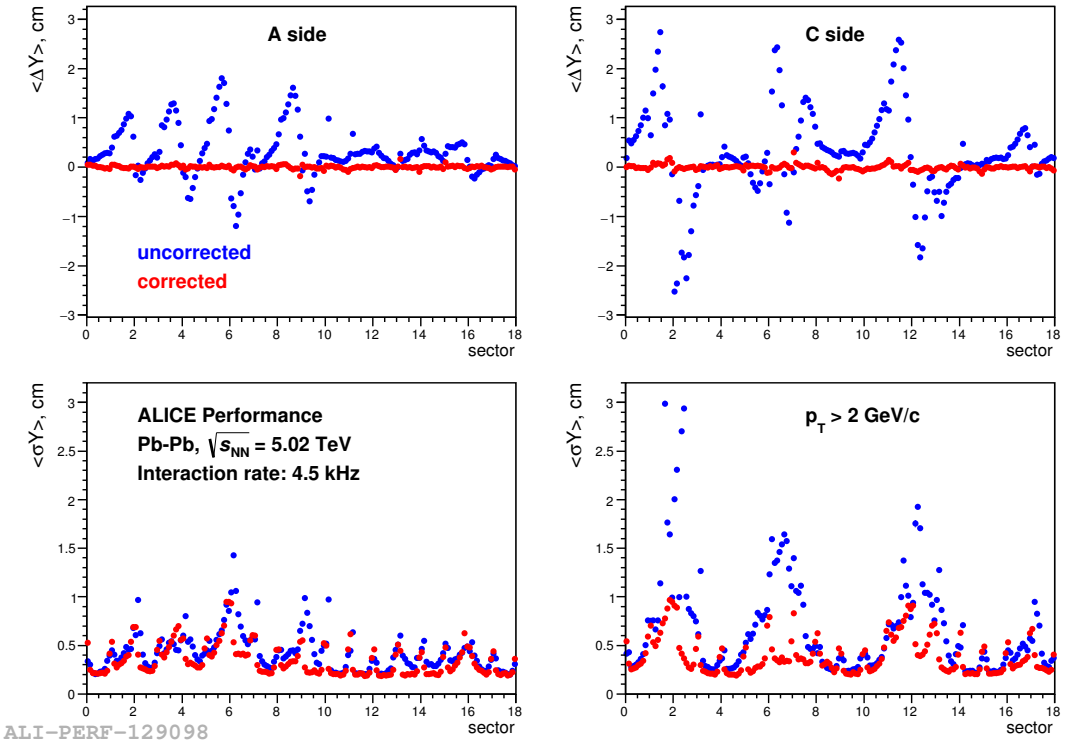

Figure 4.14: The average DCA bias $\langle \Delta Y \rangle$ (*top*) and resolution $\langle \sigma Y \rangle$ (*bottom*) in the bending plane for high momentum tracks on the TPC A side (*left*) and C side (*right*) in 2015 Pb−Pb data at 4.5 kHz interaction rate. The blue points represent the uncorrected data and the red points show the results after the space-point calibration. While the space-charge distortions are corrected on average, effects of distortion fluctuations are still visible in the DCA resolution.

4.6.2 dE/dx Calibration

The measured dE/dx signal depends on the total gain which can vary for each pad and is composed of the amount of charge induced on the pads and the response of the electronics. The gain needs to be calibrated with a precision of 1.5 % on a pad-by-pad level to achieve the required dE/dx-performance. The absolute gain factor of each pad is obtained by the measurement of the decay spectrum of radioactive krypton ($^{83}_{36}$Kr) released into the TPC gas system. The pad-by-pad calibration constants are defined by the mean of a Gaussian fit to the main peak of the spectrum. The measurement is performed at three different gains to provide the possibility to interpolate the calibration factors for any given high-voltage configuration in-between. The variations in the gain map extracted from the krypton calibration reflect mechanical deformations and imperfections within a given readout chamber, e.g. as a result of wire sag and electrostatic forces, and variations between the different chambers. Systematic differences within one chamber as well as the variations of the average gain between different chambers are of the order of 10–25 % [15]. The calibration data can be used to adjust the high voltage of single ROC in order to equalize the average gain over the full TPC.

Relative variations of the gas gain follow the relative change of the gas density which, for an ideal gas, is proportional to the ratio of pressure and temperature ($\frac{P}{T}$) [45]. As the temperature inside the TPC is monitored and controlled with a precision of 0.1 K, the decisive factor is the relative variation of the pressure. The time-dependent gain calibration is performed using the data itself. The dE/dx signals of MIPs (pions) are collected over time intervals between 5 and 15 min. The time dependence of the average

$\mathrm{d}E/\mathrm{d}x$ signal, equal to the mean of a Gaussian fit, correlates to the pressure variations in time and allows to normalize the measured $\mathrm{d}E/\mathrm{d}x$, choosing an arbitrary normalization value of 50 for MIPs. Over longer time scales, variations of the gas composition also contribute to the gain variations [66].

The projected length $\mathrm{d}x$ of a trajectory along a given pad row depends on the inclination angle φ of the track with respect to the pad row. The same geometrical dependence of the dip angle λ is given in the rz-plane. Therefore, the amount of charge deposited on a given wire by a particle with a given $\mathrm{d}E/\mathrm{d}x$ and the induced signal are calibrated for the topology of the tracks and the readout geometry. The reconstructed Q_{max} and Q_{tot} values are then a function of the width of the signal, the relative position of the cluster, the inclination and dip angle of the track and the length of the pad. In addition, a second order correction is applied for which the calibration parameters are determined for each pad region individually. They can be extracted from high-momentum cosmic tracks which provide a uniform coverage of all angles and drift lengths. Furthermore, the calculation of Q_{tot} accounts for pads with charge below the threshold.

Electron attachment by electronegative pollutants (O_2 and H_2O) in the TPC gas affects the $\mathrm{d}E/\mathrm{d}x$ signal. The attachment probability approximately scales linearly with the drift length and depends on the concentration of the pollutants which can change with time. The $\mathrm{d}E/\mathrm{d}x$ signal of MIPs as a function of the drift length is parameterized by a linear fit which is then used for calibration. The obtained cluster-loss probability due to electron attachment is of the order of $10^{-4}\,\mathrm{cm}^{-1}$ and has a rather small impact on the $\mathrm{d}E/\mathrm{d}x$ resolution.

Two effects become significant in the high-multiplicity and high particle-flux environment of Pb−Pb collisions compared to pp. First, there is an increased probability that two clusters overlap. Overlapping clusters are removed from the $\mathrm{d}E/\mathrm{d}x$ calculation as they would bias the $\mathrm{d}E/\mathrm{d}x$ towards higher values and the fraction of their charge belonging to the given track can only be approximated by models or assumptions. A cut based on the width σ_{meas} of the measured cluster relative to the expected width σ_{exp} is applied on all clusters according to $\sigma_{meas}/\sigma_{exp} < 1.5$. Second, the drift of amplification ions induces a negative undershoot on the pads following the positive signal, which is called ion tail. The amplitude of the ion tail is of the order of the electronics noise and it extends over several tens of µs. The shape depends on the relative pad position, the readout geometry, the voltage settings and the gas mixture. Furthermore, avalanche electrons arriving at an anode wire cause a drop of the potential of all the anode wires of the given segment, which is quickly ($\mathcal{O}(<100\,\mathrm{ns})$) restored by the power supply. Due to the capacitive coupling between anode wire segments and the corresponding pads, a negative common-mode signal is induced on all pads belonging to the wire segment, which depends on the charge deposited on the anode wires and the number of pads of the given segment. The consequences of the ion-tail and common-mode effects are a shift of the baseline and additional fluctuations. Threshold effects can bias the amplitude of subsequent signals, and therefore the $\mathrm{d}E/\mathrm{d}x$, towards lower values or clusters may even be entirely lost. Extensive studies of the ion-tail and common-mode effects and the development of a correction procedure is presented in [52]. The correction relies on the time response functions measured in non-zero-suppressed laser data and the assumption of charge conservation on a given anode wire segment.

5 Space-Charge Distortions in the TPC

The TPC ROCs showed instabilities during the operation with Ne-based gas mixtures in LHC Run 1, observing high currents and frequent trips of the high-voltage power supplies. The interaction rates provided by the LHC machine were significantly increased up to 8 kHz in Pb−Pb collisions in Run 2 compared to a maximum of about 1 kHz in Run 1. In order to ensure the stable operation of the TPC and avoid partial loss of data due to chamber trips at the increased interaction rates, the main component of the TPC gas was changed from Ne to Ar, as discussed in Section 4.1.4. The higher probability of multiple scattering in the Ar-CO_2 mixture is compensated by the higher amount of ionization electrons, leading to a tracking and $\mathrm{d}E/\mathrm{d}x$ performance which is comparable to the one with the Ne-CO_2 mixture. The drift field distortions due to the higher amount of space charge from primary ionization, shown in Fig. 4.12, are of the order of the space-point resolution of about 1 mm (taking into account diffusion) in a limited fraction of the TPC volume. They posed no risk of a deterioration of the space-point resolution after calibration.

In the first data at high interaction rate of LHC Run 2, large distortions of the drift field of the order of a few cm were observed. Fig. 5.1 illustrates the situation at the beginning of Run 2 data taking and shows the DCA distribution of TPC tracks extrapolated to the primary vertex in the bending plane as a function of φ for positively and negatively charged tracks in one exemplary run. The DCA in the bending plane reaches the maximum value of 3 cm in some φ regions, beyond which tracks were disregarded. The explicit pattern of the distortions and the fact that they occur only in specific regions of the TPC strongly indicate that their origin is an effect other than space charge from primary ionization. The consequences of such distortions are the deterioration of the space-point resolution, the probability to lose clusters or tracks in the affected regions and a reduced matching efficiency to the external detectors, all of which scale with the size of the distortions and, in the end, lead to a decreased $\mathrm{d}E/\mathrm{d}x$ and PID performance of the TPC. In addition to providing the means to correct the space-point distortions, the development of the space-point calibration procedure described in Section 4.6.1 also allows to determine the location of the distortions within the TPC and to measure their size with high precision. The studies presented in this chapter focus on the analysis of these distortions and their dependence on a number of variables with the goal to identify their origin and find ways to reduce them in order to minimize their impact on the performance of the TPC. It will become evident that the large distortions are caused by space charge created via gas amplification of ionization electrons at the outside edge of certain IROCs due to mechanical imperfections. In addition, two adjacent floating GG wires in the OROCs of sector 24 render the gating grid inefficient in that particular location, leading to a backflow of amplification ions created at the anode wires. The knowledge about the responsible mechanisms offers strategies for mitigation. The number of ionization electrons reaching the given spots in the IROCs is limited by adjusting the voltage of the cover electrodes, reducing the amount of space charge and, therefore, the size of the distortions. Similar results are achieved in OROC C06 by adjusting the high voltage and the voltage at the GG wires.

The details of the method used to analyze the distortions and its precision are discussed in Section 5.1. The space-charge distortions observed in Run 2 with Ar-CO_2 are presented in Section 5.2, showing their general dependencies, e.g. on the interaction rate,

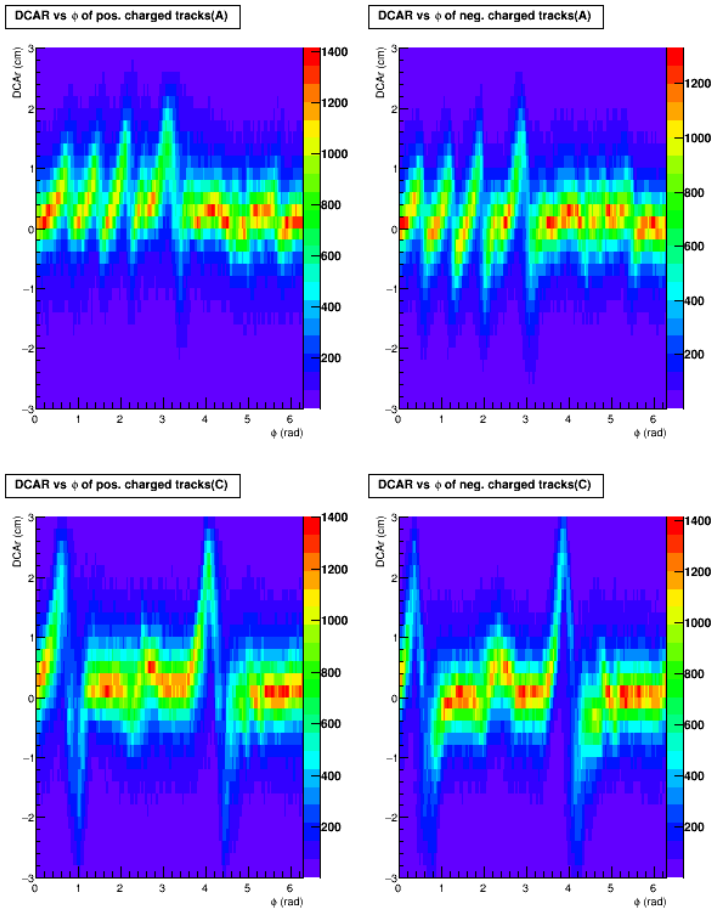

Figure 5.1: The DCA in the bending plane ($DCA\mathrm{r}$) as a function of φ for positively (*left*) and negatively (*right*) charged tracks on the A (*top*) and C (*bottom*) side. The plots show data which are not corrected for space-charge distortions from pp collisions at 200 kHz interaction rate taken in 2015.

on the $\boldsymbol{B}$-field polarity or on the collision system. They are compared to the space-charge distortions with Ne-based gas mixtures observed in Runs 1 and 2 in Section 5.3. Data from special runs taken to study and understand the dependence of the distortions on the operational parameters of the TPC are analyzed in Section 5.4. Section 5.5 and Section 5.6 focus on the origin and mitigation of the space-charge effects in the IROCs. Possible ways to mitigate the distortions due to floating GG wires in OROC C06 are investigated in Section 5.7. With the knowledge obtained from the variety of studies, new nominal operational settings are defined to minimize the space-charge distortions in the IROCs and OROCs. The results are illustrated in Section 5.8.

5.1 Distortion Analysis

The space-point calibration method described in Section 4.6.1 provides correction maps averaged over defined calibration intervals. These data are correlated to the distortions and they are used to analyze and study them. It is important to consider that the distortions have the opposite sign and are a function of the origin of the electrons, whereas the corrections are measured at the arrival point of the electrons which is equal to the distorted coordinate. The data presented in this analysis are the measured corrections while their interpretation always refers to the distortions. The correction maps are divided into small three-dimensional voxels. In radial direction, there are 159 bins in total, corresponding to one voxel per pad row. In each of the 36 sectors, there are

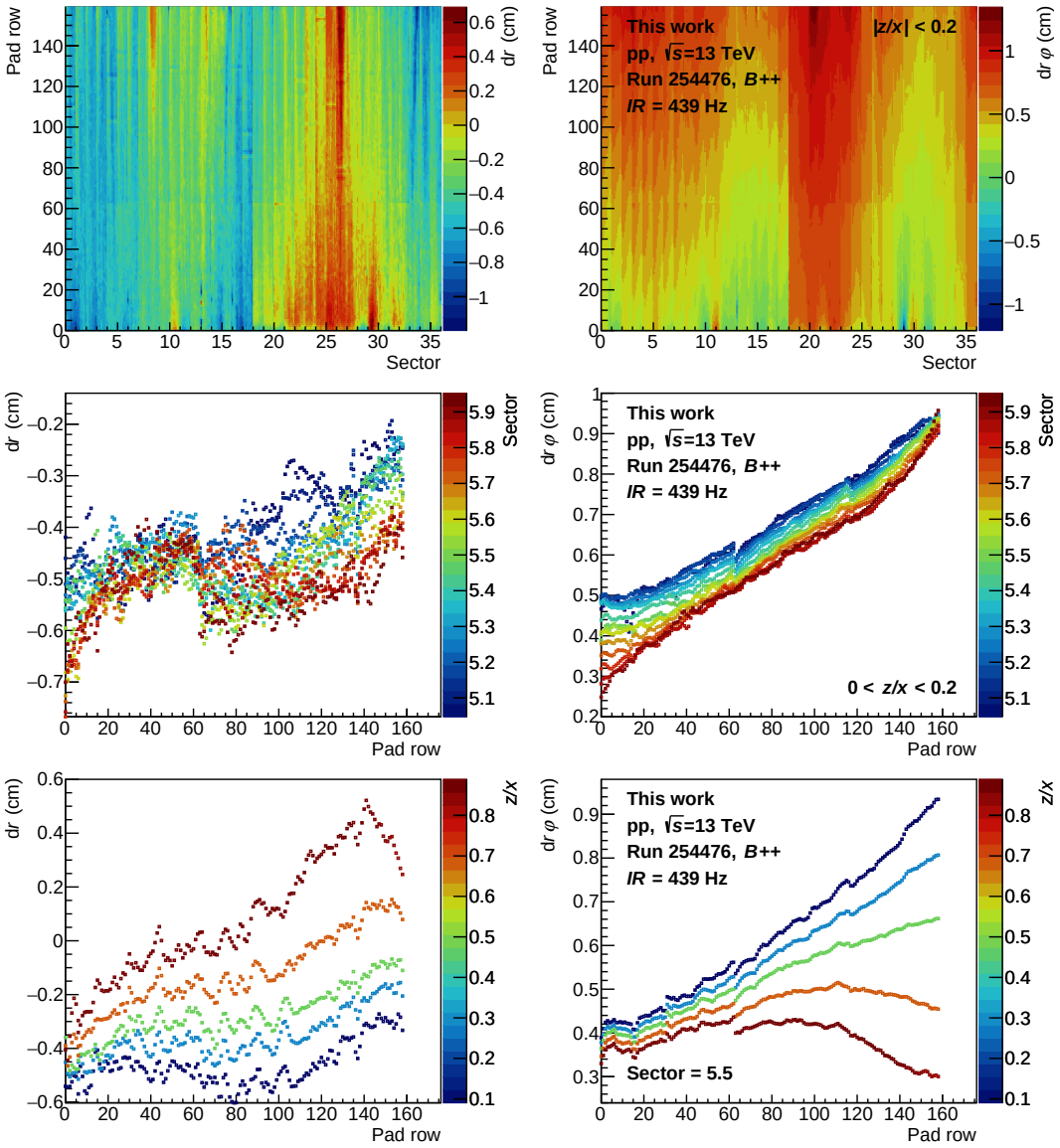

Figure 5.2: The distortions dr (*left column*) and d$r\varphi$ (*right column*) measured with nominal positive $\boldsymbol{B}$-field ($B{+}{+}$) in pp collisions at an interaction rate of 439 Hz. They are shown as a function of the pad row and the sector for one z/x bin (*top row*), as a function of the pad row and all sector bins of sector 5 for one z/x bin (*middle row*), and as a function of the pad row and z/x for one sector bin of the same sector (*bottom row*). At interaction rates that low in pp collisions, the measurement only includes the distortions due to static and misalignment effects.

15 bins in φ expressed in the local coordinates y/x or the fractional sector number coordinates. In order to maximize the number of voxels within the full acceptance ($|\eta| < 0.9$), the third dimension is chosen to be the polar angle expressed in the local coordinates z/x, using 5 bins for the A and C side, respectively. The length of the calibration interval is determined by the desired precision and the trigger configuration and is usually in the range of 20–40 min, requiring between 2 and 4 million tracks to extract the corrections with a precision of the order of 50 µm in each voxel. During the course of Run 2, there were several short time periods specially allocated for the investigation of the space-charge distortions. Those allowed to study the dependence of the distortions on all free TPC parameters and the interaction rate. Applying a high-multiplicity trigger for those runs, the required statistics were collected within a

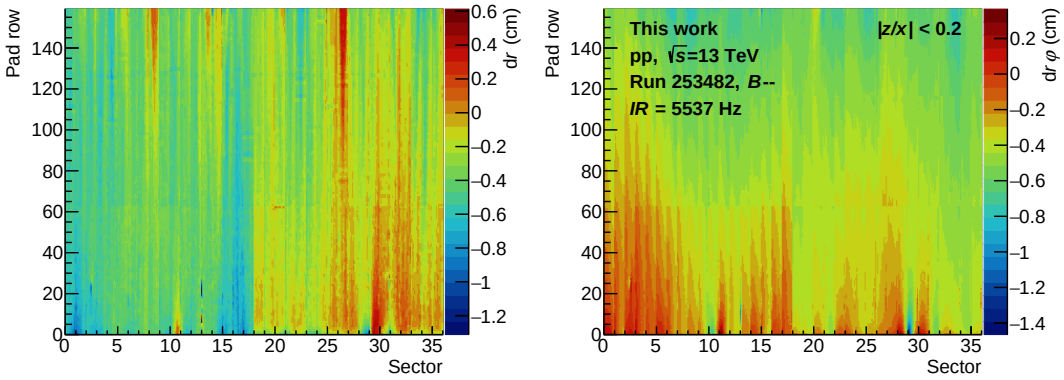

Figure 5.3: The distortions dr (*left*) and d$r\varphi$ (*right*) as a function of the pad row and the sector for one z/x bin, measured with nominal negative $\boldsymbol{B}$-field ($B--$) in pp collisions at an interaction rate of 5.5 kHz.

typical duration of 10 min.

The correction maps include distortions from all effects discussed in Section 4.5 combined, i.e. static distortions, possibly charge-up effects and space-charge distortions, but also the misalignment between the TPC and the external detectors enters into the measurement. In order to isolate the space-charge distortions from all other effects for these studies, reference maps without space-charge effects are subtracted. They are obtained by data at sufficiently low interaction rate since the distortions due to space charge start to become noticeable only at interaction rates higher than a threshold. This threshold depends on the collision system, the TPC gas mixture and the $\boldsymbol{B}$-field polarity.

The distortions in the reference map, taken with nominal $\boldsymbol{B}$-field of 0.5 T with positive polarity (denoted as $B++$), for pp collisions in 2016 are illustrated in Fig. 5.2. They amount to several mm up to 1 cm and show clear local and global dependencies on the radius, φ and z/x. While the local patterns are mostly caused by radial and azimuthal $\boldsymbol{E}$-field components due to imperfections of the electric field, the global dependencies have their origin in the inhomogeneities of the $\boldsymbol{B}$-field and the misalignment between the detectors. When reversing the polarity of the $\boldsymbol{B}$-field, the $\boldsymbol{E}\times\boldsymbol{B}$ terms change their sign, affecting mostly the azimuthal distortions as shown in Fig. 5.3.

The reference distortions are expected to be stable over short-term and long-term time scales. Therefore, the reference maps are only updated when the running configuration changes, i.e. collision system, $\boldsymbol{B}$-field polarity or TPC operational parameters. Nevertheless, additional data at low interaction rate are recorded directly before and after periods dedicated to the studies of space-charge distortions, ensuring that the reference maps and the maps with space-charge distortions are taken under the same conditions.

5.1.1 Precision of the Distortion Measurement

The correction maps are extracted from the residuals between measured TPC clusters and the ITS and TRD track extrapolations (Section 4.6.1). The dispersion σ_{D} of the residuals is representative of the accuracy of the distortion measurement. It is obtained by calculating the robust median absolute deviation (MAD) for each voxel, which is then scaled to the Gaussian standard deviation. The dispersion consists of the position resolution of TPC clusters and the track extrapolation uncertainties of the ITS and TRD tracks. At high interaction rates at which dynamic space-charge distortions become relevant, the space-charge distortion fluctuations also enter in this quantity. In order to eliminate their contribution, the dispersion is evaluated for runs at low interaction rate to

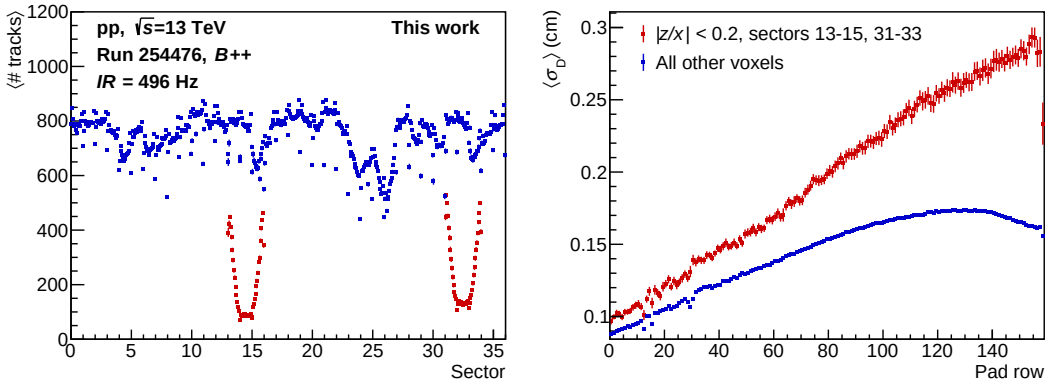

Figure 5.4: The average number of tracks per voxel collected for the extraction of the correction map as a function of the sector (*left*) and the average dispersion $\langle\sigma_{\mathrm{D}}\rangle$ as a function of the pad row (*right*). The red markers represent the voxels in the region with missing TRD modules. The blue markers represent all other voxels. The data are taken at 496 kHz interaction rate and with nominal positive $\boldsymbol{B}$-field.

estimate the precision of the distortion measurement.

The collected statistics in terms of number of tracks per voxel determine the statistical uncertainty of the distortion measurement. The average number of tracks per voxel are shown as a function of the TPC sector in the left plot of Fig. 5.4. The statistics in the chosen run match the typical requirements of a calibration interval. The red markers show the average number of tracks in the first $|z/x|$ bin and sectors 13–15 and 31–33 while the blue markers represent all other voxels. The significantly lower number of tracks in the selected regions (red markers) is a consequence of missing TRD modules at the position of the PHOS which covers $|z/x| < 0.12$ and the φ region of the selected sectors. Since the PHOS only covers part of the $|z/x|$ bin, some statistics can be collected in the region $0.12 < |z/x| < 0.2$. Furthermore, tracks with sufficiently low transverse momentum can enter sectors next to the PHOS, where the TRD is available, due to their curvature in the magnetic field, even if they cross higher pad rows. The average dispersion as a function of the pad row is shown in the right plot of Fig. 5.4. In the regions with missing TRD modules, the dispersion is systematically higher than in the other voxels. The difference as well as the spread of the dispersion represented by the error bars increase at higher pad rows as the transverse momentum needs to be lower for tracks crossing higher pad rows to be able to reach neighboring sectors with the TRD. The extrapolation uncertainty of tracks increases with decreasing transverse momentum, which is reflected in the dispersion. The dispersion in voxels with full TRD coverage is well below 2 mm. It increases with the radius until around pad row 120 and starts to decrease again at pad row 135. This dependence originates in the weights assigned to the extrapolations of ITS and TRD tracks. They are composed of the distance to the given pad row and the position resolution of the different detector layers.

The error of the extracted distortions in each voxel can be estimated by the dispersion divided by the square root of the number of tracks. The distribution as well as the mean are shown as a function of the number of tracks in the left plot of Fig. 5.5. The increase and broad distribution of the dispersion in regions without TRD, corresponding to lower amount of tracks, is also seen here. The average precision reaches 50 µm at close to 800 tracks and decreases further according to the $1/\sqrt{n}$ dependence. Another possibility to determine the accuracy of the measurement is to compare the correction maps of two different runs at similar interaction rate. This is done in the right plot of Fig. 5.5 which

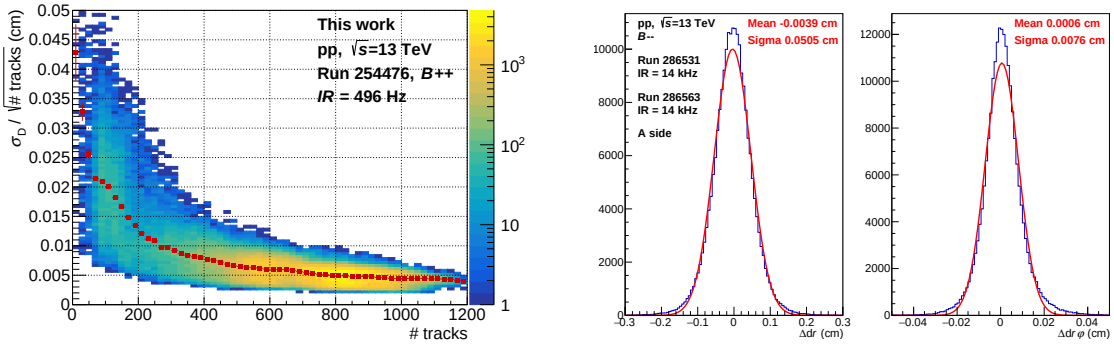

Figure 5.5: *Left:* The distribution of the dispersion σ_{D} divided by the square root of the number of tracks as a function of the number of tracks per voxel. The red markers represent the mean value and provide an estimate of the average precision of the distortion measurement. *Right:* The distributions of the differences $\Delta \mathrm{d}r$ and $\Delta \mathrm{d}r\varphi$ on the A side between two runs at low interaction rate which are taken close-by in time. Gaussian fits (red lines) are performed to obtain the mean and σ. The precision of $\mathrm{d}r$ and $\mathrm{d}r\varphi$ then correspond to $\sigma/\sqrt{2}$.

shows the distributions of the differences $\Delta \mathrm{d}r$ and $\Delta \mathrm{d}r\varphi$ between two runs which have been taken with pp collisions at 14 kHz and close-by in time. The distributions are fitted by a Gaussian to obtain the mean and σ. The resulting precision $\sigma/\sqrt{2}$ corresponds to 357 µm in $\mathrm{d}r$ and 54 µm in $\mathrm{d}r\varphi$.

5.2 Distortions with Ar-CO_2

Large distortions are observed with a gas mixture of Ar-CO_2 in data taken at high interaction rate. After subtraction of the corresponding reference map taken at low interaction rate (below 100 Hz for Pb−Pb collisions), the distortions in azimuthal direction $\mathrm{d}r\varphi$ close to the CE ($|z/x| < 0.2$) in Pb−Pb data taken at 7.5 kHz interaction rate are visualized in Fig. 5.6. While there are no residual distortions in most of the TPC volume, a number of spots with larger distortions appear in several regions. Two different kinds of structures are apparent. Distortions of up to 6 cm are measured in the OROC of sector 24 (OROC C06). The azimuthal distortions are centered around the middle of the chamber and a radius of 192 cm and they extend over the whole chamber and into neighboring sectors. On the other hand, there are several structures centered around the sector boundaries of IROCs and certain radii. The spatial extent of these structures differs, as does the number of structures appearing at different radii of the same sector boundary. The sector profile of the azimuthal distortions is shown in the bottom plot of Fig. 5.6. The colored markers represent the distortions at various radii of the IROCs, pointing out the different dependencies on the radius at different sectors. A distinct φ pattern emerges as the azimuthal distortions change their sign at the sector boundaries. Considering the opposing sign of the distortions and the corrections actually plotted, the electrons are distorted towards the boundaries between the IROCs. This means that part of the ionization electrons end up on top of the edges of the IROCs instead of in the amplification area, which results in an effective decrease of the azimuthal acceptance of the TPC. On the A side, the distortions at the sector positions 2, 4, 6 and 9 are of the order of 2–4 cm at this particular interaction rate in Pb−Pb collisions while smaller distortions are observed at sectors 7, 10 and 16. On the C side, the distortions amount to 4–6 cm at sectors 20 and 30, 1–2 cm at sectors 31 and 35 and smaller distortions appear

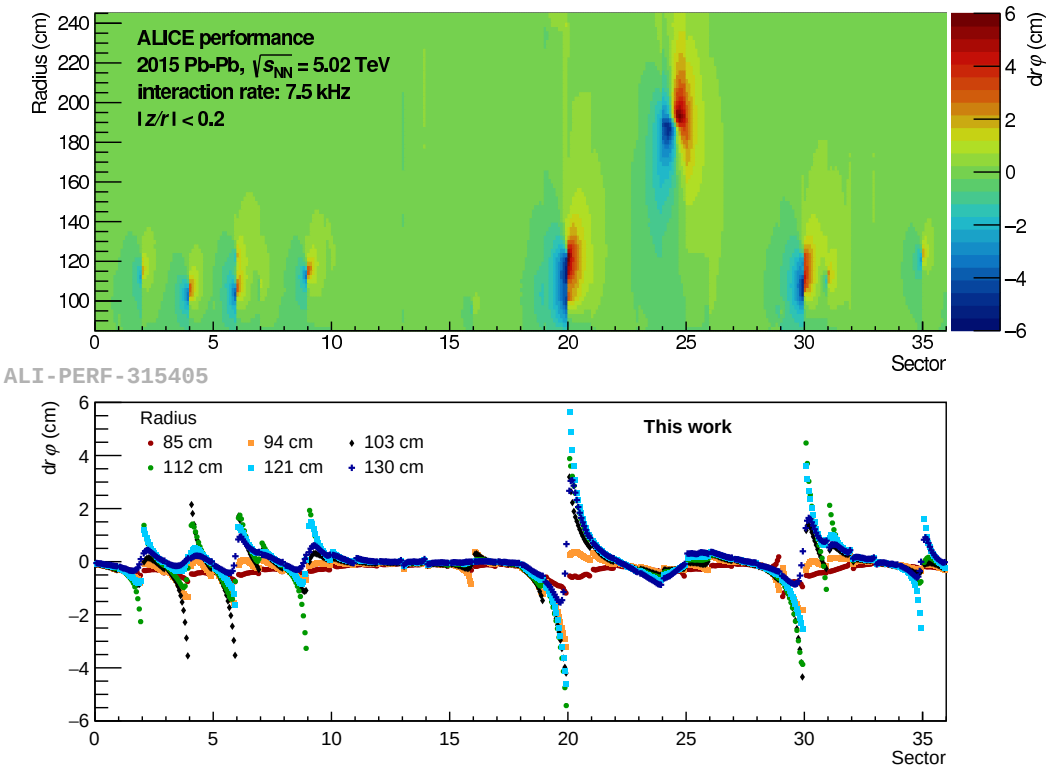

Figure 5.6: The space-charge distortions d$r\varphi$ (color scale) as a function of the radius and sector (*top*) and their sector profile at different radii of the IROCs (*bottom*) at $|z/x| < 0.2$, measured with nominal positive $\boldsymbol{B}$-field (B++) in Pb−Pb collisions at 7.5 kHz interaction rate in 2015.

at sectors 19 and 29. In this and the following sections, the distortions observed in the IROCs are further investigated while the distortions in OROC C06 are discussed in Section 5.7.

The radial dependence of the azimuthal distortions d$r\varphi$ close to the CE on both sides of the sector boundaries of the IROCs is plotted in Fig. 5.7. The distortions are very localized in radial direction as pronounced peaks are observed. A convolution of numerous peaks at different radii appears at many of the sectors. Especially sectors 20 and 30 show a rather high number of spots and stand out in terms of the spatial extent and the amplitude of the distortions. On the other hand, sector 9 shows two rather sharp peaks and there is only one peak at sector 35. The dependence of the distortions on the drift length on both sides of the sector boundaries is demonstrated in Fig. 5.8. The drift length is expressed by the local coordinate z/x with increasing $|z/x|$ corresponding to a decreasing drift distance. The radial position x is chosen differently for each sector, matching the radius close to the largest distortions observed at the corresponding sectors. As the acceptance of the TPC is limited to $|z/x| < 0.9$, the measurement covers only part of the full z-range at the radii of the IROCs. For example, at x =110 cm, the maximum z-position within the acceptance is 99 cm, covering about 40 % of the full drift and corresponding to a range between the full drift length of 250 cm and 151 cm of drift. The measured data are in good agreement with linear fits to the data points. Depending on the sector, the distortions decrease by 22–43 % across the full z/x acceptance while the drift distance decreases by 34–45 %. Since the distortions occur only at specific φ-positions and away from the inner field cage and rods, the monotonic linear behavior as a function of $|z/x|$ implies the presence of space charge with constant density along the full drift in the affected regions. Surface charge, e.g. at the surface of the ROCs, can be excluded as the resulting electric field would affect only a limited region close to the

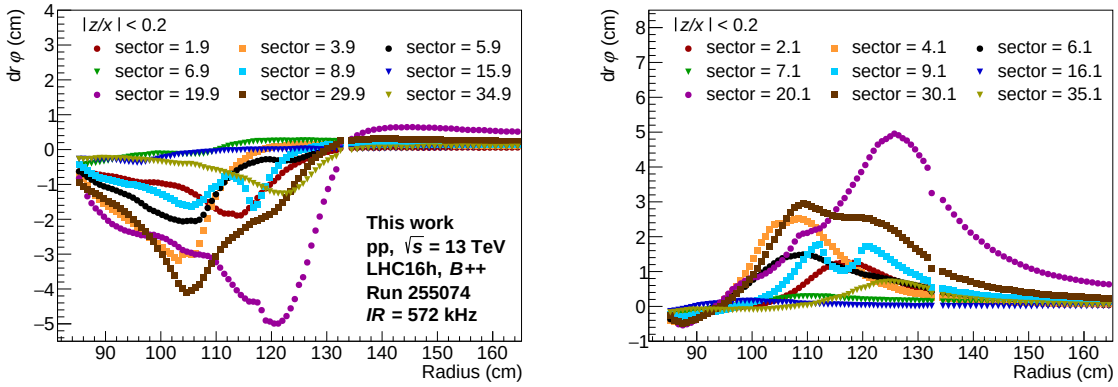

Figure 5.7: The azimuthal distortions $\mathrm{d}r\varphi$ as a function of the radius at $|z/x| < 0.2$ in pp collisions at an interaction rate of 572 kHz. They are shown for both sides (*left and right plot, respectively*) of the different sector boundaries (colored markers) affected by large distortions.

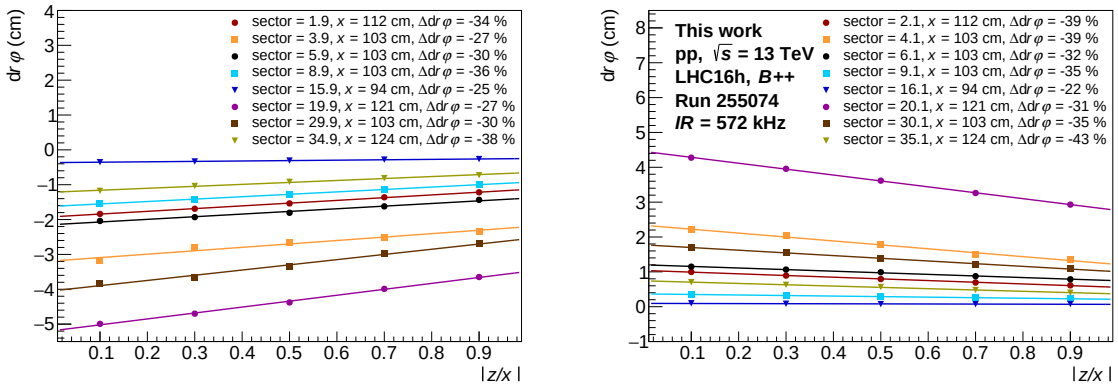

Figure 5.8: The azimuthal distortions $\mathrm{d}r\varphi$ as a function of $|z/x|$ in pp collisions at an interaction rate of 572 kHz. They are shown for both sides (*left and right plot, respectively*) of the different sector boundaries (colored markers) at the respective x-positions at which the largest distortions are observed. The solid lines represent first-order polynomial functions fitted to the data points. The relative change of the distortions across the full $|z/x|$ acceptance is quoted in the legend as $\Delta\mathrm{d}r\varphi$.

surface, therefore showing no particular dependence on the drift length. The distinct radial dependence suggests narrow columns of positive ions which are created locally in radius at the ROCs and drift through the full volume towards the CE, while the number of such columns of space charge is different at each sector. Consequently, the x-position of the distortion peaks is shifted between the two sides of the sector boundaries due to the $\boldsymbol{E}\times\boldsymbol{B}$ terms in Eq. (3.5).

5.2.1 Simulation of Space-Charge Distortions

The observed distortions are compared to results of simulations to confirm that their origin is indeed space charge and to determine the underlying space-charge distribution. Starting from a known space-charge density distribution, the distortions are calculated with AliRoot using numerical methods, first solving the Poisson equation (Eq. (4.8)) to obtain the electric field and then using the solution of the Langevin equation (Eq. (3.4)).

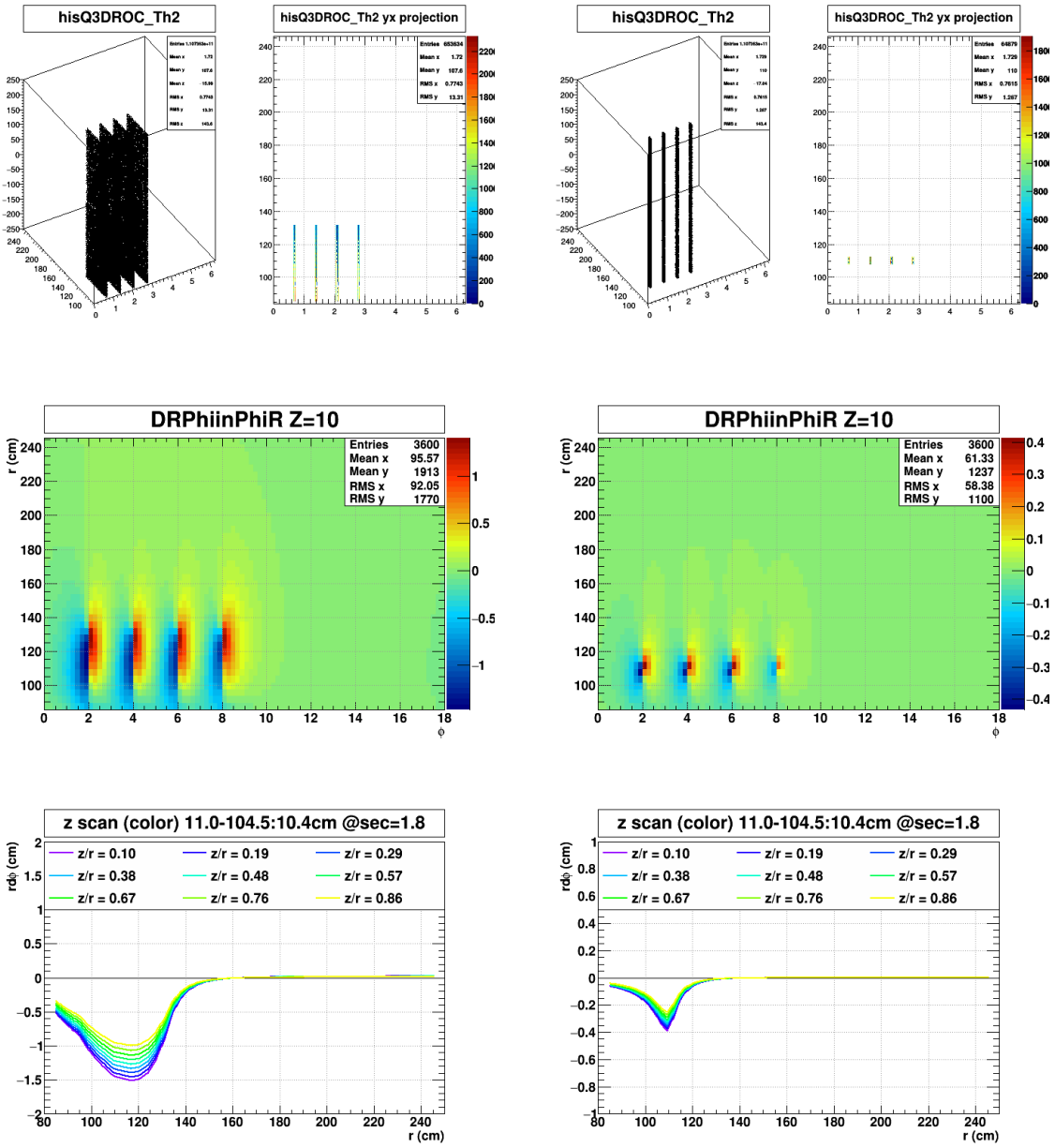

Figure 5.9: Two scenarios of space-charge distortions are simulated. Space charge is distributed along the full drift in four narrow regions in φ, once across the full radial coverage of the IROCs (*left column*) and once within a limited region in radius (*right column*). *Top:* The input space-charge density distribution as a function of z, r and φ (*3d plot*) and its r-φ projection. *Middle:* The azimuthal distortions d$r\varphi$ (color scale) close to the CE as a function of the radius r and φ. *Bottom:* The azimuthal distortions d$r\varphi$ at sector 1.8 as a function of the radius r. The different colors represent the distortions at different z/x [62, 67].

Two possible scenarios are considered and presented in the top panel of Fig. 5.9, assuming space charge at several narrow regions in φ for both. The space-charge density is chosen arbitrarily and constant along all z. In the first scenario, the space charge extends over the full radial coverage of the IROCs while in the second scenario, it has a radial extent of about 5 cm at the radial center of the IROCs.

The distortions calculated from the corresponding input distributions are also shown in

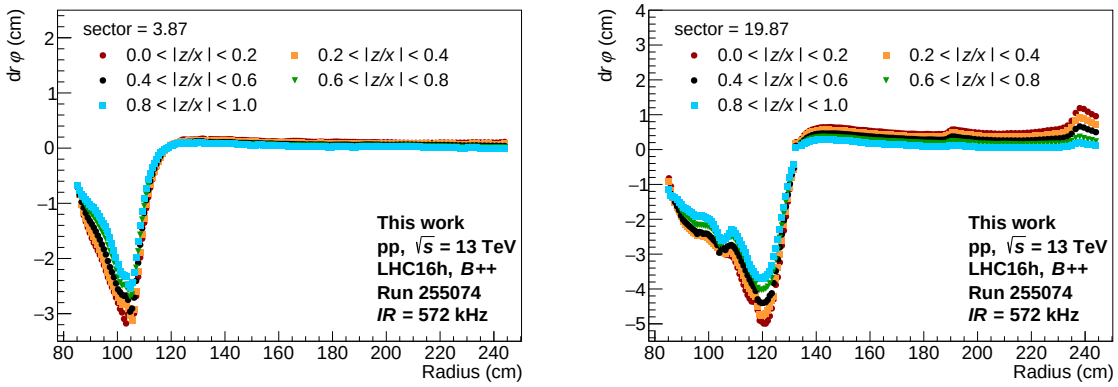

Figure 5.10: The azimuthal distortions $dr\varphi$ at sector 3.87 (*left*) and sector 19.87 (*right*) as a function of the radius in different z/x intervals represented by differently-colored markers. The data is measured with nominal positive $\boldsymbol{B}$-field in pp collisions at 572 kHz interaction rate.

Fig. 5.9. The middle panel illustrates the azimuthal distortions close to the CE as a function of the radius and φ. The different radial extents of the space-charge density distributions are reflected in the shape of the resulting distortion spots. The amplitude of the obtained distortions scales with the charge density and to some extent depends on the total area filled with space charge. A comparison to Fig. 5.6 favors the second scenario with a column of positive ions which is narrow in both r and φ. This becomes even more obvious when comparing the radial profile of the distortions at different z/x in the simulation in the bottom panel of Fig. 5.9 and the data in Fig. 5.10. The shape of the radial profile measured at sector 4 matches the one obtained by a column of space charge which is also confined in radial direction. At sector 20, which is one of the spots with the biggest distortions and largest spatial extent, the data suggests several narrow columns at different radii rather than a layer of space charge across the full radius of the IROC. The z/x dependence is similar in both simulation scenarios and it is in good agreement with the one observed in data, confirming that the distortions are caused by space charge along the full drift.

5.2.2 Dependence on the Interaction Rate and the Magnetic Field

The total amount of space charge inside the TPC volume scales with the ionization deposited by particles from collisions within one ion drift-time. This is the case for space charge from primary and secondary ionization distributed over the full TPC volume as well as for the space charge observed locally at some of the sector boundaries since the only way to create a large number of positive ions at the ROCs is amplification of ionization electrons. Therefore, the observed distortions are expected to show a characteristic dependence on the interaction rate which is a good measure for the average amount of ionization from primary collisions within the time interval relevant for the accumulation of space charge along the full drift. The interaction rate dependence is studied with data from Pb−Pb and pp collisions. In addition, the Pb−Pb data also offer the possibility to study the space-charge distortions with different $\boldsymbol{B}$-field polarities as there are ample data over the full range of interaction rates for both negative and positive magnetic field at nominal field strength. The 99th percentile of the sorted values of the absolute azimuthal distortions measured within ± 0.5 sectors around the respective sector boundary over the full radial coverage of the IROCs is used as a robust estimator for the size of the distortions in a given calibration interval.

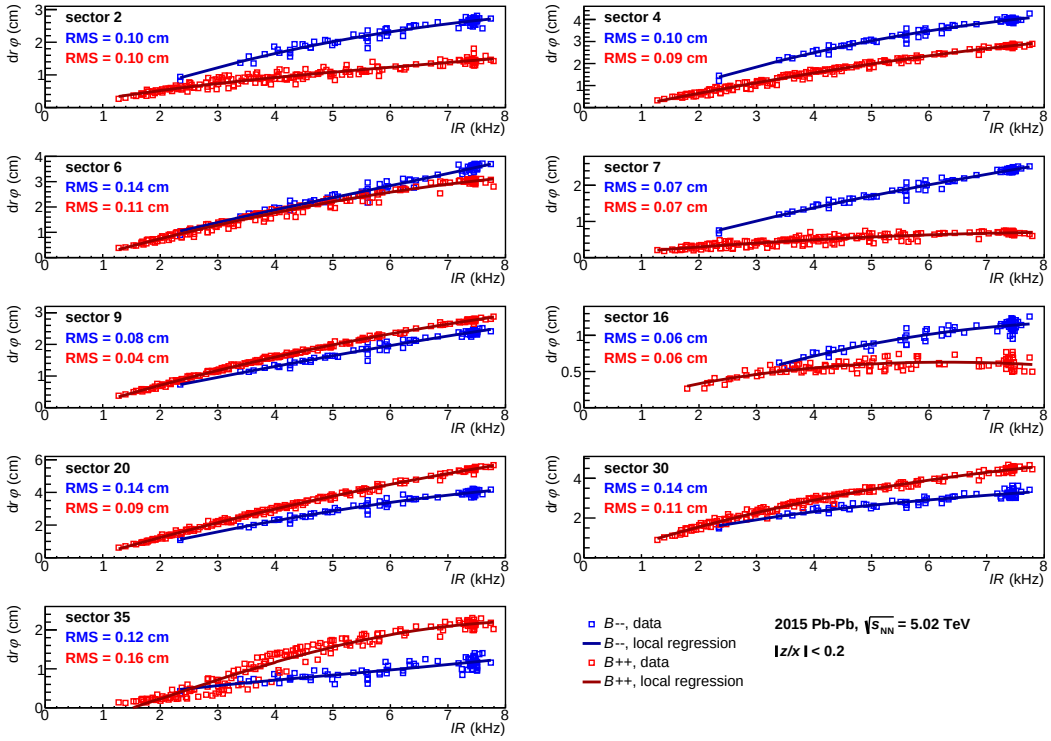

Figure 5.11: The azimuthal distortions d$r\varphi$ close to the CE at the different sector boundaries as a function of the interaction rate *IR* in Pb−Pb data taken in 2015. The blue open markers represent data taken with nominal negative magnetic field while the red open markers show the measurements with nominal positive field. The results of a local regression with a Gaussian kernel are drawn with dark blue and dark red lines for the negative and positive $\boldsymbol{B}$-field polarity, respectively. The RMS of the differences between the data points and the local regression is quoted in the figures [62, 68].

The local space-charge distortions close to the CE at interaction rates between 1 kHz and 8 kHz measured in Pb−Pb collisions with both positive and negative magnetic field in 2015 are shown in Fig. 5.11. The data are drawn with open markers. The average value at a given interaction rate, represented by the solid lines, is obtained by a local regression applying a Gaussian kernel of a width of 4 kHz. While the size of the distortions varies between the different sector boundaries, the dependence on the interaction rate is qualitatively the same. At the lowest interaction rates of about 1.2 kHz, the distortions are already prominent with a size of a few mm and they further increase with the interaction rate. The dependence differs from a strictly linear rise within the range of the measurement as the slope gets smaller at increasing interaction rates. At the highest interaction rates of the data period of close to 8 kHz, the distortions still increase at most of the sectors. However, at sectors with comparably small distortions, in particular sectors 7 (positive $\boldsymbol{B}$-field) and 16, they show signs of a saturation effect as the slope approaches zero. The RMS of the differences between the data and the local regression is of the order of 1 mm. It represents the fluctuations of the average distortions at the level of the calibration intervals but strongly underestimates the real fluctuations of the space-charge density which are relevant at much smaller time scales than the length of a calibration interval. Space-charge density fluctuations are further discussed in Section 5.2.3.

The change of the polarity of the magnetic field has a clear effect on the size of the distortions at each sector. As its nominal orientation is along the z-axis, it adds a

contribution to both the radial and azimuthal distortions via the $\boldsymbol{E}\times\boldsymbol{B}$-terms in Eq. (3.5). The dependence of the distortions on the interaction rate is generally the same with both $\boldsymbol{B}$-field polarities. Their size, however, is significantly affected in opposite ways at the sectors on the A and C side. While they are bigger with negative magnetic field on the A side, the same is the case with positive polarity on the C side. This particular fact indicates an asymmetry in the r-φ plane related to the origin of the space charge. Furthermore, the different behavior at sector 9 from all other sectors on the A side implies the significance of higher order effects. In the case of a narrow cloud of positive ions along the full drift, ionization electrons are focused towards the positive charge. Because of the $\boldsymbol{E}\times\boldsymbol{B}$-effect however, their drift path follows a helix and they are deflected away from the center of the ions. Consequently, their arrival point at the ROCs is shifted with respect to the center of the space charge distribution. As the absolute contribution of the $\boldsymbol{E}\times\boldsymbol{B}$-terms increases with the amount of space charge, the corresponding deflection from the origin of the charge also increases. Taking this into account, an exponential increase of the distortions is expected at relatively small interaction rates as ionization electrons from further and further away are focused into the region where the space charge is produced by gas amplification. With increasing space-charge density, the additional amount of ionization electrons pulled into the actual amplification region of the space charge drops as the deflection due to $\boldsymbol{E}\times\boldsymbol{B}$ gets bigger. As a consequence, the dependence on the interaction rate is expected to become linear. The change of the magnetic field polarity results in a change of the sign of the $\boldsymbol{E}\times\boldsymbol{B}$-terms which can modify the distribution of ionization electrons ending up within the amplification region of the space charge in case of asymmetries of the boundary conditions.

The average particle density $\mathrm{d}N_{\mathrm{ch}}/\mathrm{d}\eta$ of 6.5 at mid-rapidity in pp collisions [69] is smaller by a factor 77 compared to Pb−Pb collisions [70]. Therefore, interaction rates higher by the same factor are required to achieve a similar particle flux from primary collisions, resulting in a comparable amount of primary ionization and space-charge density. While the measurement of the interaction rate only takes into account primary collisions, the amount of particles from beam background, i.e. satellite collisions, contributing to the total number of particles in the TPC becomes significant at interaction rates of the order of several hundred kHz in pp collisions. As a consequence, large fluctuations of the space-charge density and of the measured distortions due to different beam conditions are observed for different calibration intervals at the same interaction rate. In order to take into account also the beam background and to provide a more precise estimate of the total particle flux inside the TPC, a second flux estimator is investigated for the analysis of the distortions. The currents measured at the anode wires of the TRD chambers are correlated to the particle flux at any given moment. Since there is no comparable mechanism like the GG in the TPC, ionization electrons created by particles from all collisions are detected in the TRD chambers, independently of the trigger signal. The anode currents of each TRD chamber are written to the OCDB with a granularity of 1 min or less if the values change by more than a pre-defined threshold and they are available on a run-by-run level. They are averaged over the full run chamber-by-chamber. The median of the average values of all chambers in the first layer of the TRD, normalized to the average relative gain of all chambers, provides a robust measure of the average anode currents in the first TRD layer and is used as an estimate for the total particle flux in the calibration intervals within the given run.

Fig. 5.12 shows the azimuthal distortions at the different sector boundaries close to the CE in pp collisions as a function of the two flux estimators, interaction rate and average anode currents in the first TRD layer. In total, almost 700 measurements taken at nominal operating conditions with positive magnetic field in 2015 and 2016 are analyzed.

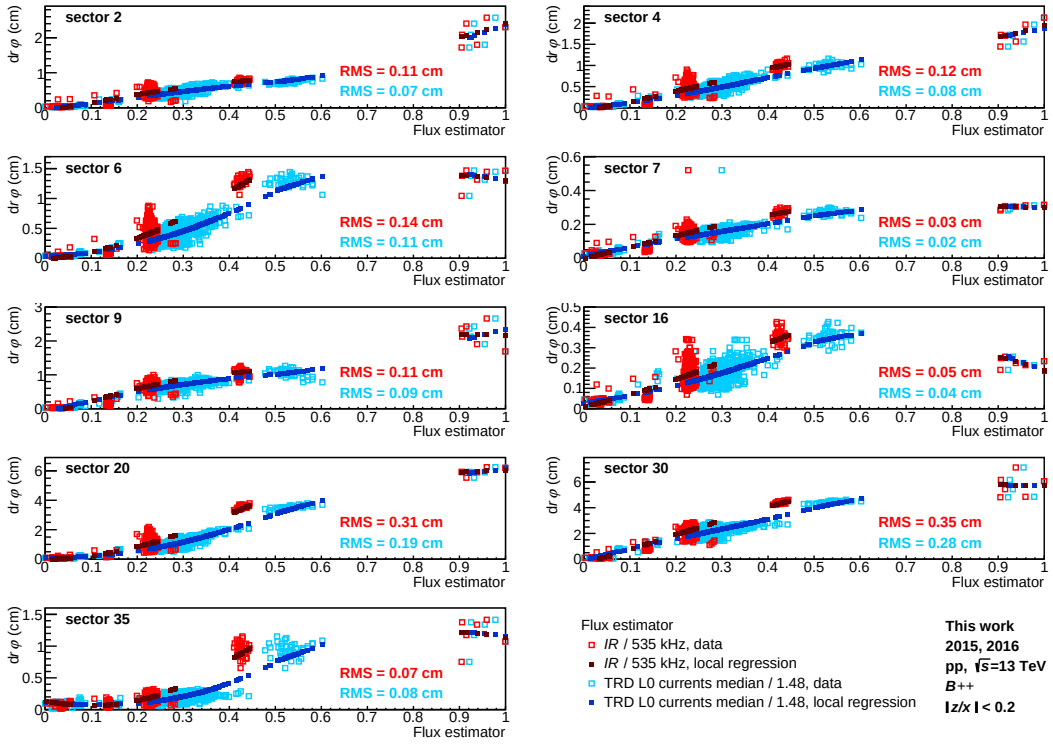

Figure 5.12: The azimuthal distortions d$r\varphi$ close to the CE at the different sector boundaries as a function of particle flux in the TPC expressed by two estimators, the interaction rate and a robust average of the TRD anode currents in its first layer. Each estimator is normalized to the respective maximum available in this data sample. The data were taken with nominal positive magnetic field in pp collisions in 2015 and 2016. The open markers show the data points while the full markers represent the results of a local regression with Gaussian kernel. The RMS values of the differences between data and local regression are quoted in the figures.

Both flux estimators are normalized to their maxima of 535 kHz and 1.48, respectively. A local regression with a Gaussian kernel width of 0.25 is performed to provide the average distortions as a smooth function of the flux. In contrast to the Pb−Pb data where the luminosity drops over time, leading to a wide continuous range of interaction rates available, the luminosity is leveled in pp collisions. Therefore, measurements are only available around certain interaction rates. More than 80 % of data points in this sample were taken at an interaction rate around 120 kHz, while 11 % are taken below 100 kHz and 6 % around 230 kHz. During a high luminosity test in 2016, few data were taken at about 500 kHz. Using the interaction rate as an estimate for the particle flux, a considerable spread of the distortions measured at the few different interaction rate points is observed. The RMS values of the differences between the data and the local regression are evaluated. They are dominated by the bulk of the points around 120 kHz and they are of the order of 15–20 % of the size of the distortions. The application of the TRD currents allows to better differentiate between different particle fluxes due to changing beam background at similar interaction rates. The data points cover a wider range of relative flux, providing a more precise parameterization of the flux dependence of the distortions. The spread of the measured distortions around the average values obtained by the local regression is also smaller as the RMS values improve by 20–40 % at almost all sectors. With the data available, the dependence of the distortions on the flux observed in pp collisions is qualitatively comparable to the interaction rate dependence in Pb−Pb collisions. In addition, the behavior at interaction rates well below 100 kHz in pp

collisions can be studied where the distortions increase exponentially. The slope decreases steadily with increasing flux. The limited number of points above 300 kHz prevents firm conclusions on the dependence towards very high interaction rates. It appears to also be similar to the observations in Pb−Pb data as the distortions further increase close to or slightly slower than linearly or slowly approach a saturation value. Regarding the size of the distortions at equivalent interaction rates in pp and Pb−Pb collisions, both measurements are in agreement except for sector boundaries 20 and 30 where the largest space-charge distortions are observed. At these two sectors, the distortions are bigger in pp collisions.

At high collision rates, the TRD anode currents proved to be a considerable alternative to the interaction rate as an estimator for the particle flux in the TPC. There are even possibilities for further improvements. In addition to the TRD anode currents in the OCDB which are used for this analysis, they are also available directly in the Detector Control System (DCS) where they are stored with a much higher granularity of 1 sec. A more precise average of the currents in one single calibration interval can be calculated using the DCS measurement instead of the OCDB values. Instead of using a robust average over full TRD layers, the same can be done for each sector combining the stack at $\eta = 0$ with the two outer stacks on each side, which allows to further differentiate the particle flux in φ-direction. The radial dependence can be extracted and extrapolated towards the volume of the TPC by the analysis of the currents in all six TRD layers and their parameterization as a function of the radius.

5.2.3 Fluctuations

The relative fluctuations of the space-charge density $\frac{\sigma_{\mathrm{SC}}}{\mu_{\mathrm{SC}}}$ can be calculated according to [18] as

$$\frac{\sigma_{\mathrm{SC}}}{\mu_{\mathrm{SC}}} = \frac{1}{\sqrt{N^{\mathrm{ion}}_{\mathrm{pileup}}}} \sqrt{1 + \left(\frac{\sigma_{N_{\mathrm{mult}}}}{\mu_{N_{\mathrm{mult}}}}\right)^2 + \frac{1}{F\mu_{N_{\mathrm{mult}}}} \left(1 + \left(\frac{\sigma_{Q_{\mathrm{track}}}}{\mu_{Q_{\mathrm{track}}}}\right)^2\right)}, \tag{5.1}$$

where μ_{SC} is the average space-charge density. The number of events $N^{\mathrm{ion}}_{\mathrm{pileup}}$ contributing to the pile up of ions in the TPC drift volume is described by a Poissonian distribution. It depends on the interaction rate and the drift time of the ions for the full drift length which is of the order of 350 ms for the Ar-CO_2 gas mixture. The relative fluctuations of the number of pile up events are given by $\frac{1}{\sqrt{N^{\mathrm{ion}}_{\mathrm{pileup}}}}$. The relative RMS of the track multiplicity distribution is given by $\frac{\sigma_{N_{\mathrm{mult}}}}{\mu_{N_{\mathrm{mult}}}}$ and $\frac{\sigma_{Q_{\mathrm{track}}}}{\mu_{Q_{\mathrm{track}}}}$ is the relative variation of the ionization of a single track. The geometrical factor F describes the range over which the space-charge density fluctuations are relevant for the distortions.

For the large local distortions observed in Run 2, F can be estimated by calculating the ratio of the spatial extent of the space charge and the area of the TPC in the r-φ plane. As the space charge is localized within a very narrow region, this ratio is significantly smaller than 1, in which case, the term containing the geometrical factor dominates Eq. (5.1). The relative space-charge density fluctuations then scale with $\sqrt{\frac{1}{r_F^2 \mu_{N_{\mathrm{mult}}}}}$, where r_F is the radius of a circle covered by the cloud of ions in the r-φ plane.

The space-charge density fluctuations are estimated for Pb−Pb as well as for pp collisions, using average charged-particle multiplicities of $\mu_{N_{\mathrm{mult}}} = 500$ and $\mu_{N_{\mathrm{mult}}} = 6.5$, respectively. The geometrical factor F is calculated assuming different spreads of the ion cloud, covering a range between 1 cm and 6 cm. The resulting space-charge density fluctuations are shown as a function of the interaction rate and r_F in Fig. 5.13. They decrease with increasing interaction rate which is proportional to the number of ion

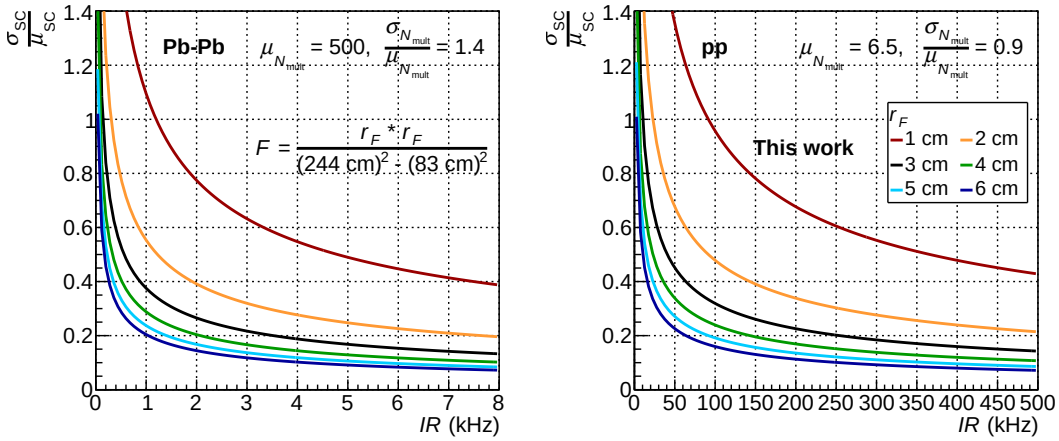

Figure 5.13: The relative fluctuations of the space-charge density $\frac{\sigma_{SC}}{\mu_{SC}}$ expected in Pb−Pb (*left*) and pp (*right*) collisions as a function of the interaction rate *IR* according to Eq. (5.1). The variation of the ionization along single tracks is assumed to be $\frac{\sigma_{Q_{track}}}{\mu_{Q_{track}}} = 1.7$ [18]. The case of only local space-charge distortions is defined by the choice of the geometrical factor F. The transverse spread r_F of the cloud of space charge is varied, indicated by the different colors.

pile-up events. Although the interaction rates in pp collisions are higher by about two orders of magnitude, the relative fluctuations are of the same order as in Pb−Pb collisions as the geometrical factor is the driving force in the case of the localized narrow columns of space charge. Furthermore, the variation of r_F demonstrates the significant impact of the size of the distortion spot on the space-charge density fluctuations as they scale with $\frac{1}{r_F}$. For the relevant region between 1 kHz and 8 kHz in Pb−Pb data, the fluctuations are expected to be between 60 % and 15 %, depending on the size of the distortions. At the common interaction rates in pp collision at ALICE in LHC Run 2, which are 100 kHz and 200 kHz, the relative space-charge density fluctuations are estimated to be around 15–50 % and 10–40 %, respectively.

The time scales relevant for the space-charge density fluctuations are determined by the different contributions in Eq. (5.1). They are of the order of the ion drift time or smaller, which is much shorter than the length of the calibration intervals used to extract the correction maps from the data. Therefore, the measured distortions provide only an average value as they are obtained from the mean of the residuals between the distorted TPC clusters and the reference track positions from the ITS-TRD-TOF track interpolation within a given calibration interval (Section 4.6.1). The fluctuations $\sigma_{\mathrm{d}r\varphi}$ of the distortions within one calibration interval can be estimated from the dispersion σ_{D} of the measured residuals. The dispersion can be written as $\sigma_{\mathrm{D}}^2 = \sigma_{\mathrm{d}r\varphi}^2 + \sigma_0^2$, where σ_0 accounts for all other contributions to the uncertainty of the measurement, i.e. intrinsic space-point resolution, diffusion and track interpolation uncertainties. Correction maps of low interaction rate data without space-charge distortions can provide an estimate for σ_0. It is subtracted from the dispersion of high-interaction rate data to leave only the contribution from the space-charge distortions.

Fig. 5.14 shows the dispersion σ_{D} as a function of the sector close to the CE in Pb−Pb data taken with nominal positive magnetic field. Data at an interaction rate of 7 kHz are shown with colored markers, where the color represents the pad row. The black markers show the dispersion averaged over all pad rows in the IROC at low interaction rate, which is around 0.15 cm and approximately constant in φ. At high interaction rate, the dispersion at the sector boundaries affected by the space-charge distortions is

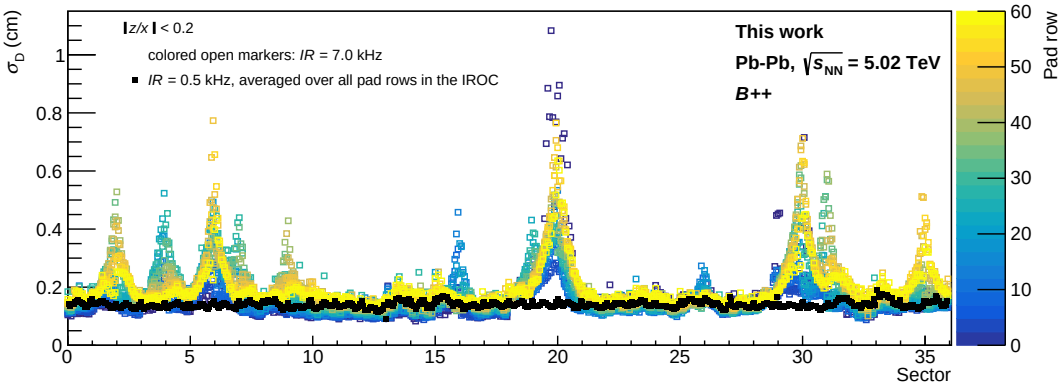

Figure 5.14: The dispersion σ_{D} of the measured residuals in azimuthal direction as a function of the sector close to the CE. The data have been taken during Pb−Pb collisions with nominal positive magnetic field. The open colored markers represent data at 7 kHz interaction rate, where the color indicates the pad row. The full black markers show the dispersion averaged over all pad rows in the IROC at low interaction rate.

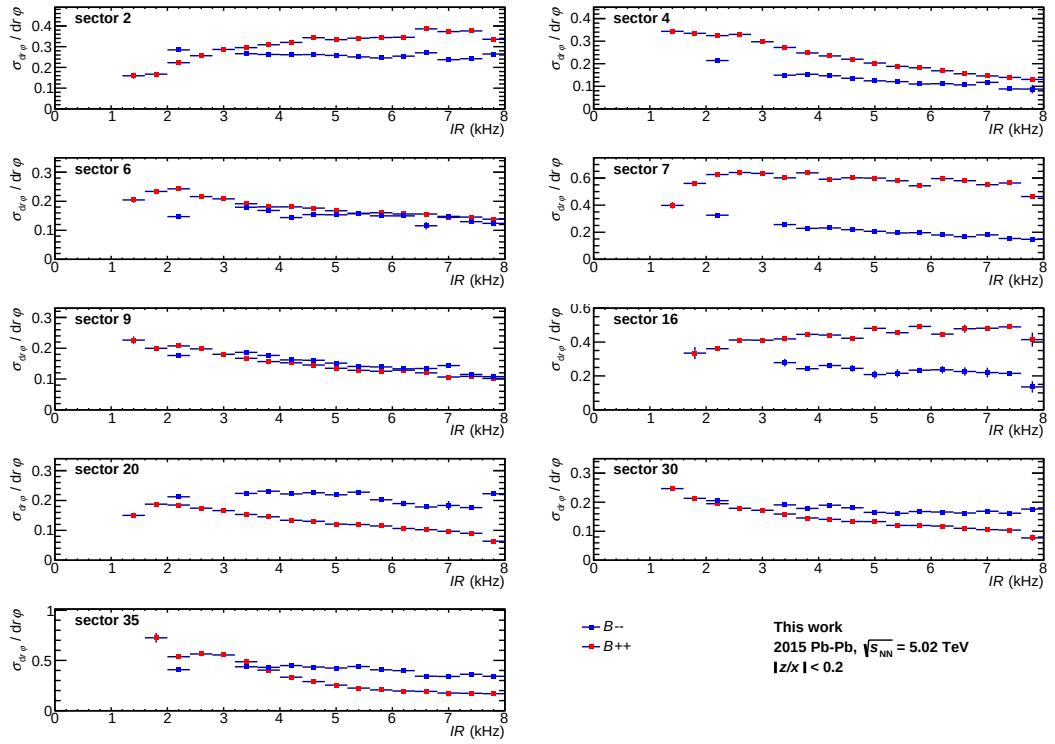

Figure 5.15: The relative fluctuations $\sigma_{\mathrm{d}r\varphi}/\mathrm{d}r\varphi$ of the azimuthal distortions close to the CE, derived from the dispersion σ_{D} as described in the text. They are shown as a function of the interaction rate and the $\boldsymbol{B}$-field polarity for the sectors with the biggest space-charge distortions. The fluctuations $\sigma_{\mathrm{d}r\varphi}$ are calculated as the average of the values around the pad row with the biggest distortions ±2 pad rows in the given interaction rate bin. The vertical error bars represent the standard deviation of this distribution.

significantly higher due to large fluctuations of the space-charge density. It is comparable to the low interaction rate data in the other regions. The fluctuations of the distortions $\sigma_{\mathrm{d}r\varphi}$ relative to the measured distortions $\mathrm{d}r\varphi$ (Fig. 5.11) as a function of the interaction rate in Pb−Pb collisions are presented in Fig. 5.15 for the different sector boundaries. Data with both magnetic field polarities are shown. Only the region close to the CE is

selected. The distortion fluctuations are taken as the average of the fluctuations around the pad row of the largest distortion ±2 pad rows at the given sector boundary. The data qualitatively agrees with the results derived form Eq. (5.1) in Fig. 5.13. Comparing the different $\boldsymbol{B}$-field polarities for a given sector, the relative distortion fluctuations are smaller for the setting with larger distortions. As the size of the local distortions increases, the space-charge density fluctuations are affected by fluctuations over a larger area, corresponding to r_F in Fig. 5.13, and, therefore, the relative space-charge density fluctuations get smaller. At most of the sectors with sizable distortions, the relative distortion fluctuations decrease with increasing interaction rate. At the highest interaction rate, the relative fluctuations at the sectors with the biggest distortions are between 10 % and 20 %, while for smaller distortions they reach up to 60 %. At low interaction rates, the distortion fluctuations tend to decrease as the measured distortions start to disappear. The dependence on the interaction rate at a given sector results from the combination of the number of ion pile-up events and the size of the distortion spot, both affecting the relative fluctuations. The number of ion pile-up events is the product of the interaction rate and the ion drift time. The latter follows pressure and temperature variations which are calibrated on time scales of the order of 1 h. The effect of ion drift time variations on the distortion fluctuations is disregarded here since the size of the distortion spots is the dominant factor in case of very local space-charge distortions.

The calibration procedure for the space-charge distortions described in Section 4.6.1 is the optimum solution with the information available in Run 2 data taking. However, the large fluctuations within a calibration interval can still affect the momentum and energy-loss measurement of single tracks, as they are treated by an additional uncertainty term in the covariance matrix of the track fit instead of being fully corrected. One way to minimize the effect of the fluctuations on the quality of the data is to perform a time-dependent calibration. Time intervals with large fluctuations can be identified by the analysis of tracking variables, e.g. the ITS-TPC track-matching efficiency as a function of φ, p_{T} and η. A strong deterioration of the track-matching efficiency at a given sector implies a large fluctuation. Time intervals identified like this can be excluded from the calibration and the data, improving both the calibration and the quality of the data available for physics analyses.

5.3 Distortions with Ne-Based Gas Mixtures

The characteristic gas properties of the Ne-based gas mixtures used in the TPC in Runs 1 and 2, in particular the amount of ionization and the ion mobility, are expected to lead to a space-charge density that is smaller by a factor of about 3.4 compared to the Ar-based gas mixture used in Run 2. This factor is composed of two times less ionization [60] and an ion mobility that is higher by a factor of 1.72 [51] in the Ne-based mixtures. For space charge created by gas amplification at the readout chambers, the amplification factor and the ion backflow also contribute to the amount of space charge. The nominal gain of the ROCs operated with Ne-CO_2-N_2 in 2017 is 1.6 times higher than with Ar-CO_2 in the remainder of Run 2.

In most of Run 1, the gas mixture was Ne-CO_2 (90-10). In 2013, p−Pb data at $\sqrt{s_{\mathrm{NN}}}$ = 5.02 TeV were taken with both magnetic field polarities at interaction rates between 4 kHz and 200 kHz. These high interaction rate data are the most promising to detect space-charge distortions in Run 1 data as the combination of average particle multiplicity and interaction rate gives the highest particle flux achieved during Run 1. Since the procedure to precisely correct large space-point distortions (Section 4.6.1) was developed and used in the calibration for Run 2, a special reconstruction pass including the new correction method was applied on a total of 16 runs selected from that p−Pb

Avg. interaction rate (kHz)	$\boldsymbol{B}$-field polarity	Period	Run	Duration (min)
3.9	negative	LHC13b	195351	42
9.4	negative	LHC13c	195592	17
9.7	negative	LHC13c	195596	21
9.8	negative	LHC13b	195480	27
9.8	negative	LHC13d	195681	74
82	negative	LHC13d	195726	23
124	negative	LHC13d	195724	66
163	negative	LHC13d	195721	21
72	positive	LHC13f	197153	84
91	positive	LHC13e	196214	55
92	positive	LHC13f	196974	24
128	positive	LHC13e	196199	42
139	positive	LHC13f	196972	152
185	positive	LHC13e	196185	35
199	positive	LHC13f	196965	21
200	positive	LHC13f	197296	43

Table 5.1: The average interaction rate, $\boldsymbol{B}$-field polarity, LHC period, run number and run duration of the runs from the 2013 p−Pb data taking period which are analyzed for the presence of local space-charge distortions.

period. This provides the possibility to verify the presence of the space-charge distortions in Run 1 and to study them as a function of the interaction rate and $\boldsymbol{B}$-field polarity with a Ne-based gas mixture.

Furthermore, in Run 2, the gas mixture was changed to Ne-CO_2-N_2 (90-10-5) to decrease the space-charge distortions for the pp data taking at $\sqrt{s} = 13$ TeV in 2017. The measured distortions can be directly compared to those in pp data taken with Ar-CO_2. In addition, more studies of the interaction rate dependence are performed and the measured distortions are compared to those in Run 1.

5.3.1 Run 1 p−Pb Data with Ne-CO_2

Table 5.1 shows the list of runs, their interaction rate and the polarity of the nominal $\boldsymbol{B}$-field from the 2013 p−Pb data taking period which are analyzed for local space-charge distortions. The correction maps of the runs at the lowest interaction rates, i.e. run 195351 at 3.9 kHz and run 197153 at 72 kHz for negative and positive magnetic field polarity, respectively, are used as reference maps to subtract static effects, leaving only distortions due to space charge. It is carefully checked that these reference maps are free from noticeable local space-charge distortions observed at the specific sector boundaries in Run 2 data with Ar. A calibration interval of 40 min was chosen for the reconstruction of these data. Those runs with a duration significantly longer than the calibration interval are split into multiple calibration intervals, resulting in more correction maps and data points than the actual number of runs.

The space-charge distortions observed in p−Pb collisions at interaction rates of 163 kHz for negative and 200 kHz for positive $\boldsymbol{B}$-field polarity are shown as a function of the radius and the sector in Fig. 5.16. The TPC region of intermediate track dip angles is selected ($0.4 < |z/x| < 0.6$) since distortions due to charge-up effects are dominant at long drift and small radii on the C side. For both magnetic field polarities, the local patterns observed at the sectors 2, 4, 6, 7, 9, 16, 20, 29, 30, 31 and 35 are the same as in pp data with Ar-CO_2. The ionization electrons are focused towards the boundary

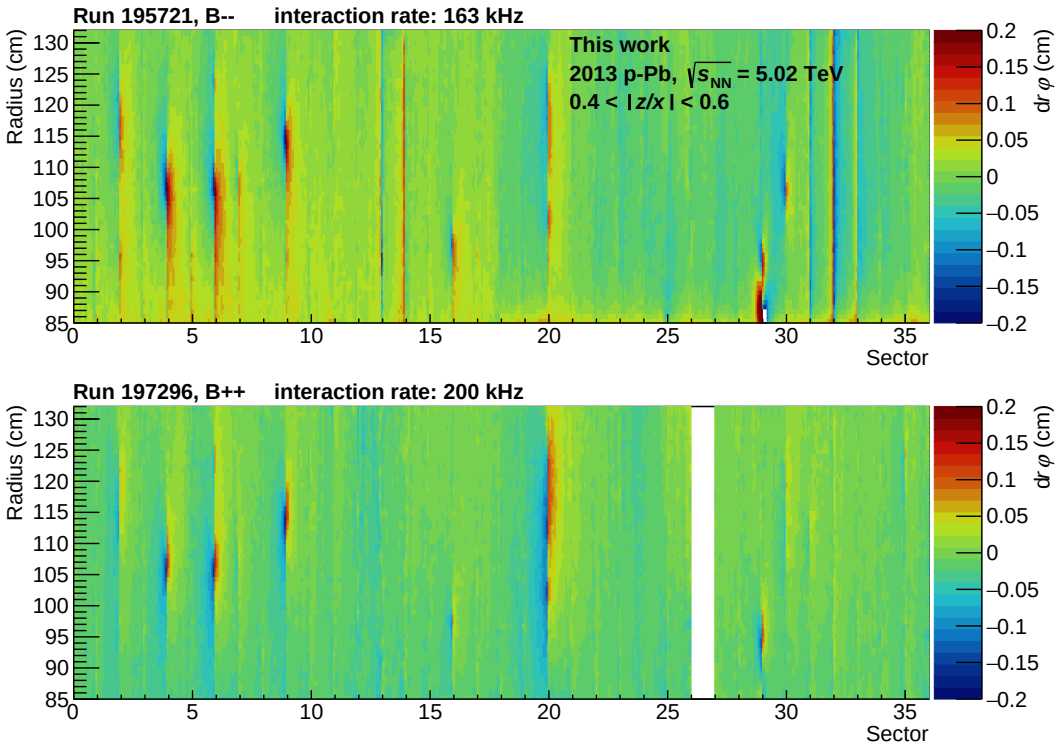

Figure 5.16: The distortions d$r\varphi$ (color scale), after subtraction of reference maps at low interaction rate without space-charge effects, as a function of the radius and sector. They are measured in high interaction rate p−Pb data with nominal negative (*top*) and positive (*bottom*) magnetic field. The region of $0.4 < |z/x| < 0.6$ is selected to avoid regions where charge-up effects are the dominant ones. In run 197296, no measurement is available in sector 26 as it was excluded from data taking.

between the two ROCs at the given sector position. Further analysis, in the same way as in Section 5.2, also shows a linear dependence of the local distortions on the drift length, concluding that the space charge was already present in Run 1. The exact shape and position along r of the distortion spots depend on the polarity of the magnetic field. Their maxima are in the order of 1–2 mm, which is the same order of magnitude as the intrinsic cluster resolution of the TPC. Therefore, the effect of the space-charge distortions on the reconstructed tracks is minimal in Run 1 data.

The interaction rate dependence of the space-charge distortions at $0.4 < |z/x| < 0.6$ in the 2013 p−Pb data is shown for runs with both nominal negative and nominal positive magnetic field in Fig. 5.17. A robust estimate of the size of the distortions is calculated by using the 99.9th percentile of the sorted array of absolute distortions measured in the IROCs at the given sector boundary ±0.5 sectors. At lowest interaction rates around 10 kHz, the values are in agreement with zero taking the uncertainty of the measurement into account. For negative $\boldsymbol{B}$-field, space-charge distortions of about 500 µm on the C side and well above 500 µm on the A side are present at 82 kHz and they rise with increasing interaction rate. The comparison between the two polarities of the $\boldsymbol{B}$-field on the A side is qualitatively consistent with the observations in Pb−Pb data taken with Ar-CO_2 in 2015 (Fig. 5.11). The distortions with positive magnetic field start to rise at higher interaction rates compared to those with negative $\boldsymbol{B}$-field and, therefore, are smaller at a given interaction rate. At sector 20 on the C side, the magnitude of the distortions with negative and positive magnetic field is comparable while at sector 30 with positive $\boldsymbol{B}$-field, the distortions appear to be constant around 500 µm for the entire

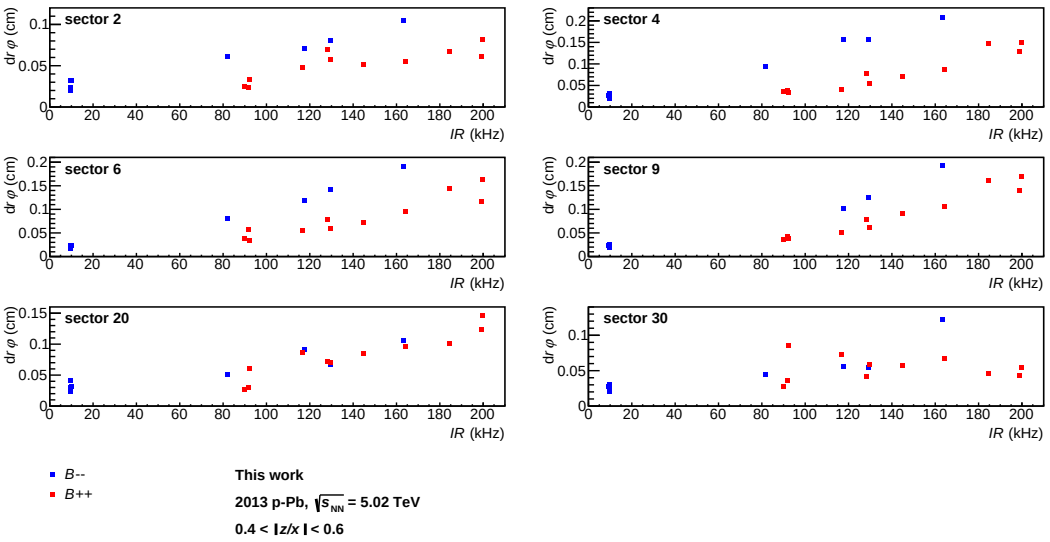

Figure 5.17: The azimuthal distortions d$r\varphi$ at the different sector boundaries as a function of the interaction rate *IR* in p−Pb collisions taken in 2013. The data is shown for the TPC acceptance within $0.4 < |z/x| < 0.6$. The blue and red markers represent data with nominal negative and positive magnetic field, respectively.

range of interaction rate points. The difference in the size of the distortions between A and C side with the respective magnetic fields in p−Pb data with Ne-CO_2 deviates from the observations with Ar-CO_2 (Fig. 5.11). This can be attributed to the characteristic properties of the gas amplification mechanism by which the space charge is created at the respective sectors. The limited number of points and range of interaction rates prohibits a conclusive deduction of the functional dependence of the space-charge distortions on the interaction rate. At and close to their onset, an exponential increase is expected but the available data points would also agree with a fit by a first order polynomial.

5.3.2 Run 2 pp Data with Ne-CO_2-N_2

For the year 2017, when only pp data were taken, the gas mixture was changed from Ar-CO_2 (88-12) to Ne-CO_2-N_2 (90-10-5). The motivation to switch back to a Ne-based gas was the restoration of the situation in Run 1 in terms of space-charge distortions and, therefore, to confirm that the condition of the TPC and its components stayed unchanged during the long shutdown between Runs 1 and 2. Further dedicated studies with the Ne mixture also allow to gain a better understanding of the observed space-charge effects and their origin.

The distortions measured in one run with nominal negative $\boldsymbol{B}$-field in pp data taken at an interaction rate of 462 kHz in 2017 are plotted as a function of the radius and the sector in Fig. 5.18. They are shown for tracks at intermediate dip angles of $0.4 < |z/x| < 0.6$. Similar observations are made as in the p−Pb data from Run 1. At sectors 2, 4, 6, 7, 9, 16, 20, 29 and 30, the same characteristic local patterns as in the Run 2 data with Ar-CO_2 are present. Their radial positions match those in the high interaction rate p−Pb data with Ne-CO_2. The biggest space-charge distortions appear at sectors 4, 6 and 9 and they are of the order of a few mm, which is comparable to the magnitude of the distortions measured in Run 1. A direct comparison to the distortions in p−Pb data with Ne-CO_2 at an interaction rate of 163 kHz is made in Fig. 5.19. Taking into account the different average charged-particle multiplicities in pp and p−Pb collisions of 6.5 [69] and 17.35 [71], respectively, the interaction rate of the p−Pb run

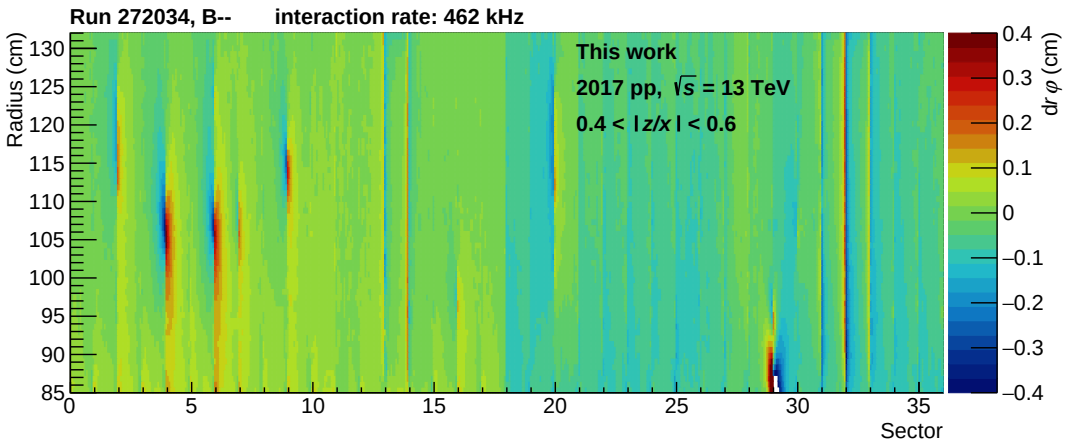

Figure 5.18: The measured distortions $\mathrm{d}r\varphi$ (color scale) as a function of the radius and sector in a run taken with nominal negative magnetic field during pp collisions at 462 kHz interaction rate in 2017. The data are shown for $0.4 < |z/x| < 0.6$.

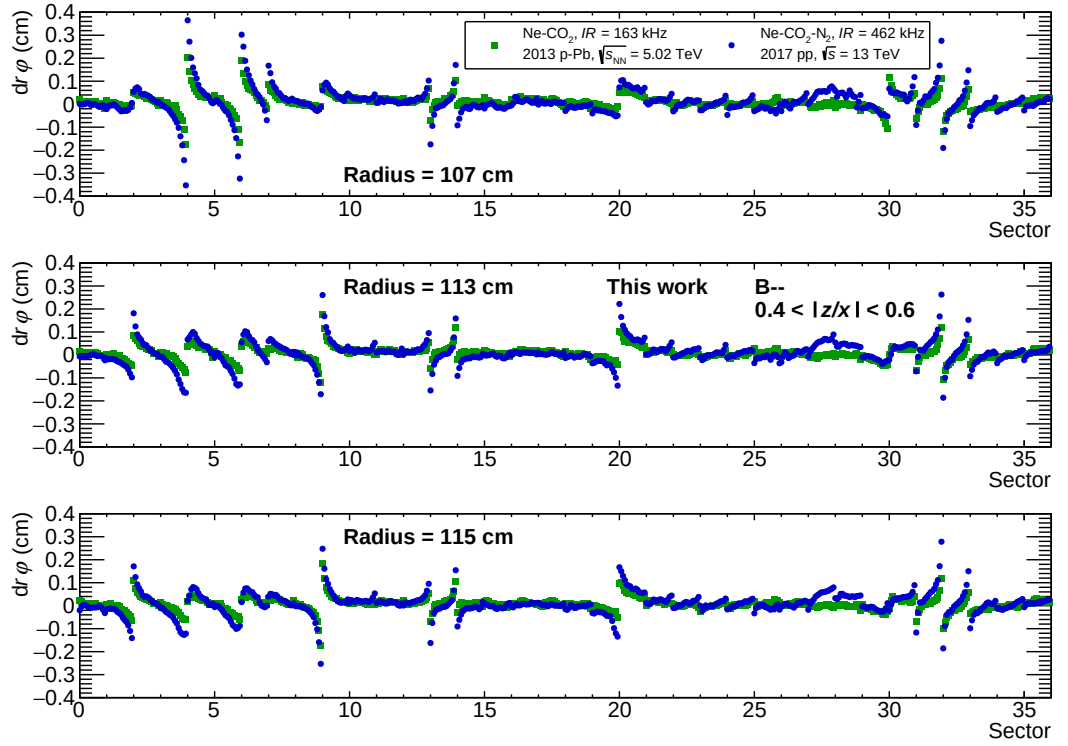

Figure 5.19: The measured distortions $\mathrm{d}r\varphi$ as a function of the sector at three different radii (*top*, *middle* and *bottom*) for tracks at $0.4 < |z/x| < 0.6$. The green markers show p−Pb data from 2013 with Ne-CO_2 (90-10) at an interaction rate of 163 kHz. The blue markers represent pp data taken in 2017 with Ne-CO_2-N_2 (90-10-5) at 462 kHz. The magnetic field has negative polarity and nominal strength in both runs.

corresponds to an pp-equivalent interaction rate of 435 kHz which is almost 6 % lower than in the pp run. The plots show the distortions measured at three different radii as a function of the sector at $0.4 < |z/x| < 0.6$. In general, the space-charge distortion patterns observed in the two runs are well in agreement. The distortions on the A side are larger by a factor of 1.5 to 2 in the pp run. On the C side, there are constant offsets between the high interaction rate runs and the low interaction rate references. They amount to 0.65 mm and 0.2 mm in the pp and p−Pb run, respectively, and are corrected

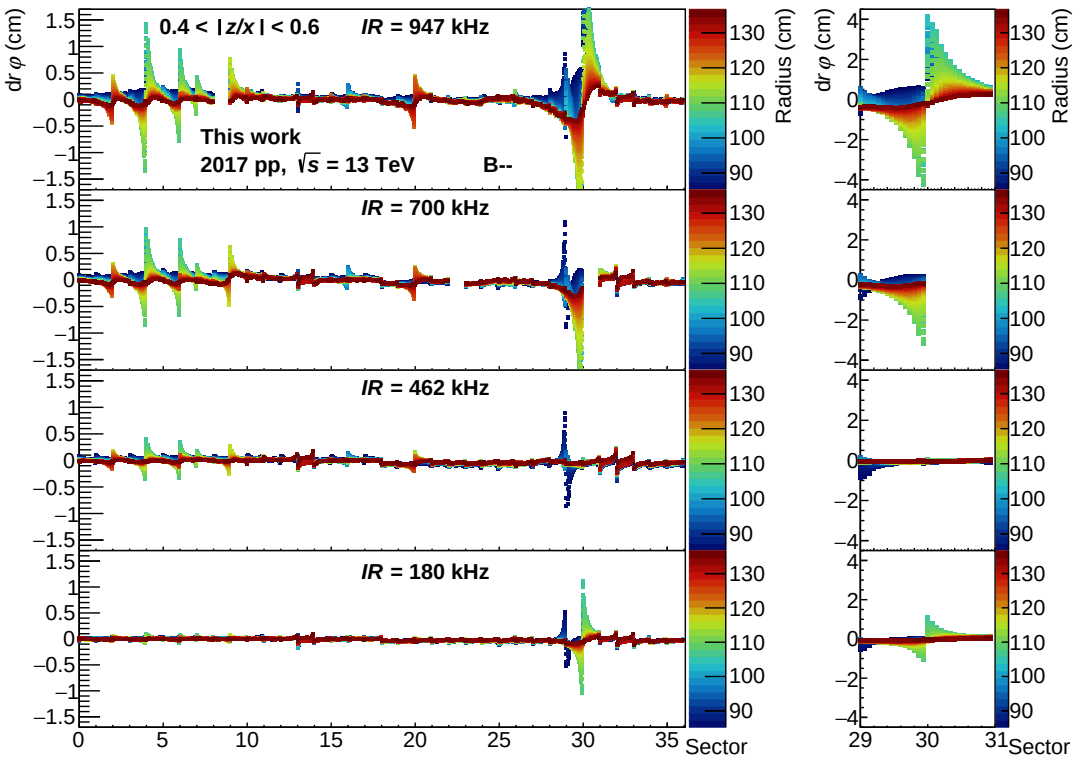

Figure 5.20: The measured distortions $dr\varphi$ with Ne-CO_2-N_2 as a function of the sector (*left*) and at sector 30 (*right*). The color scale represents the radius. The data show the measurements at different interaction rates with nominal negative $\boldsymbol{B}$-field and at $0.4 < |z/x| < 0.6$. Missing data points for a single sector indicate that the particular ROC was switched off during the given run.

for in Fig. 5.19. Similar as on the A side, the space-charge distortions at sector 20 are bigger by a factor of two in the pp run while at sector 30, the opposite appears to be the case and they are smaller by a factor of two in this particular comparison. Apart from the local space-charge distortions, sector dependent effects due to charge-up are observed at sectors 12, 13, 14, 31, 32 and 33, where they are of the order of several mm, and to a smaller extent at every sector on the C side. Comparing the size of the distortions due to the charge-up effects in pp and p−Pb, they are bigger by a factor of two in the pp data, which matches the differences in the local space-charge distortions. Since both charge-up and space-charge effects depend primarily on the particle flux inside the TPC, the observed differences can be reduced to the different running conditions in the two runs, i.e. collision system and energy, interaction rate and beam background, and the exact gas mixture. Therefore, one can conclude that the space-charge distortions in Run 1 and Run 2 with Ne-based gas mixtures are compatible and that, in Run 2, the TPC was in the same condition as it was in Run 1.

The results of a dedicated scan to study the interaction rate dependence of the distortions with Ne-CO_2-N_2 are presented in Fig. 5.20. Four consecutive runs have been exercised, increasing the interaction rate from 180 kHz to 947 kHz and then decreasing it to 700 kHz and 462 kHz. The local space-charge distortions monotonously increase with the interaction rate at almost all sector boundaries, e.g. to up to 1.5 cm at sector 4. Only at sector 30, a highly irregular appearance of the space-charge distortions is observed in two particular data taking periods in 2017. At the beginning of the scan, they are uncharacteristically large compared to the other sectors and to previous observations with Ne-based gas mixtures, reaching values only observed in Ar data so far. In the last run of the scan, they are back at a level which one would expect from the measurement

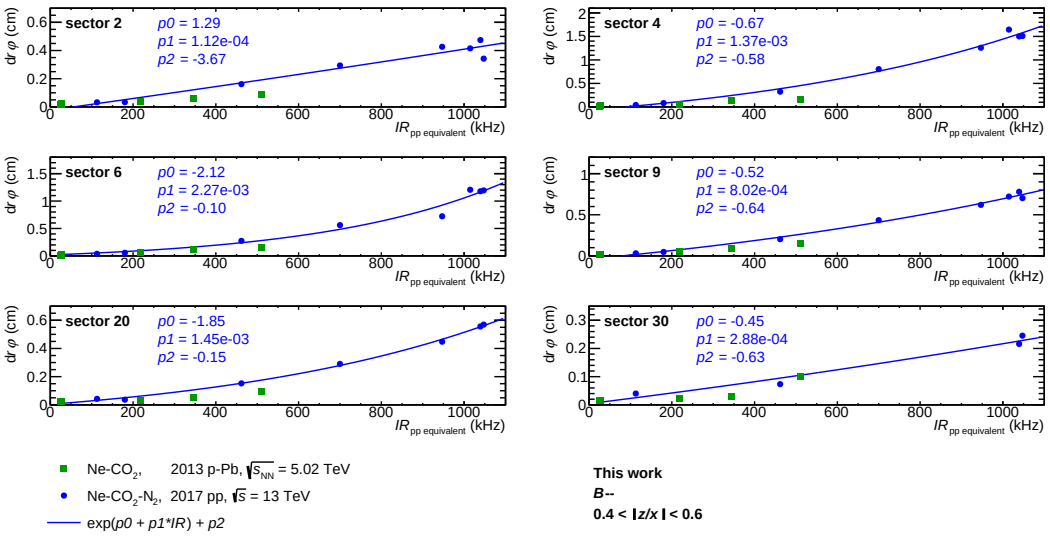

Figure 5.21: The measured space-charge distortions $\mathrm{d}r\varphi$ as a function of the pp-equivalent interaction rate $IR_{\text{pp equivalent}}$ for sectors 2, 4, 6, 9, 20 and 30 at $0.4 < |z/x| < 0.6$ with nominal negative $\boldsymbol{B}$-field. The green markers show the distortions observed in Run 1 p−Pb data with Ne-CO_2, scaling the interaction rate by the average charged-particle density, while the blue markers represent Run 2 pp data with Ne-CO_2-N_2. The blue lines represent fits of the blue markers, using an exponential fit function with a constant offset. The fit parameters are quoted in the plots.

at the other sectors. In order to fully understand this temporary anomalous behavior at sector 30 with Ne-CO_2-N_2, a detailed knowledge of the geometry of the structure at which the space charge is created is required. Further high-intensity tests at around 1000 kHz interaction rate have been performed in 2017. The measured distortions in these as well as in the dedicated interaction rate scan are shown in Fig. 5.21 for sectors 2, 4, 6, 9, 20 and 30 at $0.4 < |z/x| < 0.6$. The results from the analysis of Run 1 p−Pb data with the same (nominal negative) magnetic field are included, scaling the interaction rate by the average charged-particle density as described in the previous paragraph. The Run 2 pp data points are fitted using an exponential with a constant offset. For sector 30, the measurements with uncharacteristically large distortions are removed from the plot. The fits agree well with the data points, which confirms the expectation of an exponential increase with the interaction rate at small space-charge densities or distortions (see Section 5.2.2) at least at sectors 4, 6, 9 and 20.

5.3.3 Comparison to Data with Ar-CO_2

The space-charge density in the TPC depends on the characteristic properties of the gas mixture, particularly on the ion mobility and the amount of primary and secondary ionization. Comparing the Ne and Ar-based gas mixtures used in the TPC, the ion mobility is higher by a factor 1.72 [51] and the total ionization lower by a factor of two [60] with Ne-CO_2-N_2. As the space charge causing the local distortions at specific sector boundaries is created at the ROCs, the amplification factor and the ion backflow also affect the space-charge density. In Run 2, the gain at the anode wires with nominal high-voltage settings was 1.6 times higher with Ne-CO_2-N_2 than with Ar-CO_2. The ion backflow from the active readout area is expected to be below 10^{-4} due to the presence of the GG. As a properly-working GG implies that the space charge is created outside the active readout area, the product of total ionization, gain and ion backflow is an

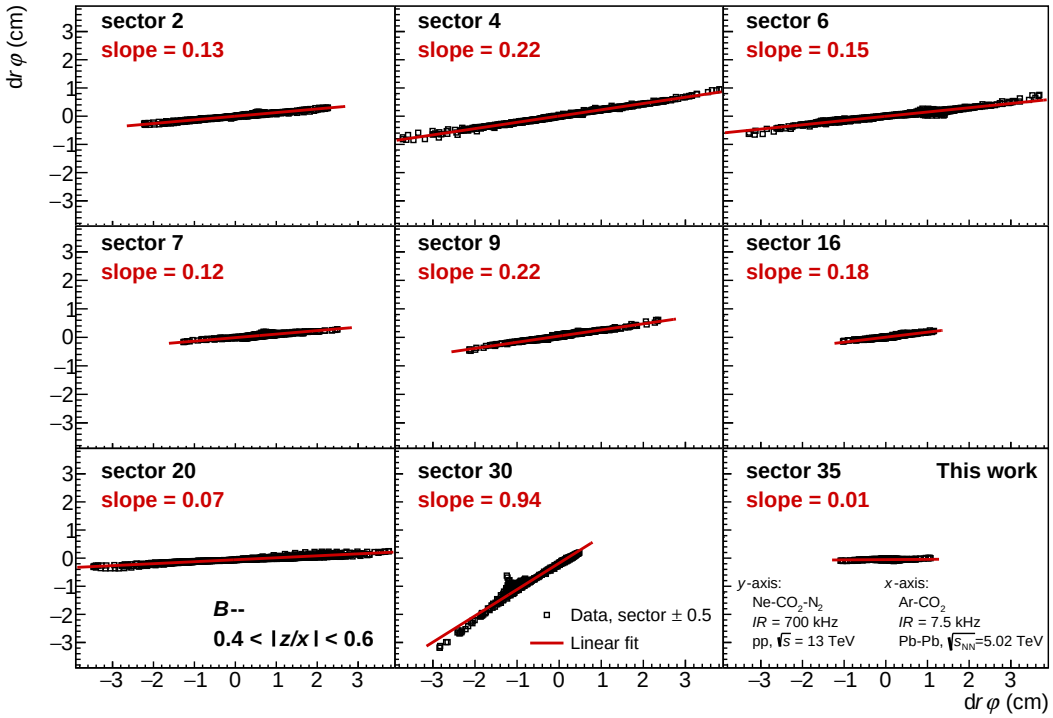

Figure 5.22: The correlation between the local space-charge distortions $dr\varphi$ in two different runs at 9 different sector boundaries for an interval of ± 0.5 sectors and for $0.4 < |z/x| < 0.6$. Each data point represents the distortion measured in one voxel of the IROCs. Two runs taken with nominal negative $\boldsymbol{B}$-field are compared. The y-axis shows the values in a run with Ne-CO_2-N_2 in pp collisions at 700 kHz interaction rate, while the distortions with Ar-CO_2 in Pb−Pb collisions at 7.5 kHz are shown on the x-axis. A linear fit to the data is performed to extract the relative size of the distortions with Ne-CO_2-N_2 from the slope of the fit.

unknown variable when comparing the local space-charge distortions with Ne and Ar and it is impossible to directly measure it. However, the space-charge density is expected to decrease at least by the difference in the ion mobility when switching the gas mixture to Ne-CO_2-N_2.

The local space-charge distortions with Ne-CO_2-N_2 in data taken with pp collisions in 2017 are quantitatively compared to the distortions with Ar-CO_2 in Pb−Pb and pp collisions. For all comparisons, data at nominal negative magnetic field are used. The highest interaction rates in 2015 Pb−Pb collisions were of the order of 7.5 kHz, which is taken as a reference for the size of the space-charge distortions with Ar-CO_2. The pp-equivalent interaction rate, using the average charged-particle density for the normalization, is 577 kHz. It is compared to pp data with Ne-CO_2-N_2 at 700 kHz which was taken during the dedicated interaction rate scan in 2017. The correlation of the local space-charge distortions between those two runs is shown in Fig. 5.22 at different sector boundaries within a range of ± 0.5 sectors for $0.4 < |z/x| < 0.6$. Each point represents the distortion measured in one voxel of the IROCs. Aside from minor deviations of the shape of the distortion spots due to the different collision systems, interaction rates and gas mixtures, a clear linear correlation is observed. The slope of the linear fit to the data defines the relative size of the distortions at each sector with Ne-CO_2-N_2 compared to Ar-CO_2 for these two particular runs. Disregarding sector 30 where some irregular fluctuations of the measured distortions were observed during two periods in 2017 (see

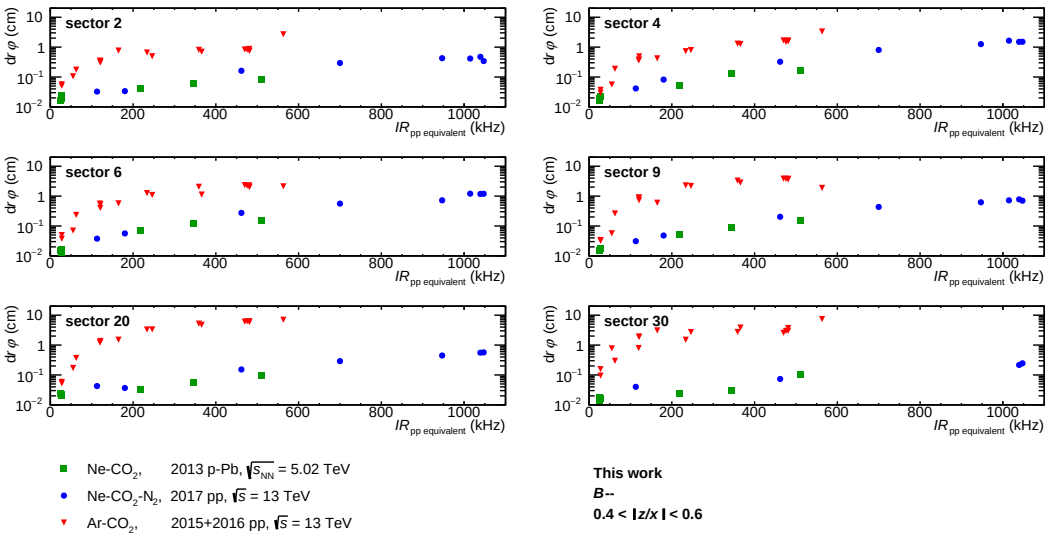

Figure 5.23: The measured space-charge distortions $dr\varphi$ as a function of the interaction rate IR at sectors 2, 4, 6, 9, 20 and 30 for $0.4 < |z/x| < 0.6$. Data with nominal negative $\boldsymbol{B}$-field taken in pp collisions with Ne-CO_2-N_2 (blue markers) and Ar-CO_2 (red markers) are shown together with p−Pb data (green markers). The p−Pb interaction rate is normalized to the average charged-particle density in pp collisions.

Section 5.3.2), the distortions are smaller by a factor between 5 and 10 with Ne-CO_2-N_2. Taking the difference of about 20 % in the (pp-equivalent) interaction rate into account, the amount by which the local space-charge distortions decrease with Ne-CO_2-N_2 is higher by several factors than one would expect from the characteristic gas properties.

Similar results are observed when comparing the distortion with Ne-CO_2-N_2 in the pp data from 2017 to pp data taken with Ar-CO_2 in 2015 and 2016. They are shown as a function of the interaction rate at sectors 2, 4, 6, 9, 20 and 30 in Fig. 5.23. The data taken with Ne-CO_2 in p−Pb collisions in 2013 are also included, normalizing the interaction rate to the average charged-particle density in pp. The highest interaction rate in the Ar-CO_2 data are around 560 kHz as the space-charge distortions are already of the order of several cm. With Ne-CO_2-N_2, interaction rates above 1000 kHz are available as dedicated high-intensity scans were performed in 2017. Still, the distortions are smaller by about a factor of two on the A side and by one order of magnitude on the C side compared to the highest interaction rates with Ar-CO_2. At equal interaction rates, the differences on the A side are again about a factor of 5 to 10 while on the C side, they are close to a factor of 20. From the dependence of the space-charge distortions on the interaction rate with Ne and Ar, respectively, it becomes evident why their difference is bigger than a simple scaling with the interaction rate taking only the gas properties into account. Increasing interaction rates imply a larger amount of ionization and higher space-charge densities and distortions. Since the space charge is created by gas amplification only in small local regions, an increase of distortions also results in a larger area from which primary ionization is attracted to the local amplification region of the space charge, leading to an exponential increase of the space-charge density and the distortions with the interaction rate. This dependence is observed with Ne, where the space-charge distortions are still small. With bigger distortions as in the Ar-CO_2 data, the increasing $\boldsymbol{E}\times\boldsymbol{B}$-effects reduce the exponential rise up to the point where the dependence on the interaction rate becomes linear.

5.4 Dependence on TPC Parameters

The influence of several operational parameters of the TPC on the local space-charge distortions are investigated and presented in this section. Dedicated runs were taken with Ar-CO_2 during pp and p−Pb collisions in 2016, varying the given nominal settings or conditions and performing systematic scans. The dependencies of the distortions on the trigger rate, GG and anode voltages are studied with the goal of identifying the exact origin of the space charge. In order to observe systematic dependencies, the space-charge distortions in the various scans are compared to those in a reference run taken nearby in time with nominal settings and similarly high interaction rate. The data from the scans are scaled by the interaction rate to account for the interaction rate dependence of the distortions, although this method is only an approximation as a non-linear dependence of the distortions on the interaction rate is observed in the previous sections.

5.4.1 Scan of the Trigger Rate

The TPC trigger rate defines the frequency at which the GG is opened in order to collect the ionization created by particles from the event that caused the trigger. At each trigger, the GG stays open for 100 µs to allow electrons to drift the full length of the TPC and then, is closed for at least the amount of time it takes to collect all amplification ions in the ROCs at either the pad plane, cathode or GG wires [60]. Given a transparency of the GG of below 10^{-4} in the closed state [48] and assuming that the large amount of space charge observed locally is created inside the active area of the ROCs, the space-charge distortions have to scale with the trigger rate in order to explain the observed interaction rate dependence (Section 5.2.2).

The nominal trigger rate of the TPC depends on the trigger configuration and it was set at either 400 Hz or 300 Hz for pp collisions in 2016. Two separate runs, at opposite $\boldsymbol{B}$-field polarity, were taken with trigger rates of 196 Hz and 82 Hz, respectively. The respective references for comparison were taken with trigger rates of 392 Hz and 257 Hz, meaning the trigger rate was decreased by a factor of two and more than three in the dedicated scans. The correlation between the space-charge distortions in the run with reduced trigger rate and those in the corresponding nominal reference are shown in Fig. 5.24. A range of ±0.5 sectors around sectors 2, 4, 6, 7, 9, 16, 20, 30 and 35 and the region close to the CE ($|z/x| < 0.2$) are selected. For each sector, the nearly perfect linear correlation of the data is fitted by a first order polynomial to extract its slope representing the relative difference of the distortions in the scans. The values are generally different at each sector. In the run with the trigger rate decreased by 50 %, the space-charge distortions actually increase at all sectors by up to 17 % (sector 35). In the other scan, no systematic dependence is observed after lowering the trigger rate by a factor of about three, as the slopes are close to one at most sectors. The comparison of the space-charge distortions in the two scans with decreased trigger rate to the nominal references is in agreement with the distortion fluctuations observed in Section 5.2.3, implying no dependence on the trigger rate of the TPC. From this observation, the interaction rate dependence of the local space-charge distortions can only be explained by a local transparency of the GG in the closed state which is of the same order as the transparency in the opened state, if the space charge originates inside the active amplification region of the ROCs. The other possibility is that the space charge is created outside the active area of the ROCs.

5.4.2 Transparency of the Gating Grid

The working principle and operational parameters of the GG are explained in Section 4.1.2. The GG transparency is defined by the constant offset voltage V_{G} and the bipolar bias

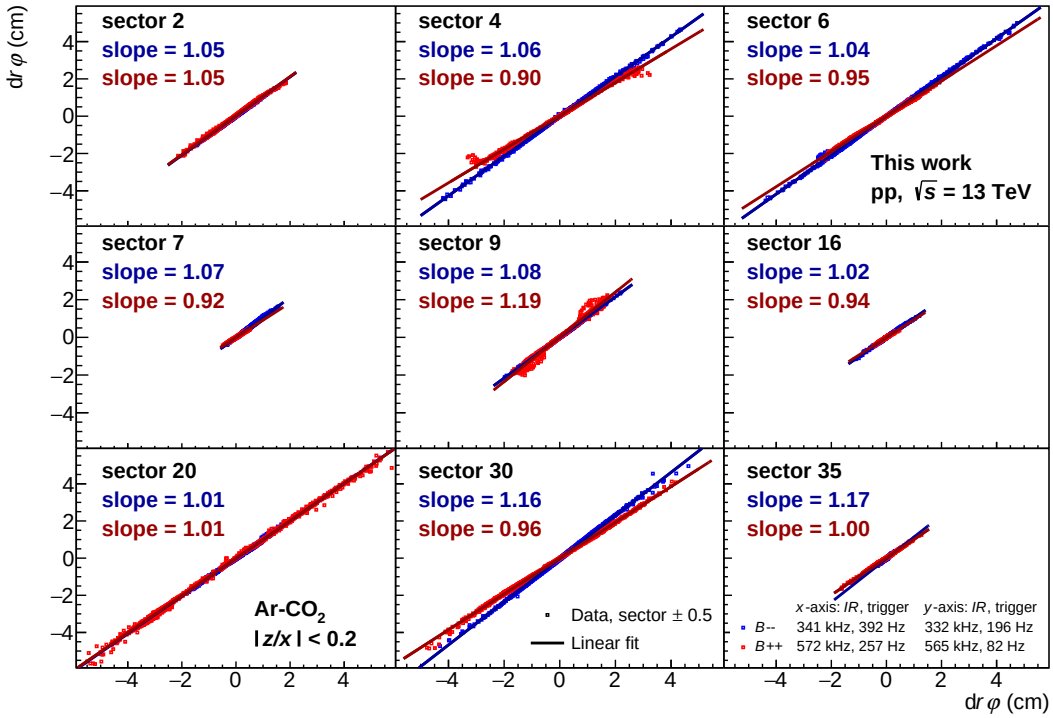

Figure 5.24: The correlation of the measured space-charge distortions $dr\varphi$ between runs with decreased trigger rate (y-axis) and corresponding references with nominal settings (x-axis). It is shown at nine sectors within a range of ± 0.5 sectors and at $|z/x| < 0.2$. The blue markers represent data at nominal negative $\boldsymbol{B}$-field, for which the trigger rate is decreased by 50 %. Data, taken with nominal positive magnetic field, for which the trigger rate is decreased by a factor of about three is shown with red markers. The solid lines represent linear fits to the data points. The slopes of the fits are quoted as colored text.

voltage ΔV. In the case that the space charge is created in the amplification region of the ROCs, the GG should be inefficient in the corresponding local regions so that the positive ions can escape from the amplification region into the drift volume. Therefore, the measured local space-charge distortions are expected to scale with the GG transparency and to depend on the potentials at the GG wires. The GG voltages were varied in several runs to study this dependence. Furthermore, the local efficiency of the GG is studied in data with the GG permanently closed and different drift fields.

Scan of the GG Potentials

Three scans of the offset and bias voltage in the IROCs were performed. In the first run, the offset voltage was changed from its nominal value of $-70\,\mathrm{V}$ to $-10\,\mathrm{V}$. From electrostatic simulations [27], the electron transparency is expected to decrease by a few percent in the open mode, resulting in less total positive charge produced in the ROCs. Furthermore, the modified potential offset in the closed mode with respect to the cathode wires and the CE can lead to second-order modifications of the transparency from either side of the GG. In the subsequent run, ΔV was increased from $\pm 90\,\mathrm{V}$ to $\pm 120\,\mathrm{V}$ with the nominal offset voltage, which is expected to decrease the transparency in the closed state even further than the nominal value of below 10^{-4}. In another run taken about one week later, ΔV was increased even more to $\pm 130\,\mathrm{V}$. All data are taken with nominal positive magnetic field.

The results of all three scans are presented in Fig. 5.25. It shows the correlation between

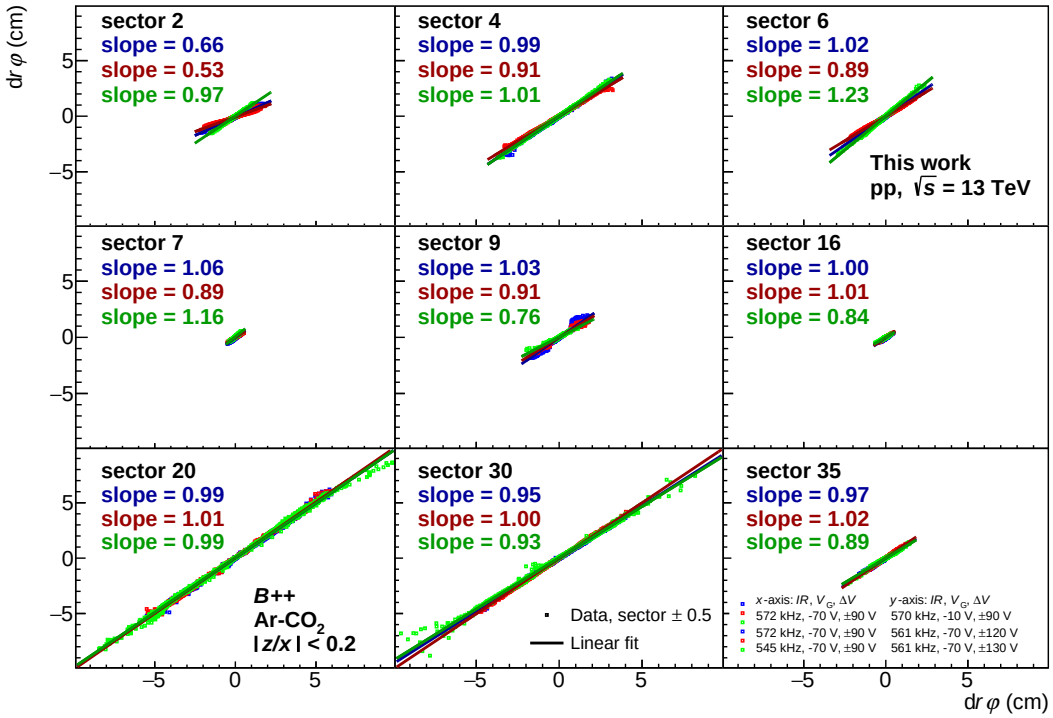

Figure 5.25: The correlations of the measured distortions $\mathrm{d}r\varphi$ between scans of the GG voltages (y-axis) and a corresponding reference with nominal settings (x-axis). The colored markers represent three scans in which either the GG offset voltage or bias voltage was changed. The data were taken at positive $\boldsymbol{B}$-field with Ar-CO_2 and are shown at different sectors within an interval of ± 0.5 sectors for $|z/x| < 0.2$. The solid lines are linear fits to the data points and the respective slopes indicate the change of the distortions relative to the reference.

the space-charge distortions at the different sector boundaries measured in a run with modified GG voltages and those in a reference run with nominal settings at similar interaction rate. The region of $|z/x| < 0.2$ is selected. Linear correlations are observed for all three scans. The data points are fitted with a polynomial of first order to determine the relative change of the distortions in the scans with respect to the reference by the slope of the fit. In the first scan with reduced offset voltage, the deviations of the slopes from one is of the order of a few percent at all sectors except at sector 2. Here, the space-charge distortions are smaller by 34 % in the scan. In the second scan with $\Delta V = \pm 120\,\mathrm{V}$, the distortions decrease by about 10 % at most sectors on the A side. The exception is again sector 2 where the distortions even decrease to close to 50 %. On the C side however, the slopes are equal to one within 2 %. Further increasing ΔV to $\pm 130\,\mathrm{V}$, the space-charge distortions decrease further at some sectors but the opposite trend is observed at others. While sectors 30 and 35 on the C side show a decrease of about 10 % and sector 9 on the A side of 24 %, the distortions at sectors 6 and 7 are larger by up to 23 % compared to the reference with nominal settings. Taking the uncertainty of the linear interaction rate scaling into account, no systematic dependence of the distortions on the voltages of the GG can be concluded. The deviations of the correlations from one in the different scans are mostly compatible with the expected space-charge density and distortion fluctuations (Section 5.2.3).

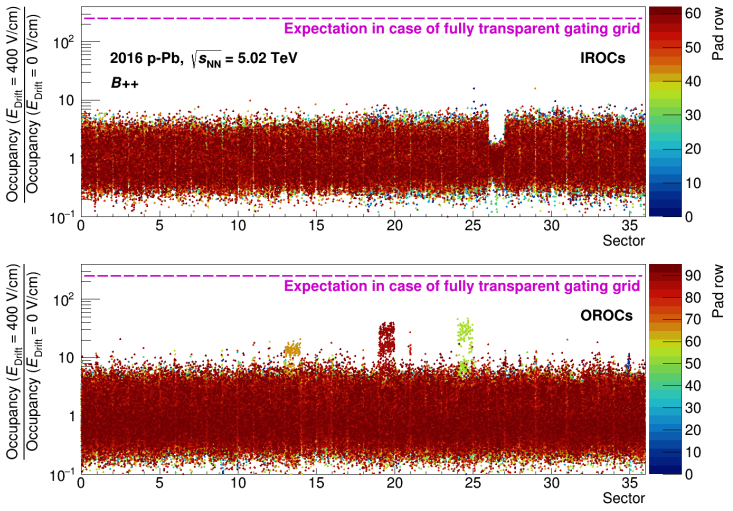

Figure 5.26: The ratio of relative pad occupancies as a function of the sector and the pad row for IROCs (*upper plot*) and OROCs (*lower plot*) [62, 72]. Data from two runs are compared. The GG was kept in a closed state in both runs, while the drift field E_{Drift} was switched off in one of them to keep ionization created in the drift volume from drifting towards the ROCs. The expected value of the ratio in case of a fully transparent GG is indicated by the dashed line.

Cluster Occupancy with Closed GG

The proper functionality and local efficiency of the GG are validated using data collected in two runs with special settings. In both runs, the GG is kept in the closed state in the event of a trigger while still reading out the signals induced on the pads by ionization inside the volume of the ROCs. In the first run, the nominal drift field of 400 V/cm was applied so that ionization electrons created in the drift volume would move along the drift field towards the ROCs. In case of local inefficiencies of the GG, a fraction of the ionization proportional to the GG transparency would enter the ROC volume and induce additional signals on the pads. In the second run, the potentials at the CE and the field cage were set to zero, switching off the drift field. The ionization electrons from the drift volume never reach the ROCs and the only signals read out come from ionization created in the ROC volume.

The ratio of the pad occupancies in those two runs is analyzed [62] to determine the efficiency of the GG. Here, the pad occupancy is defined as the number of signals above the threshold on each pad normalized to the median. In case of a transparency of 100 %, the occupancy with nominal drift field is expected to be larger by a factor of about 250 compared to the data taken without drift field. This factor is estimated from the geometrical parameters of the TPC, assuming a constant drift velocity, as the length of the drift volume is about 250 times larger than the thickness of the ROCs. The occupancy ratio measured in the IROCs and OROCs is shown in Fig. 5.26 as a function of the sector and the pad row. It spreads around one in all of the IROCs. Specifically at the sector boundaries where large local space-charge distortions are observed, no deviation from the bulk is observed. The results in the OROCs are the same except for sectors 13 (OROC A13), 19 (OROC C01) and 24 (OROC C06), where the ratio increases to 20, 40 and 50, respectively, at one or two of the pad rows. At the given pad rows of these chambers, it is known that there are one (sectors 13 and 19) or two adjacent (sector 24) floating GG wires. In case of one floating wire, the polarity of the bias potential can be chosen such that the transparency for ions stays minimal, however implying full transparency for electrons. This is not the case anymore for two adjacent

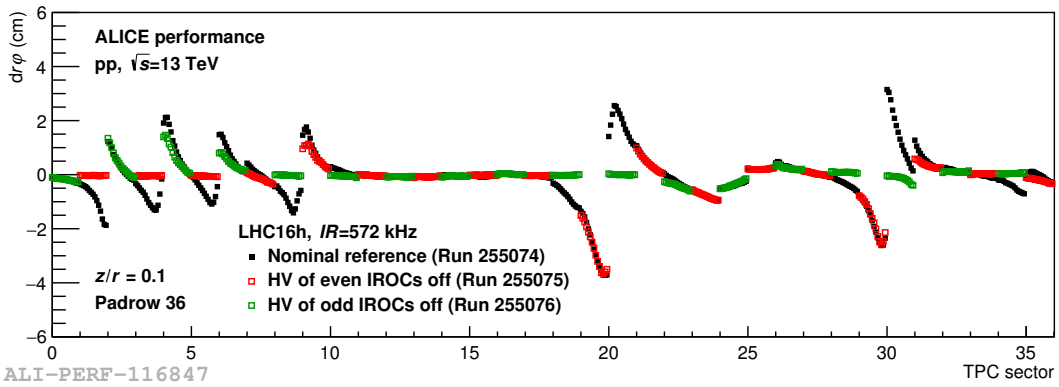

Figure 5.27: The space-charge distortions $dr\varphi$ measured at pad row 36 and at $|z/x| < 0.2$ as a function of the sector. The black full markers show the data for a reference with nominal anode high-voltage settings at 572 kHz interaction rate (IR). The red open markers show the data measured with only odd-numbered IROCs in a run where the high voltage of all even-numbered IROCs was switched off. The green open markers represent the opposite scenario in a run where all odd-numbered IROCs were switched off.

floating GG wires. Therefore, the GG is transparent for electrons over a fraction of a single pad row in OROC A13 and OROC C01 and also for ions in the case of OROC C06. The measurement confirms that the GG wires in the IROCs are fully efficient in terms of electron transparency in the closed state, so that no additional charge is created in the ROCs while the GG is closed.

5.4.3 Potential at the Anode Wires

The most likely mechanism to produce a large amount of positive ions which cause the local space-charge distortions is by gas amplification at the high potentials close to the anode wires. The dependence of the space-charge distortions on the anode high-voltage is studied in order to rule out any other sources. In a first scan, the high voltage of every other IROC was completely switched off, i.e. signals and, therefore, distortions can only be measured by the other half of the chambers. In the subsequent run, the high voltage of the other half of the chambers was switched off. These data allow to determine if the space charge is created at the anode wires of single IROCs or if the space-charge distortions are independent of the anode high-voltage. In a second scan, the anode high-voltage is decreased in steps to study the correlation between the size of the distortions and the anode wire gain.

Runs with IROCs Turned Off

Two consecutive runs were taken in which the anode high-voltage of the even and odd-numbered IROCs, respectively, was switched off. As the local space-charge distortions are always located at the boundary between two chambers, they are still seen in the remaining IROCs, if the space charge is still present. For comparison, a run with nominal high-voltage settings was taken right before the scan as a reference for the usual space-charge distortion patterns. All three runs were taken at a similar interaction rate of about 570 kHz. The distortions measured in this scan are shown as a function of the sector in Fig. 5.27. The nominal reference scenario is drawn with the black full markers. The distortions with the even-numbered IROCs switched off (red open markers) are only measured by the odd-numbered IROCs and vise versa (green open markers). The data are shown for pad row 36 and at $|z/x| < 0.2$. It is observed that the space-charge distortions appear or disappear when certain IROCs are switched on or off. This implies that the space charge is created

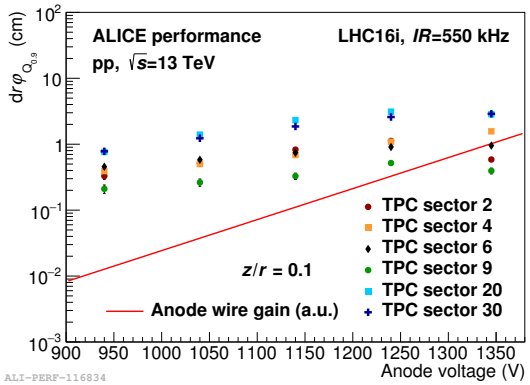

Figure 5.28: A robust estimate (refer to the text for more details) of the measured local space-charge distortions $\mathrm{d}r\varphi_{Q_{0.9}}$ close to the CE ($z/r = 0.1$) at different sector boundaries (colored markers) as a function of the high voltage at the anode wires of the IROCs. The data are taken at interaction rates of around 550 kHz. The solid red line represents the relative anode wire gain expressed in arbitrary units (a.u.).

by gas amplification at the anode wires of single IROCs. Performing further analysis of the data using all pad rows at each sector boundary, the IROCs at sectors 2 (A02), 4 (A04), 6 (A06), 7 (A07), 9 (A09), 10 (A10), 16 (A16), 19 (C01), 29 (C11), 30 (C12) and 35 (C17) are identified as the sources of the space charge. For all these chambers, the space charge is created on that side of the chamber where the cathode wires were soldered and the anode and GG wires were cut off at the edge of the wire ledge during production, as illustrated in Fig. 4.3.

Scan of the Anode High-Voltage

A detailed study of the high-voltage dependence of the space-charge distortions is performed by varying the potentials at the anode wires of the IROCs at sectors 2, 4, 6, 9, 20 and 30. In consecutive runs, the high voltage of these IROCs was set to 1240 V, 1140 V, 1040 V, 940 V and 1345 V, with 1345 V being the nominal IROC voltage with Ar-CO_2. In the same way as when half of the IROCs were fully switched off, the space-charge distortions are measured in the adjacent IROCs at sectors 1, 3, 5, 8, 19 and 29. The interaction rate in all of these runs was leveled at around 550 kHz. The results of this scan are presented in Fig. 5.28. The plot shows a robust estimate of the measured distortions in $r\varphi$-direction at the given sector boundary close to the CE ($z/r = 0.1$) as a function of the anode high-voltage. The robust estimate used here corresponds to the 90th percentile of the sorted array of absolute distortions $\mathrm{d}r\varphi$ measured in the IROCs within ± 0.5 sectors around the given sector boundary. An exponential dependence is observed for the space-charge distortions at lower high voltage while the slope of the dependence tends to decrease towards higher voltages at some sectors. The latter observation indicates signs of saturation with increasing high voltage although measurements with even higher voltages would have been necessary to make a firm conclusion. The plot also contains the high-voltage dependence of the relative anode wire gain drawn by the solid red line for comparison, which follows a strict exponential dependence. While the anode wire gain at 1240 V drops to around 33 % of the nominal value, the effect on the space-charge distortions is significantly smaller or there is even no effect at all at some sectors. Decreasing the high voltage further, the anode wire gain at 940 V is below 2 % while local space-charge distortions of several mm were still measured. Both the measured space-charge distortions and the anode wire gain depend exponentially on the high voltage at the anode wires, but the slope of the distortions is much smaller than the one of the anode wire gain. Together with the results from

Section 5.4.3, the observations clearly show that the production mechanism of the space charge is connected to gas amplification at the anode wires. However, the significant differences in the comparison to the anode wire gain indicate that the positive ions causing the local space-charge distortions are created in a different way or at a different place than the ions from the usual gas amplification process which generates the signals in the active area of the ROCs.

5.5 Origin of the Space Charge

The knowledge about the exact origin of the space charge is important to develop an effective mitigation strategy and to reduce the effect as much as possible. From the measurement of the space-charge distortions, it is deduced that the space charge is located within a very local region in radius and at the φ-boundaries between the affected sectors. However, it is unclear whether the positive ions are created in-between two readout chambers, i.e. inside the 3 mm gap, or close to the edge of the active area of one readout chambers. The results presented in the previous section indicate that the space charge is created by gas amplification at the anode wires. In the nominal design of the TPC readout, there are no amplification structures in the gap between adjacent ROCs as the anode wires are cut at the outside edge which is then covered by an additional layer of epoxy (Section 4.1.2). On the other hand, the dependence of the space-charge distortions on the high voltage of the IROCs significantly differs from the one of the nominal gain in the active readout region. This suggests that, in case the space charge originates at the edge of the active readout region, there are effects in addition to the nominal gas amplification that lead to the distinct high-voltage dependence. Furthermore, the measurements of the cluster occupancy with closed GG (Section 5.4.2) demonstrate the full efficiency of the GG in the affected regions in terms of blocking electrons from the drift volume. This is not necessarily directly transferable to the efficiency of blocking ions from the other side but the fact that the wires run along the full azimuth requires an additional effect which renders the GG partially transparent for ions at only a small φ-region close to the chamber edge.

Further studies are carried out in [62] in order to narrow down the location of the space charge in $r\varphi$. They are summarized in this and the next paragraph. The pad occupancy with and without space-charge distortions is compared using Pb−Pb data taken at high (7.5 kHz) and low (<100 Hz) interaction rate. The occupancy is proportional to the number of clusters N_{cl} measured on the pads and to the pad width w. As the space-charge distortions affect the drift path of ionization electrons w.r.t. their nominal drift path without distortions, the number of clusters on a given pad is expected to also be modified. The spatial distribution of the ratio of pad occupancies of high to low interaction rate is used to determine the center of gravity towards which the electrons are deflected by the space charge, which corresponds to the center of gravity of the space-charge distribution. It is extracted with extremely high space-granularity since the occupancy is measured on the pad level. Furthermore, the ratio of the occupancies can approximately be written as

$$\frac{N_{\mathrm{cl}}(\text{high IR})}{N_{\mathrm{cl}}(\text{low IR})} = 1 + \frac{(\mathrm{d}r\varphi(r\varphi + w/2) - \mathrm{d}r\varphi(r\varphi - w/2))|_{z\approx 125\,\mathrm{cm}}}{w} \,, \tag{5.2}$$

where $\mathrm{d}r\varphi(r\varphi \pm w/2)|_{z\approx 125\,\mathrm{cm}}$ are the space-charge distortions along $r\varphi$ at the azimuthal pad boundaries averaged over the full drift. The right side of the equation corresponds to the derivative of the distortions w.r.t. $r\varphi$. As the gradient of the space-charge distortions increases towards the boundaries between two sectors, the derivative is expected to provide a much sharper pattern than the measured space-charge distortions themselves. The occupancy ratio at sector 4 as a function of the pad row and the distance to the

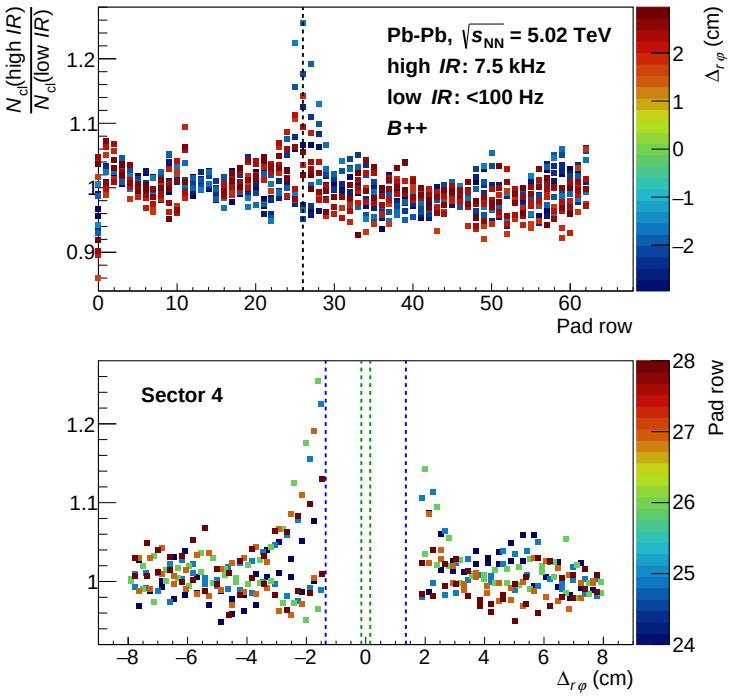

Figure 5.29: The ratio of normalized pad occupancies in Pb−Pb data of high (7.5 kHz) to low (<100 Hz) interaction rate $\frac{N_{\text{cl}}(\text{high IR})}{N_{\text{cl}}(\text{low IR})}$ at sector 4 [62, 72]. The data was taken with nominal positive $\boldsymbol{B}$-field. *Top:* The ratio is shown as a function of the pad row and the distance to the sector boundary $\Delta_{r\varphi}$ on the color axis. The dashed line indicates the radial position of the space charge obtained from the center of the sharp peak. *Bottom:* The ratio as a function of the distance to the sector boundary $\Delta_{r\varphi}$ and the pad row on the color axis. The green dashed lines represent the gap between two ROCs and the blue dashed lines indicate the edge of the active readout area of the respective ROC.

sector boundary ($\Delta_{r\varphi}$) is shown in Fig. 5.29. In the upper plot, a sharp peak highlighted by the dashed line is observed at pad row 26, indicating the location of the space charge in radial direction. Similarly sharp peaks at different positions are present in the data for the other sectors with space-charge distortions. The lower plot shows the distribution along the $r\varphi$-direction for pad rows around pad row 26. The green dashed lines represent the gap between two ROCs and the blue dashed lines mark the edges of the active readout area of the respective ROCs. The symmetry axis of this distribution indicates the position of the space charge in $r\varphi$ and its origin. Although there are no data points beyond the active readout region, it is clear that the symmetry axis is centered in the gap between ROCs instead of being significantly shifted towards the edge of the active readout area of either ROC. This is also the case for the distributions at all other sector boundaries with space-charge distortions. This observation strongly implies that the space charge is created inside the gap between two ROCs.

Other studies in [62] adopt an analytical model to fit the measured space-charge distortions d$r\varphi$ as a function of the position in the TPC. According to Eq. (3.12), the space-charge distortions d$r\varphi$ can be approximated by

$$\mathrm{d}r\varphi = \frac{L_{\text{drift}}}{E_z}(E_{r\varphi} - \omega\tau E_r) \,, \tag{5.3}$$

where L_{drift} is the drift distance of the electron, E_z is the nominal drift field of 400 V cm^{-1} and $E_{r\varphi}$ and E_r are assumed to be constant along the drift path which corresponds to a

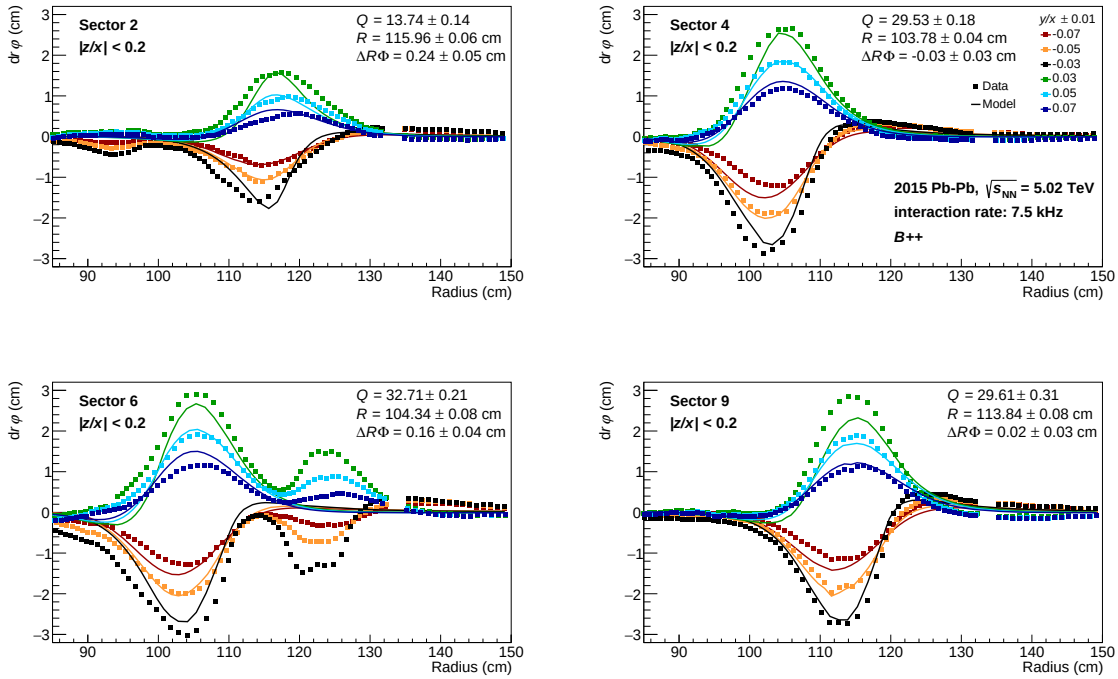

Figure 5.30: The space-charge distortions $dr\varphi$ measured at four sectors on the A side are shown by markers as a function of the radius for $|z/x| < 0.2$ [62, 72]. The color of the markers indicates the distance to the given sector boundary in units of y/x. The measurement is taken with Pb−Pb collisions at 7.5 kHz interaction rate and nominal positive $\boldsymbol{B}$-field. The solid lines represent the results of the analytical model which is used to fit the data. The fit parameters for the potential (Q) and the position (R, $\Delta R\Phi$) of the line charge are quoted in the plots.

straight-line drift of the ionization electrons. Eq. (5.3) is valid for small distortions caused by a line charge with constant charge density along the drift direction z. Then, the radial and azimuthal electric fields are defined by Gauss's law as

$$E_r(r, r\varphi) = \sum_{i=0}^{N} \frac{(r - R_i)Q_i}{(r - R_i)^2 + (r\varphi - R\Phi_i)^2 + \Delta 0_i^2} \,, \tag{5.4}$$

$$E_{r\varphi}(r, r\varphi) = \sum_{i=0}^{N} \frac{(r\varphi - R\Phi_i)Q_i}{(r - R_i)^2 + (r\varphi - R\Phi_i)^2 + \Delta 0_i^2} \,, \tag{5.5}$$

where $Q = \frac{\lambda}{2\pi\varepsilon}$ is the potential of the line charge and R and Φ are its position in radius and azimuth, respectively. The constant term $\Delta 0$ introduces a minimum distance to the line charge, which is representative of a finite width in the azimuthal plane. The model can be extended by summation over different line charges with indices i. Fitting the data with this model using only one line charge for simplicity, the position as well as the charge density of the space charge can be obtained from the fit parameters at the different sector boundaries. The results for four sectors on the A side are visualized in Fig. 5.30 which shows the measured space-charge distortions as a function of the radius for $|z/x| < 0.2$. The distance to the given sector boundary in units of y/x is represented by different colors. The fitted model is drawn with solid lines and qualitatively agrees very well with the data, considering its simplicity. At sectors where the distortion pattern is more complex and there are two or more line charges, like at sector 6, only one of the lines is fitted by the model. The fit parameters quoted in the plots indicate that the radial position of the

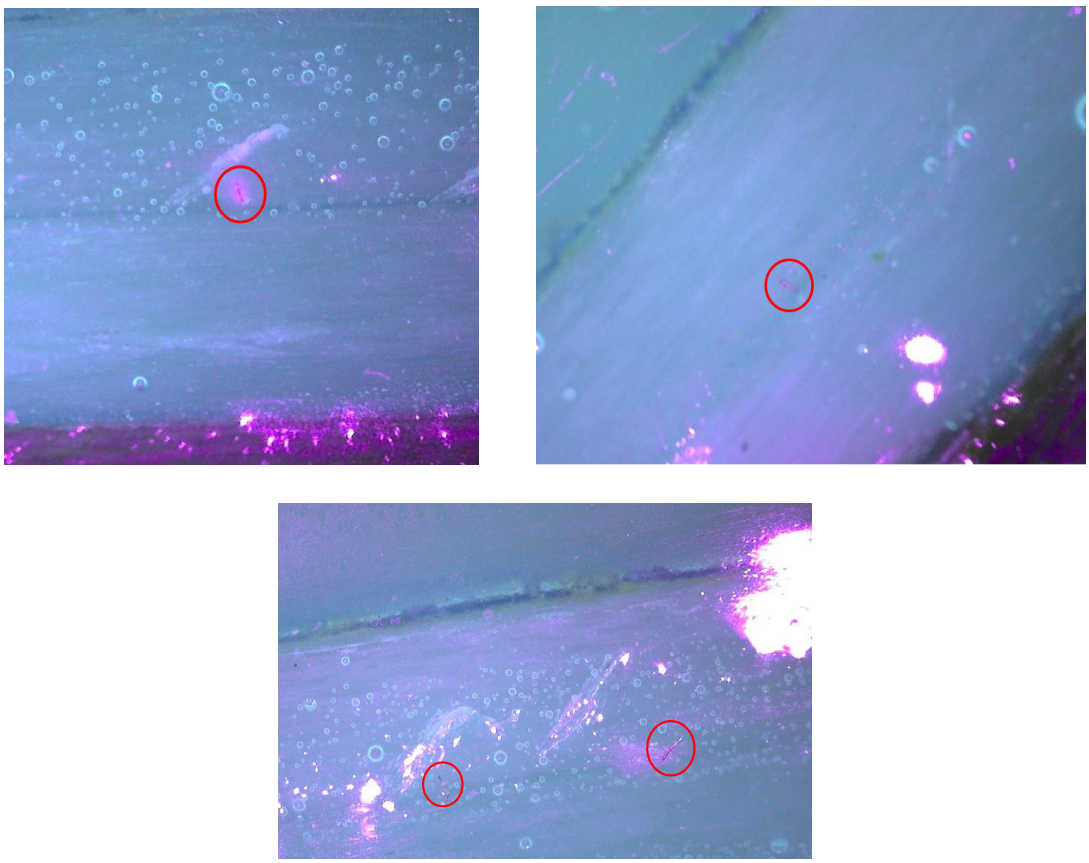

Figure 5.31: Wire tips (marked with red circles) sticking out into the layer of epoxy on the outer edge of IROC A02 (*top left*), IROC A06 (*top right*) and IROC A04 (*bottom*) [73].

lines can be quite different depending on the sector. However at all sectors, the azimuthal position $\Delta R\Phi$ w.r.t. the sector boundary is compatible to being inside the region of the gap between two chambers which has an extent of $|\Delta R\Phi| \leq 0.15\,\text{cm}$. Moreover, it is demonstrated in [62] that the position of the space charge obtained from this model is constant over long periods of time for a given polarity of the magnetic field.

5.5.1 Investigation of the Readout Chambers

During Long Shutdown 2 of the LHC in 2019–2021, the ROCs of the TPC were exchanged by ROCs equipped with stacks of four GEM foils [18, 19, 49]. After the extraction of the MWPCs, those which were affected by large local space-charge distortions were investigated by TPC hardware experts [73]. Their outer edges were surveyed with a microscope camera for suspicious structures which could cause amplification in the gap between two ROCs. For all ROCs which were surveyed, it was found that one or more tips of anode wires were sticking out from the ledges into the layer of epoxy at the outer edge (Fig. 4.3), or possibly even out of the epoxy layer, close to the radii where the large space-charge distortions were observed. Three photographs from the microscope camera survey are shown in Fig. 5.31 as examples of some of the visible wire tips of IROCs A02, A04 and A06. During operation, these anode wire tips induce high electric fields, which result in gas amplification of primary and secondary ionization drifting inside the gap. The positive amplification ions drift back from the gap into the active drift volume since there is no mechanism like the GG, resulting in the observed space-charge distortions. This final survey of the ROCs confirmed the initial conclusions from the observations discussed so far and it validated the studies and the strategy to mitigate the space-charge distortions presented in the next section.

5.6 Dependence on the Cover-Electrode Voltage

The strong evidence for the origin of the space charge lying inside the gap between two readout chambers points out that the only way to decrease the amount of space charge and to mitigate the distortions is via the cover electrodes mounted on top of the wire ledges (Section 4.1.2). The nominal voltage at the cover electrodes of $-180\,\mathrm{V}$ is tuned to match the potential of the drift field, minimizing the static distortions close to the edges of the active area of the ROCs and, consequently, also at the outer edges of the ROCs which face the gap. As the interaction-rate dependence of the space-charge distortions (Section 5.2.2) implies a dependence on the primary ionization, the proper adjustment of the cover-electrode voltage is expected to decrease the number of ionization electrons which reach the volume inside the gap between two ROCs and, therefore, also the amount of space charge which is produced by gas amplification. As a part of this thesis, electrostatic simulations (Section 5.6.1) are carried out in order to study by how much the amount of ionization ending up both inside the gap and at the edge of the active area of the ROCs is affected by the cover-electrode voltage. The results of the simulations were used to define the values for systematic scans of the cover-electrode voltage in the experiment (Section 5.6.2) and they are compared to the measured data obtained in these scans (Section 5.6.3). The final new nominal settings of the cover-electrode voltage are determined using the results of the systematic scans, minimizing the space-charge distortions as much as possible for the last Pb−Pb run of Run 2 in 2018.

As the electrostatic potential in the TPC drift volume, applied by the CE and the field cage, has negative sign by design, an increase of the cover-electrode potential towards more positive values is expected to deflect the ionization electrons in the vicinity of both edges of the cover electrode towards the cover electrode itself. Introducing such static distortions will lead to a loss of ionization at the edges of the active readout area but it will also decrease the amount of ionization entering the volume between two ROCs. Another option is to apply different voltages on the adjacent cover electrodes of two ROCs, effectively deflecting the ionization electrons between the two ROCs towards one of the cover electrodes. Both of these scenarios are studied in simulations and with data.

5.6.1 Electrostatic Simulations

The 3-dimensional calculations of the drift of ionization electrons inside the TPC volume close to the ROCs are performed with the Garfield software [74]. A 2D projection of the simulated 3D cell geometry is shown in the plots of Fig. 5.32 which illustrate the drift paths of ionization electrons with different cover-electrode potentials. The elementary cell is centered around the gap of 3 mm between two ROCs and it contains all essential elements of the ROCs described in Section 4.1.2. The dimensions of the single elements, e.g. wire pitches and thickness or the size of the wire ledges, can also be found in Section 4.1.2. The anode, cathode and gating grid wires run along the y-direction and they are arranged along x. The nominal wire potentials are used in the simulation, i.e. 1345 V, $-70\,\mathrm{V}$ and 90 V for the anode, GG offset and GG bias potential, respectively, and 0 V as ground for the cathode wires. Different to the real experiment where the wires are cut either behind the soldering point or at the outside edge of the wire ledge, depending on the wire type and the side of the ledge, all wires have their end points at the outside edge of the wire ledge in the simulation. Only one wire ledge, the one at the gap in the center of the cell, for each of the two ROCs is implemented in the simulation. The wire ledges consist of four dielectric elements, divided by the three wire planes, with a relative permittivity (ε_r) of 4.8. They have a total height of 1 cm and a width of 1.15 cm. There is a 100 µm thick cover electrode on top and a 500 µm thick layer of epoxy, simulated by a dielectric with $\varepsilon_r = 6$, at the outside edge of each ledge. The drift direction corresponds to z. A 2 mm thick cathode plane is placed 2 cm above the cathode

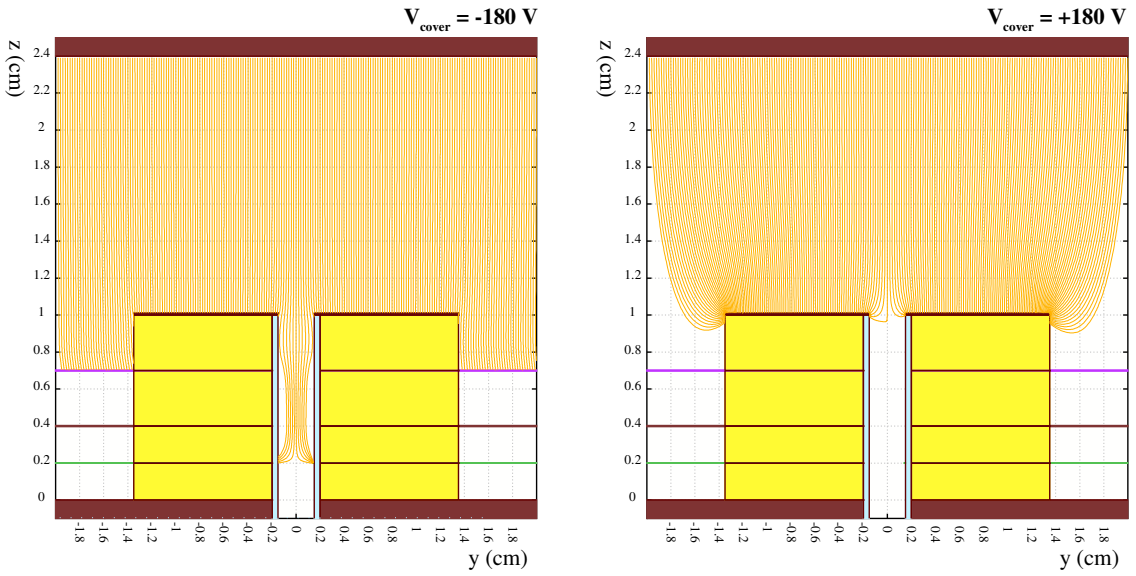

Figure 5.32: Visualizations of the 3D simulation of the electron movement close to the boundary between two ROCs, projected onto the y-z plane. The *left* plot shows results from the simulation with nominal potentials at all the electrodes while the voltage at both cover electrodes is increased from $-180\,\mathrm{V}$ to $+180\,\mathrm{V}$ in the simulation on the *right*. Both simulations are performed for Ar-CO_2 (90-10) and with a magnetic field $\boldsymbol{B}$ of $-0.5\,\mathrm{T}$ along z. The anode wires are drawn by green lines, the cathode wires by brown lines and the GG wires by purple lines. The cathode plane, the pad plane and the cover electrodes are illustrated by brown boxes, the wire ledges by yellow boxes and the thin layer of epoxy by light-blue boxes. The orange lines represent the drift paths of electrons starting close to the cathode plane.

wire grid. It is set to a potential of $-800\,\mathrm{V}$ and represents the high-voltage electrode. A 2 mm thick electrode at ground and a 2 mm thick dielectric with $\varepsilon_r = 4.7$ simulate the pads and the PCB of the pad plane. A 5 mm thick dielectric with $\varepsilon_r = 4.8$ and a 1.5 cm thick electrode represent the support structure for the pad plane and the aluminum body. Furthermore, another 2 mm thick electrode at ground is placed at a distance of 3.3 cm below the pad plane as the TPC end plate. The elementary cell has dimensions of $\pm 0.5\,\mathrm{cm}$ in x and $\pm 4\,\mathrm{cm}$ in y. In order to provide a uniform field using the nominal potentials, 50 periodic copies to both sides of the elementary cell are used in x and one periodic copy to each side in y. The resulting potential and electric field in the cell are calculated in Garfield via an interface to neBEM (nearly exact Boundary Element Method) [75]. In addition to the electric field, a magnetic field of $|B| = 0.5\,\mathrm{T}$ in z-direction is applied. The electron transport properties for Ar-CO_2 (90-10) at 300 K temperature and a pressure of 1 atm are then calculated by the interface to Magboltz [59]. For the simulation of the movement of ionization electrons, transverse and longitudinal diffusion are neglected. They are detector-specific statistical processes which smear out the arrival point distribution of ionization electrons. On average however, the arrival points are determined by the electric and magnetic fields. Therefore, switching off diffusion in the simulation relaxes the requirements for the statistics in terms of the number of electrons which need to be simulated.

The drift lines of electrons, starting close to the cathode plane and distributed randomly in x and y, are calculated for a large variety of different cover-electrode potential combinations. Both scenarios with identical potentials at adjacent cover electrodes of two

ROCs and scenarios with different potentials are considered. In general, the combination of potentials of two adjacent cover electrodes (V_{cover}) can be defined by the cover-electrode offset voltage ($V_{\text{cover,offset}}$), with $V_{\text{cover,offset}} = (V_{\text{cover1}} + V_{\text{cover2}})/2$, and the respective bipolar difference to the offset voltage of the individual cover electrodes (ΔV_{cover}), with $\Delta V_{\text{cover}} = (V_{\text{cover1}} - V_{\text{cover2}})/2$. In the simulations, cover-electrode voltages which are around the nominal values and which are considered to be safe for the hardware are used as well as more extreme values which provide some extrapolation power. The plots in Fig. 5.32 show two examples for simulated electron drift lines with settings of $V_{\text{cover}} = -180\,\text{V} \pm 0$ (nominal values) and $V_{\text{cover}} = +180\,\text{V} \pm 0$. Significant static distortions of the electron drift paths are introduced when the potential is increased from nominal to $+180\,\text{V} \pm 0$, affecting both the amount of electrons entering the gap between the two ROCs as well as those at the edge of the active readout area. Two quantities are defined in order to quantify the effect of modified cover-electrode settings on the amount of collected ionization. The fraction of the total number of electron drift lines which enter the gap for a given cover-electrode setting relative to the same fraction with nominal settings is calculated as N_{gap}. Drift lines entering the gap are defined by a selection on their end-point coordinates y and z, requiring that $|y| \leq 0.15\,\text{cm}$ and $z \leq 1\,\text{cm}$. The fraction of the total electron drift lines for given cover-electrode voltages which have their end point at the edge of the active readout area relative to the fraction with the nominal cover-electrode potential as quantified as N_d. Here, electron drift lines are selected for which their end-point coordinate y is between the edge of the wire ledge ($|y| \geq 1.35\,\text{cm}$) and a distance d from the edge and for which $z \leq 1\,\text{cm}$. It is found that $d = 5\,\text{mm}$ is a reasonable value so that in the case of the most extreme negative cover-electrode potentials, there is still a sizable amount of electrons ending up in the area defined by d. For N_{gap} and N_d, all ionization electrons ending up at the walls of the wire ledges are considered to enter the gap between two ROCs or the active readout region, respectively. This is done to account for the side walls of the wire ledges charging up on short time scales in the real experiment, as both negative and positive charges may end up there until an equilibrium is established at which the collected net charge is zero. This effect is strongly dynamic and depends on many variables like the exact electric potentials and the interaction rate. Therefore, it is not included in the static Garfield simulations, which introduces an additional uncertainty when comparing the results of the simulations to measurements.

For each cover-electrode voltage configuration, 250000 electrons are simulated. They are distributed randomly in x over a range of 0.75 cm centered around one anode wire, which fully covers the range of three adjacent anode wires. As modified cover-electrode voltages affect the potentials in the areas relevant for N_{gap} and N_d differently, the range over which the electrons are distributed randomly in y is adjusted separately in simulations performed for N_{gap} and N_d, respectively. They are chosen such that for the most extreme cover-electrode potentials, a significant amount of electrons still ends up on top of the cover electrode or outside the active readout area defined by d. For calculations of N_{gap}, the electrons are distributed within an interval of $\pm 0.6\,\text{cm}$ around the center of the gap while for N_d, they are distributed between $0.7\,\text{cm} < |y| < 2\,\text{cm}$ on both sides of the gap. The systematic uncertainty introduced by the starting position of single electrons in x and y is negligible w.r.t. the dimensions of all elements of the TPC ROCs, as the number of total electrons is chosen accordingly.

The results of the electrostatic simulations are presented in Section 5.6.3 where they are also compared to measured data.

5.6.2 Measurements

Multiple special-run campaigns were performed during the course of Run 2 in order to study the local space-charge distortions as a function of the cover-electrode voltage. These measurements cover periods when the TPC was filled with Ar-CO_2 (2015–2016, 2018) and Ne-CO_2-N_2 (2017), respectively. Here, the potentials at the cover electrodes of the IROCs were adjusted and data with the modified cover-voltage settings were collected, providing the measurement of the space-charge distortions. In Section 5.6.3, the distortions with modified cover-electrode voltages are then compared to those measured with nominal settings in the same way as it is done in Section 5.4. The correlation between the space-charge distortions with modified settings and those with nominal settings is drawn for the corresponding sector boundaries $\pm$ 0.5 sectors in the IROCs and for $|z/x| < 0.2$. Fitting the correlation with a polynomial of first order, the slope corresponds to the relative size of the space-charge distortions with the modified voltage configuration.

In a first scan during the p−Pb run at the end of 2016, the cover-electrode voltage was varied between 0 V and −240 V in steps of −60 V. The purpose of these data was to demonstrate that the space-charge distortions could be mitigated by a modification of the potential at the cover electrodes. The data were taken with nominal positive $\boldsymbol{B}$-field and at an interaction rate of about 200 kHz which is equivalent to 534 kHz in pp collisions in terms of expected space-charge density. At the time of the measurements, the TPC was filled with Ar-CO_2. No dedicated reference runs without space-charge distortions were taken with the corresponding cover-electrode voltages at low interaction rate, which means that the distortions from the reference run with the nominal voltage of −180 V is subtracted in order to account for static distortions. Therefore, the static distortions close to the cover electrodes during the scan and those in the reference run are mismatched. As additional static distortions of the order of a few mm are expected for modified cover-electrode voltages (Fig. 5.32), this discrepancy is small compared to the size of the local space-charge distortions of up to several cm and it is acceptable for the purpose of proving the principle.

Towards the end of 2017, further special runs were taken with Ne-CO_2-N_2, nominal negative magnetic field and at about 1100 kHz interaction rate. By then, modifications of the hardware have been conducted by the hardware experts, allowing to independently power adjacent cover electrodes and to also apply positive potentials. This change was required to apply a potential difference ΔV_{cover} between two adjacent cover electrodes. In this scan, the cover-electrode voltages were set to $V_{\text{cover}} = 0 \mp 180\,\text{V}$, resulting in $V_{\text{cover1}} = -180\,\text{V}$ and $V_{\text{cover2}} = +180\,\text{V}$. Reference runs at low interaction rate (30 kHz) both with nominal and modified cover-electrode potentials were recorded right before to study and subtract the modified static distortions. Another run at 1100 kHz with $V_{\text{cover}} = 0$ is taken for comparison to the first scan from 2016.

The plan for 2018 was to find the final configuration for the cover electrodes in order to mitigate the local space-charge distortions as much as possible. Therefore, two more scans were performed to extend the range of cover-electrode voltages covered by the first scans. The data were taken with negative $\boldsymbol{B}$-field and with an Ar-CO_2 gas mixture. For each setting of cover-electrode potentials, one run at high interaction rate of about 1100 kHz is taken to measure the space-charge distortions and another run is taken at low interaction rate of 15 kHz as a reference for static distortions, specifically to account for these close to the cover electrodes. Dedicated runs with the nominal detector configuration were also included in the scans for comparison. The same cover-electrode potentials as in the scan of 2017 were used but covering both polarities of ΔV_{cover}. In addition, five more settings are studied, applying $V_{\text{cover}} = V_{\text{cover,offset}} \mp \Delta V_{\text{cover}}$ of +120 V

$V_{\text{cover,offset}}$	ΔV_{cover}	V_{cover1}	V_{cover2}	Year	$\boldsymbol{B}$-field	Coll. sys.	IR (kHz)
0	0	0	0	2016	++	p−Pb	200
-60 V	0	-60 V	-60 V	2016	++	p−Pb	200
-120 V	0	-120 V	-120 V	2016	++	p−Pb	200
-180 V*	0*	-180 V*	-180 V*	2016	++	p−Pb	200
-240 V	0	-240 V	-240 V	2016	++	p−Pb	200
-180 V*	0*	-180 V*	-180 V*	2017	−−	pp	30
0	∓180 V	-180 V	+180 V	2017	−−	pp	30, 1100
0	0	0	0	2017	−−	pp	1100
-180 V*	0*	-180 V*	-180 V*	2018	−−	pp	15, 1100
0	∓180 V	-180 V	+180 V	2018	−−	pp	15, 1100
0	±180 V	+180 V	-180 V	2018	−−	pp	15, 1100
+60 V	∓120 V	-60 V	+180 V	2018	−−	pp	15, 1100
+120 V	∓60 V	+60 V	+180 V	2018	−−	pp	15, 1100
0	0	0	0	2018	−−	pp	15, 1100
+90 V	0	+90 V	+90 V	2018	−−	pp	15, 1100
+180 V	0	+180 V	+180 V	2018	−−	pp	15, 1100

Table 5.2: A list of cover-electrode voltage configurations which were used during several scans in Run 2, together with additional information about the running conditions. The nominal settings are marked with an asterisk (*). A Ne-CO_2-N_2 gas mixture was used in 2017 while Ar-CO_2 was used in 2016 and 2018.

$\mp$ 60 V and +60 V $\mp$ 120 V as well as increasing $V_{\text{cover,offset}}$ from 0 to +180 V in steps of 90 V. A list of the cover-electrode voltage settings used in all of the scans together with additional information is provided in Table 5.2. After defining the final configuration which works best to mitigate the local space-charge distortions, a dedicated interaction-rate scan was performed, increasing the interaction rate from 30 kHz up to 1100 kHz in six steps.

5.6.3 Results

The drift lines of ionization electrons calculated by Garfield for cover-electrode voltages between −360 V and 0 and $\Delta V_{\text{cover}} = 0$ are illustrated in Fig. 5.33. Drift lines for the nominal voltage of −180 V are shown in Fig. 5.32. As the nominal voltage matches the drift field and minimizes static distortions at the chamber boundaries, any deviation from the nominal deflects the drift lines from a straight path. This effect is observed in the drift-line plots. A more positive voltage attracts the ionization electrons towards the cover electrode. As a result, less electrons drift into the gap between two ROCs as they end up on either of the two cover electrodes. At the other side of the wire ledge, i.e. at the edge of the active readout area, electrons close to the wire ledge end up on top of the cover electrode, which leads to a loss of ionization and effectively larger dead zones. In the experiment, this would be reflected by losses of the cluster charge or even fully lost clusters. Electrons further away are deflected towards the wire ledge and might still end up inside the active readout area with distorted end points. Decreasing the voltage further towards more negative values, the opposite effect is observed. More electrons enter the region of the gap between the two chambers. On the edge of the active readout area, electrons are pushed away from the wire ledge, distorting their measured arrival points. In addition, ionization which usually would end up on top of the cover electrode, and escape detection, is deflected inside the active area. In case of significantly more negative potentials, e.g. −360 V, the electrons are deflected by so much that the geometrical active area starts to decrease as no ionization ends up close to the wire ledge.

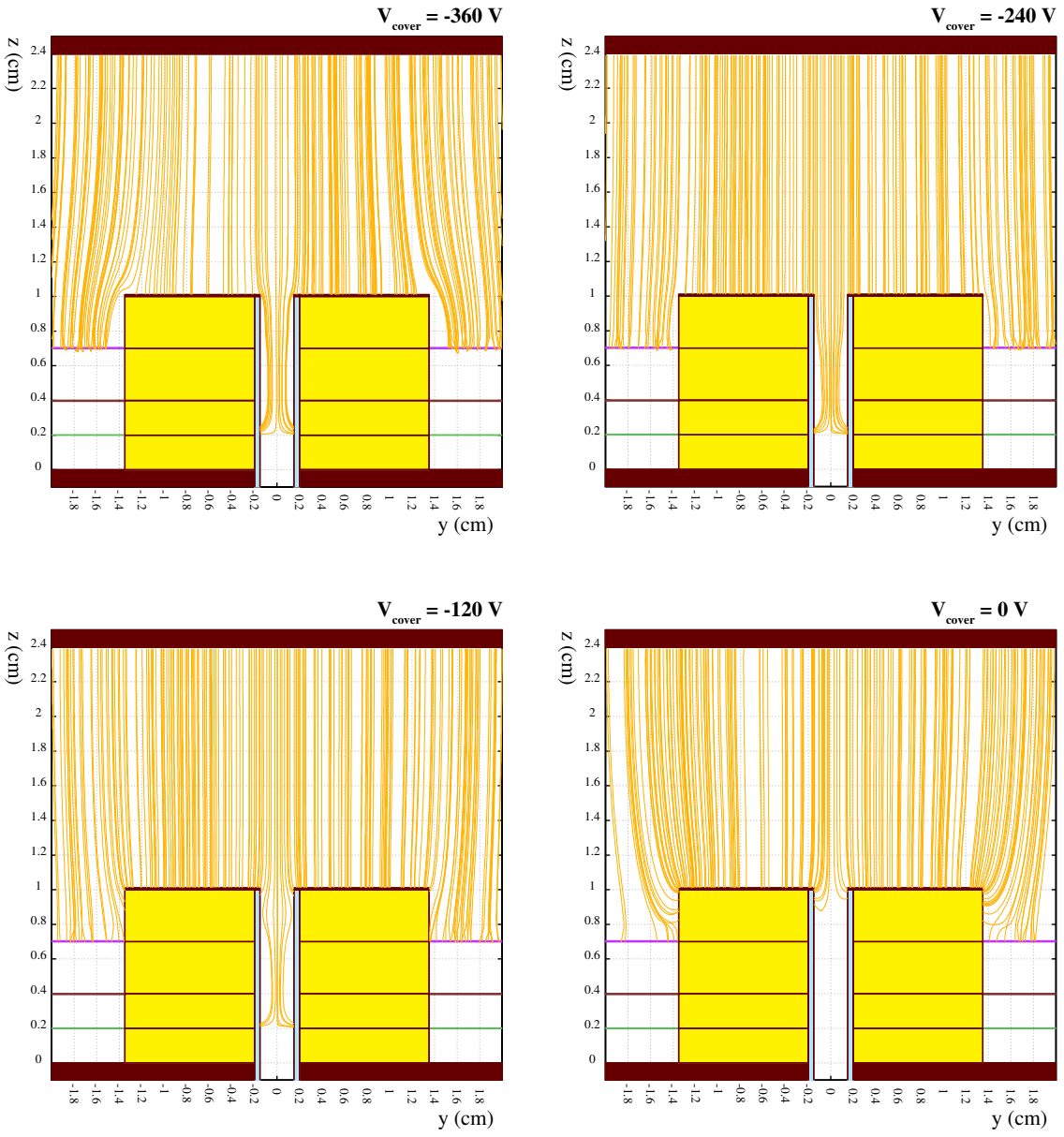

Figure 5.33: The drift lines of ionization electrons (orange lines) calculated by Garfield for four different cover-electrode voltages V_{cover}. The potential difference between the two adjacent cover electrodes ΔV_{cover} is kept at 0. The values of V_{cover} are quoted in the legends of the plots. They are gradually increased from $-360\,\text{V}$ (*top left*) to $-240\,\text{V}$ (*top right*) to $-120\,\text{V}$ (*bottom left*) to 0 (*bottom right*). The electron drift lines with nominal cover-electrode potential of $-180\,\text{V}$ are shown in the left plot of Fig. 5.32. All simulations are performed with a magnetic field of $\boldsymbol{B} = 0.5\,\text{T}$ along the drift direction and nominal voltages of the closed GG ($V_{\text{G}} = $ -70 V and $\Delta V = \pm 90\,\text{V}$).

The relative amount of drift lines, compared to nominal settings, ending both in the gap between two chambers (N_{gap}) and close to the wire ledge at the edge of the active readout area ($N_{d=5}$) are calculated for cover-electrode voltages between $-360\,\text{V}$ and 0. As an additional parameter, the offset voltage of the GG (V_{G}) is decreased from the nominal value of $-70\,\text{V}$ to $-150\,\text{V}$ in steps of $-20\,\text{V}$ for each cover-electrode voltage. The results are shown in Fig. 5.34. A linear trend is observed for N_{gap} as it decreases from 1.7

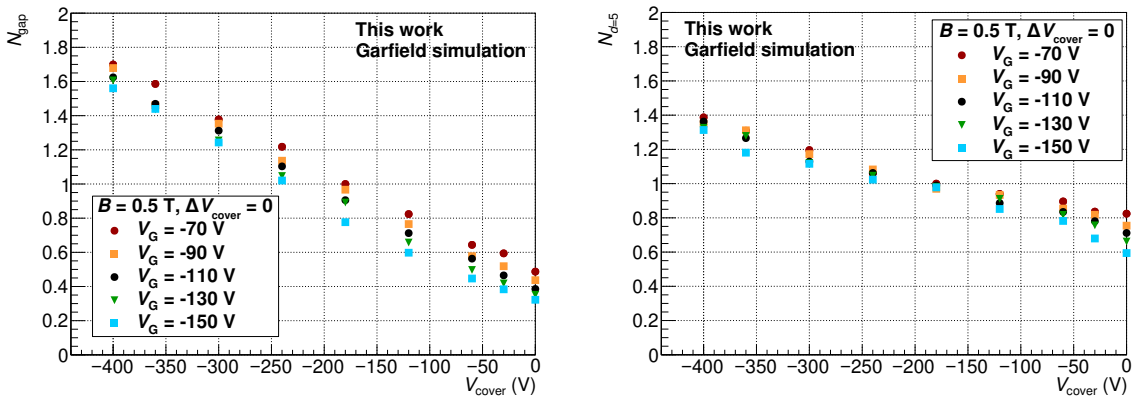

Figure 5.34: The relative amount of electron drift lines in Garfield simulations ending up inside the gap between two ROCs (N_{gap}, *left*) and at the edge of the active readout area of one ROC ($N_{d=5}$, *right*). The results are shown as a function of the cover-electrode voltage V_{cover} for $\Delta V_{\mathrm{cover}} = 0$ and for different offset voltages of the GG (V_{G}). The Garfield simulations are performed with a closed GG ($\Delta V = -90\,\mathrm{V}$) and a magnetic field $\boldsymbol{B}$ of 0.5 T along the drift direction.

at $-400\,\mathrm{V}$ down to 0.5 at 0 V, both at nominal V_{G}. A change of the GG offset voltage to more negative values globally shifts the potential in the volume of the simulated cell, leading to more field lines ending at the cover electrodes. In the Garfield simulations, this effect is also observed in-between two ROCs as the potential of the GG wires partially penetrates the dielectric layer between the gas volume and the wire ledge. Therefore, N_{gap} systematically decreases with more negative V_{G}. The results for $N_{d=5}$ provide similar trends with two key differences. It also systematically decreases with more positive cover-electrode voltage and more negative GG offset voltage. However, there are deviations from a linear dependence, especially towards to most negative ($-400\,\mathrm{V}$) and most positive (0 V) values. The problem at the edge of the active readout area is slightly more complicated than at the gap. It is open towards both sides of the edge as, for example at $V_{\mathrm{cover}} = 0$, more drift lines are ending on top of the cover electrode but there are also electrons from further away being pulled inside the region of interest defined by d. Moreover, the slope of $N_{d=5}$ is smaller by a factor of two compared to the one of N_{gap}, decreasing from 1.4 down to 0.8 over the range of simulated cover-electrode voltages at nominal V_{G}. According to these results of the Garfield simulations, the local space-charge distortions in the TPC are expected to decrease with more positive potentials at the cover electrodes. The amount by which the distortions decrease can give further indications whether the positive ions are created inside the gap between two ROCs or at the edge of the active area of one ROC.

The first cover-electrode voltage scan of the detector was performed during p−Pb collisions at 200 kHz interaction rate in 2016 while the TPC was filled with Ar-CO_2. According to the expectations from the Garfield simulations, the voltage at the cover electrodes of the detector was evenly varied between $-240\,\mathrm{V}$ and 0. The measured local space-charge distortions $\mathrm{d}r\varphi$ in a run with a given setting are then correlated to those obtained with nominal settings, selecting the data from the IROCs of the six most critical sectors, 2, 4, 6, 9, 20 and 30, ± 0.5 sectors around the given sector boundary, respectively, and $|z/x| < 0.2$. The slope of the linear correlation indicates the relative size of the distortions compared to nominal conditions. The results are summarized in Fig. 5.35, showing the relative space-charge distortions as a function of the

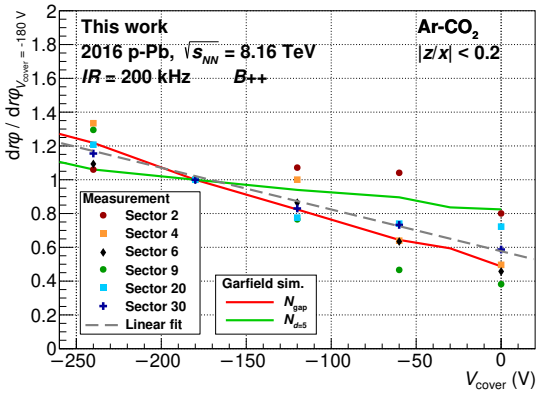

Figure 5.35: The space-charge distortions measured at different cover-electrode voltages relative to those at nominal voltages ($dr\varphi/dr\varphi_{V_{\mathrm{cover}}=-180\,\mathrm{V}}$) as a function of the cover-electrode voltage V_{cover}. Data at different sector boundaries ± 0.5 sectors and at $|z/x| < 0.2$ are shown with full colored markers. A linear fit of the data is shown by the gray dashed line. The solid lines represent results from Garfield simulations for N_{gap} (*red*) and $N_{d=5}$ (*green*) at nominal GG voltages.

cover-electrode voltage. The data points at a given V_{cover} have a significant spread, emphasizing the slightly different characteristics and dependencies of the effect at each individual sector which were already observed in studies of the interaction-rate dependence and the fluctuations. In addition, significant local fluctuations can bias single measurements which is suspected partly in the case of sectors 2 and 4. Taking all these uncertainties into account, a general trend is still observed as the space-charge distortions continuously decrease with more positive cover-electrode voltage. A linear fit of all data points is performed to visualize this behavior. Averaged over all data, the distortions decrease by more than 40 % when increasing V_{cover} to 0. In Fig. 5.35, the results from this measurement are also compared to results from Garfield simulations. The data are well in agreement with results for N_{gap}, for which the absolute slope is 24 % larger than in the data. Although $N_{d=5}$ also predicts decreasing space-charge distortions with more positive V_{cover}, the absolute slope is smaller by more than a factor two compared to the data. Taking into account the studies described in Section 5.5, these results strongly favor the scenario in which the space charge is produced inside the gap between two ROCs by gas amplification of primary and secondary ionization. A more positive cover-electrode voltage deflects a fraction of the ionization away from the gap, effectively reducing the total amount of charge which is amplified at the anode wires.

Apart from changing the cover-electrode offset voltage, a potential difference ($\Delta V_{\mathrm{cover}}$) between two adjacent cover electrodes is also studied in Garfield simulations and with the detector. The left plot of Fig. 5.36 illustrates the drift lines of electrons for $V_{\mathrm{cover}} = 0 \mp 180\,\mathrm{V}$. Using such a high $\Delta V_{\mathrm{cover}}$ in this static scenario, the electrons starting at one side of the gap are pulled across the gap to end up on the other cover electrode. N_{gap} is calculated for various values of $\Delta V_{\mathrm{cover}}$ and for $V_{\mathrm{cover,offset}}$ of $-60\,\mathrm{V}$, 0 and $+60\,\mathrm{V}$. The results are shown in the right plot of Fig. 5.36. As observed in the previous simulations and measurements, N_{gap} decreases with more positive $V_{\mathrm{cover,offset}}$ for all $\Delta V_{\mathrm{cover}}$. However, N_{gap} first increases with increasing $\Delta V_{\mathrm{cover}}$ up until around $\Delta V_{\mathrm{cover}} = 90\,\mathrm{V}$ as the fraction of drift lines deflected into the gap from one side is slightly higher than the fraction deflected out of the gap onto the cover electrode on the other side. Only when the potential difference between the cover electrodes is sufficiently large such that the electrons on one side of the gap are deflected across the full width of the gap towards the cover electrode on the other side, N_{gap} starts to decrease. For values $\Delta V_{\mathrm{cover}} > 100\,\mathrm{V}$,

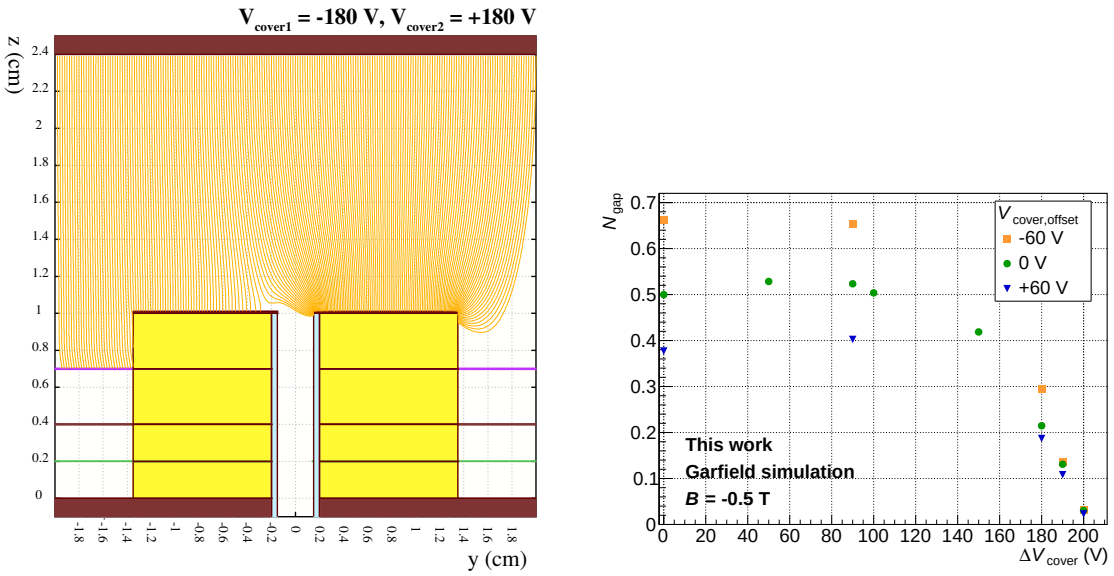

Figure 5.36: *Left:* Drift lines of electrons calculated by Garfield for a cover-electrode voltage of $V_{\text{cover}} = 0 \mp 180\,\text{V}$. *Right:* The fraction of ionization electrons entering the gap between two ROCs relative to the fraction with nominal voltage settings (N_{gap}) as a function of ΔV_{cover}, obtained from Garfield simulations. The results for three different values of $V_{\text{cover,offset}}$ are shown with different marker colors.

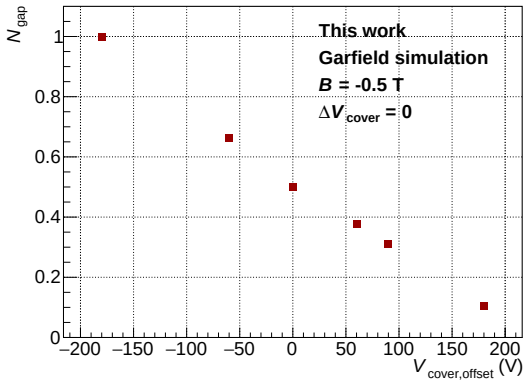

Figure 5.37: Results of Garfield simulations for the fraction of ionization electrons entering the gap between two ROCs relative to the fraction with nominal voltage settings (N_{gap}) as a function of $V_{\text{cover,offset}}$ for $\Delta V_{\text{cover}} = 0$.

N_{gap} decreases with the square of ΔV_{cover} down to 2% at $\Delta V_{\text{cover}} = 200\,\text{V}$ for all $V_{\text{cover,offset}}$, implying that the value of $V_{\text{cover,offset}}$ becomes negligible at sufficiently high ΔV_{cover}. Further simulations are performed to extend the range of cover-electrode potentials to positive values at zero ΔV_{cover}. The results of those are presented in Fig. 5.37. Following the linear dependence observed in Fig. 5.34, N_{gap} decreases to almost 10 % at $V_{\text{cover}} = +180\,\text{V}$. Both simulations with a potential difference between adjacent cover electrodes as well as simulations with positive cover-electrode potentials provide a promising outlook on ways to mitigate the local space-charge distortions by possibly one order of magnitude. In the following paragraphs, the results obtained in simulations are compared to corresponding measurements performed in 2017 and 2018.

First measurements of the local space-charge distortions with $\Delta V_{\text{cover}} = \mp 180\,\text{V}$ were performed in 2017, when the detector was filled with Ne-CO_2-N_2, at interaction rates

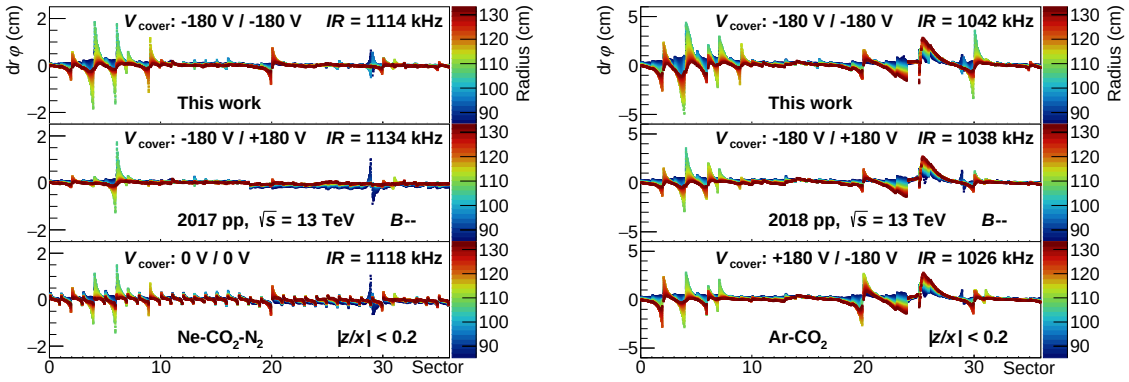

Figure 5.38: *Left plot:* The measured space-charge distortions (d$r\varphi$) as a function of the sector and the radius for the nominal cover-electrode settings (V_{cover}: -180 V / -180 V, *top*), for V_{cover}: -180 V / +180 V (*middle*) and for $V_{\text{cover}} = 0$ (*bottom*). The measurements were taken with Ne-CO_2-N_2 at interaction rates around 1100 kHz and with negative $\boldsymbol{B}$-field. Data at $|z/x| < 0.2$ are selected. *Right plot:* The measured space-charge distortions (d$r\varphi$) as a function of the sector and the radius for the nominal cover-electrode settings (V_{cover}: -180 V / -180 V, *top*), for $V_{\text{cover}} = 0 \mp 180$ V (*middle*) and for $V_{\text{cover}} = 0 \pm 180$ V (*bottom*). The data were taken with Ar-CO_2 at interaction rate of about 1100 kHz with nominal negative $\boldsymbol{B}$-field. The region in the TPC of $|z/x| < 0.2$ is selected.

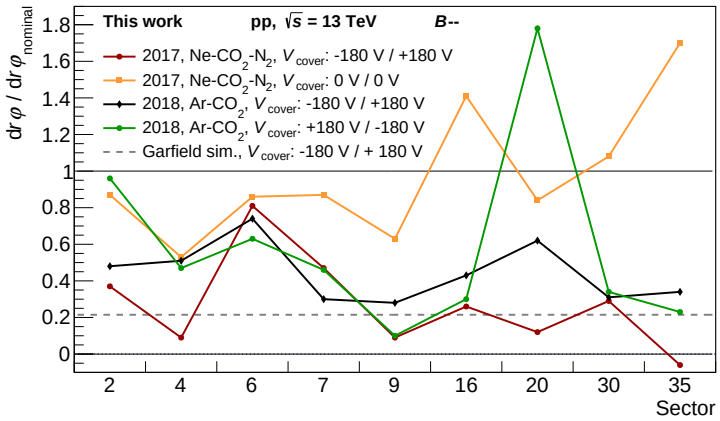

Figure 5.39: The relative space-charge distortions with a given cover-electrode voltage configuration (represented by the markers in with different colors), compared to the nominal scenario, as a function of the sector. The data shows the scans with $\Delta V_{\text{cover}} = 180$ V with both polarities, taken with Ne-CO_2-N_2 and Ar-CO_2 at interaction rates around 1100 kHz. The result from the Garfield simulation is drawn by the gray dashed line.

around 1100 kHz. A dedicated run with nominal settings for reference as well as a run with $V_{\text{cover}} = 0$ for comparison to previous measurements in 2016 were taken. The measured space-charge distortions in all three runs are shown in the left plot of Fig. 5.38 as a function of the sector and the radius. Applying the potential difference between adjacent cover electrodes, the size of the distortions decreases significantly as predicted by Garfield simulations. At sector 6 however, an inconsistency is observed with respect to the other sectors, as barely any improvement is achieved. This suggests that, in contrast to the static scenario assumed in the Garfield simulations, the results in the real detector are strongly dependent on the dynamics of the back-drifting positive ions, which is individual at each sector boundary. The measurements were taken again in 2018 with

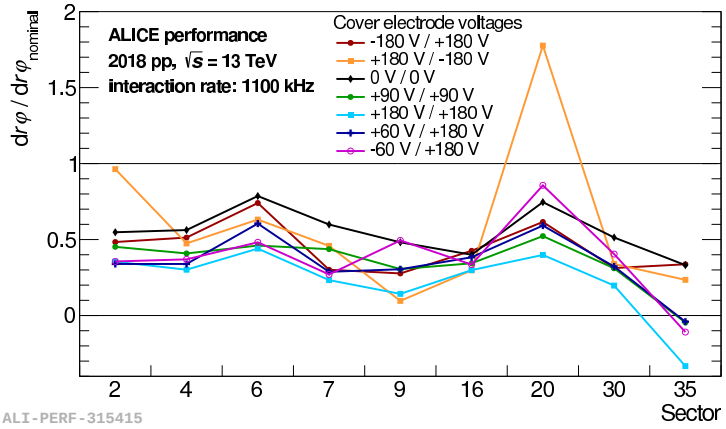

Figure 5.40: The space-charge distortions for a given cover-electrode voltage configuration relative to those with nominal settings as a function of the sector. The markers with different colors represent the different cover-electrode settings, including both settings with zero and non-zero ΔV_{cover} at different $V_{\text{cover,offset}}$. The data were taken with Ar-CO_2 at interaction rates of about 1100 kHz.

Ar-CO_2, applying $\Delta V_{\text{cover}} = 180\,\text{V}$ with both polarities ($\mp$ and $\pm$). The space-charge distortions in these runs are drawn as a function of the sector and radius in the right plot of Fig. 5.38. A summary of the measurements of 2017 and 2018 with $\Delta V_{\text{cover}} = 180\,\text{V}$ is presented in Fig. 5.39. It shows the measured distortions for a given cover-electrode voltage relative to those with nominal settings for each sector boundary which is affected. The expectation obtained by the Garfield simulation is also included in the plot. The result for $V_{\text{cover}} = 0$ with Ne-CO_2-N_2 is consistent with previous measurements from 2016 with Ar-CO_2 in Fig. 5.35. For $\Delta V_{\text{cover}} = 180\,\text{V}$, the data with Ne-$CO_2$-$N_2$ is close to the Garfield simulation except for sector 6. The results with Ar-CO_2 with the same settings are similar to those with Ne-CO_2-N_2 although they are systematically above the neon data. Changing the polarity of ΔV leads to no further systematic decrease of the distortions. Instead, the distortions at sectors 2 and 20 significantly increase again. This confirms the observations of the measurements with Ne-CO_2-N_2 as no consistent improvement can be achieved for all sectors at once applying non-zero ΔV. With the particular configuration of $\Delta V_{\text{cover}} = 180\,\text{V}$, the $\boldsymbol{E}$-field at only one of the cover electrodes differs from the nominal scenario. As the cloud of positive ions emerging from the gap into the drift volume adds an additional contribution to the $\boldsymbol{E}$-field, the effect seen in the static case of the Garfield simulation is diminished by different amounts depending on the individual sector. The space-charge density with Ar-CO_2 is significantly higher compared to that with Ne-CO_2-N_2 at the same interaction rate, therefore the contribution from space charge to the $\boldsymbol{E}$-field is larger and the cover-electrode settings with non-zero ΔV are relatively less effective with Ar-CO_2. Following these results, more measurements with different combinations of $V_{\text{cover,offset}}$ and ΔV_{cover} were taken at an interaction rate around 1100 kHz as well as points with zero ΔV_{cover} and $V_{\text{cover,offset}}$ up to $+180\,\text{V}$. Fig. 5.40 shows the relative space-charge distortions in these scans as a function of the sector. In general, the sector-by-sector trend is almost always consistent between all cover-electrode configurations, with a few occasional exceptions. It becomes clear that the variations of the improvement between the sectors are visibly smaller for cover-electrode settings with zero ΔV_{cover} while for non-zero ΔV_{cover}, the results may significantly deviate for single sectors compared to the global trend. Some data points at sector 35 are below zero because the space-charge distortions disappear or become negligible w.r.t. to time-dependent charge-up effects. The relative decrease of the space-charge distortions averaged over all sectors for each setting from Fig. 5.40 is tabulated in Table 5.3. For the calculation of the average, a

$V_{\text{cover,offset}}$	ΔV_{cover}	V_{cover1}	V_{cover2}	$\langle \mathrm{d}r\varphi/\mathrm{d}r\varphi_{\text{nominal}} \rangle_{\text{sector}}$
0	$\mp$180 V	-180 V	+180 V	0.408
0	$\pm$180 V	+180 V	-180 V	0.437
120 V	$\mp$60 V	+60 V	+180 V	0.397
60 V	$\mp$120 V	-60 V	+180 V	0.446
0	0	0	0	0.523
+90 V	0	+90 V	+90 V	0.405
+180 V	0	+180 V	+180 V	0.296

Table 5.3: The relative space-charge distortions measured for each cover-electrode voltage configuration from Fig. 5.40, averaged over all sectors using a robust LTS regression with a fraction of good points of 0.95.

robust least trimmed squares (LTS) regression with a fraction of good points of 0.95 is used in order to be less sensitive to large variations for single sectors at a given cover-electrode voltage configuration. While for the settings with non-zero ΔV_{cover} the distortions on average decrease to about 40 %, the results for zero ΔV_{cover} and increasing $V_{\text{cover,offset}}$ confirm the systematic trend which is observed in Fig. 5.35. Applying +180 V on all cover electrodes, the space-charge distortions on average decrease below 30 %. This is still significantly larger than the prediction of the Garfield simulation (Fig. 5.37) which is close to 10 %. Nonetheless of all configurations, $V_{\text{cover}} = +180\,\text{V} \pm 0$ yields the best and most robust improvement in terms of the size of the local space-charge distortions for all sectors which are affected. Therefore, this parameter was selected as the new nominal voltage for the cover electrodes of all IROCs for the rest of 2018 including the final Pb−Pb data-taking period of Run 2.

5.7 Floating Gating Grid Wires in OROC C06

The potential at a GG wire can be undefined in the rare event that the connection between the wire and the power supply is cut, e.g. a broken soldering point. Cases of floating GG wires exist in the OROCs of sectors 13 (OROC A13) and 19 (OROC C01). As the floating wire charges up to the nominal drift potential during operation, the closed GG is partially transparent for charges in that narrow region and a fraction of the amplification ions enters the drift volume where they cause space-charge distortions. The amount of leaking ions can be mitigated by choosing the preferred polarity of ΔV such that the two adjacent GG wires are biased with a negative potential. This way, most of the amplification ions are neutralized and the effect of space-charge distortions due to the floating GG wire are minimized. A more serious situation is observed in the OROC of sector 24 (OROC C06) where two adjacent GG wires are floating. In this case, the reversal of the ΔV-polarity is ineffective as there is no preferred polarity. The space-charge distortions observed around OROC C06 in 2015 Pb−Pb data at 7.5 kHz interaction rate are shown in Fig. 5.41. They reach up to 8 cm both for $\mathrm{d}r\varphi$ and $\mathrm{d}r$ in OROC C06 and they are also significant in the readout chambers of the adjacent sectors, reaching several cm. As the tracking and PID resolutions and efficiencies are affected by large space-charge distortions in such a large region of the TPC, the possibilities to minimize the amount of back-drifting ions due to the floating GG wires are investigated.

The source of the observed distortions, which is ion backflow from the amplification region, is well understood. The total space-charge density depends on the amount of primary ionization per time interval which is proportional to the interaction rate. At a fixed interaction rate, the number of amplification ions created at the anode wires depends on the gain. The fraction of amplification ions drifting back into the TPC drift volume (ion backflow), as well as the gain, is determined by the electric field

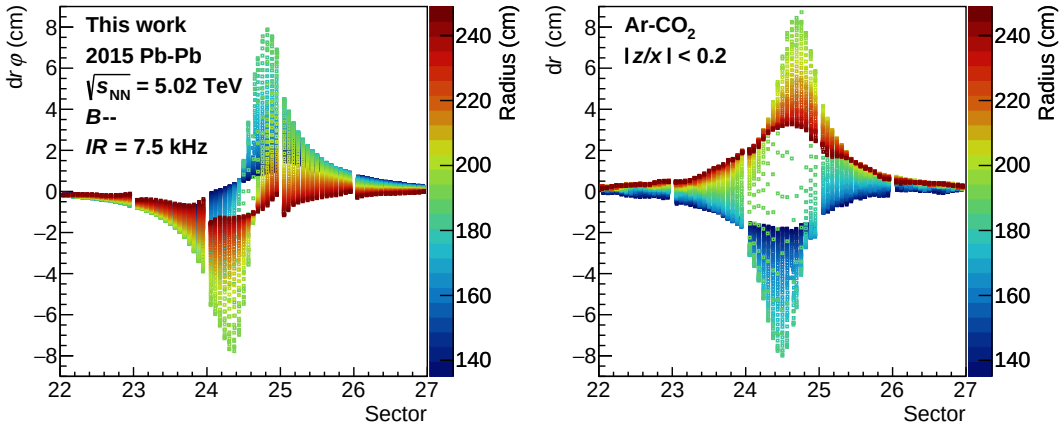

Figure 5.41: The measured space-point distortions d$r\varphi$ (*left*) and dr (*right*) around OROC C06 due to ion backflow, caused by two adjacent floating GG wires, as a function of the sector and the radius for $|z/x| < 0.2$. The data were taken with Ar-CO_2 during Pb−Pb collisions at 7.5 kHz interaction rate in 2015.

configuration defined by the wires, wire potentials and wire geometry. While the potentials at the two floating GG wires of OROC C06 are undefined, the electric field can still be manipulated by the potentials at the adjacent GG wires. Therefore, the space-charge density in OROC C06 can be changed by three parameters which are controlled by the detector: the anode high-voltage and the GG voltages V_{G} and ΔV. In the following, the space-charge distortions are studied as a function of two of these parameters, the anode high-voltage and ΔV.

The high voltage at the anode wires of OROC C06 was decreased in a scan of six consecutive runs during pp collisions taken at an interaction rate of about 850 MHz in 2018 while the TPC was filled with Ar-CO_2. Starting at the nominal voltage of 1589 V, it was decreased by 10 V at each step down to a voltage of 50 V below the nominal, at which the gain corresponds to 67 % of the nominal gain [76]. The space-charge distortions in OROCs C05, C06 and C07 at reduced high voltage in OROC C06 are compared to the ones at nominal voltage, performing a linear fit of their correlation and quantifying the decrease of the distortions by the slope of the fit function. The results are shown as a function of the difference to the nominal voltage ΔHV in Fig. 5.42 for azimuthal and radial space-charge distortions at $|z/x| < 0.2$. An exponential increase of the distortions with the high voltage at the anode wires is observed. They decrease down to 47 % at $\Delta\mathrm{HV} = -50$ V which is significantly more than expected from the lower gain. Assuming that the ion backflow at the two floating GG wires stays constant with decreased anode high-voltage, the exponential dependence as a function of ΔHV has two contributions. As the gain increases exponentially with the voltage, the amount of total amplification ions also increases correspondingly. In addition, the amount of primary ionization which is amplified in that specific region also increases with the size and the extent of the space-charge distortions as the electrons are deflected towards the region of the floating GG wires, similarly as for the local space-charge distortions observed in the IROCs. While a decrease of the distortions by more than a factor two is a significant improvement, the lower gain (67 % of the nominal) can lead to a higher sensitivity to threshold effects and to an efficiency loss of found clusters. At $\Delta\mathrm{HV} = -50$ V, the fraction of missing clusters for minimum-ionizing particles increases from 5 % for all sectors on the C side to 12 % in sector 24 [77]. This is very well acceptable considering that it affects only a small fraction of the total detector volume and, therefore, has a minor implication for the overall tracking performance. In contrast, the improvement in cluster resolution and tracking efficiency achieved by decreasing the space-charge

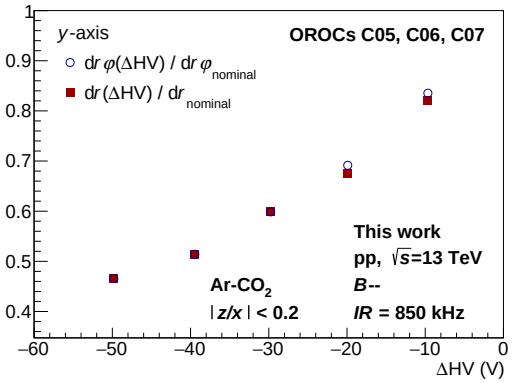

Figure 5.42: The measured space-charge distortions relative to those measured at nominal high voltage are shown on the y-axis as a function of the difference to the nominal high voltage ΔHV. The azimuthal distortions d$r\varphi$ and the radial distortions dr are represented by the open blue markers and the full red markers, respectively. Data in the OROCs of sectors 23, 24 and 25 (C05, C06, C07) at $|z/x| < 0.2$ are analyzed. They were taken during pp collisions at 850 kHz interaction rate and at nominal negative $\boldsymbol{B}$-field while the TPC was filled with Ar-CO_2.

distortions and the volume which is affected by them is much more significant.

The nominal bi-polar bias potential ΔV of ± 90 V is applied to the GG wires in order to keep the positive amplification ions from drifting into the TPC drift volume. In the case of two adjacent floating GG wires, an increase of ΔV results in more ions being attracted by the negatively polarized wires in the direct vicinity of the floating ones. This observation is made in Pb−Pb data from 2015 where the ΔV was increased to 110 V and 120 V to study the effect on the space-charge distortions in the IROCs (Section 5.4.2). The left plot of Fig. 5.43 shows the logarithm of the azimuthal distortions d$r\varphi$ in OROC C06 measured at $|z/x| < 0.2$ in the 2015 Pb−Pb data-taking period as a function of the median of the currents in the first layer (L0) of the TRD. Here, TRD L0 currents are used as a more robust estimator for the particle flux than the interaction rate and a value of 1.8 corresponds to a collision rate of 8 kHz. The dependence of a localized space-charge density and the resulting distortions on the particle flux is discussed in Section 5.2.2. Data for three different values of ΔV are shown in the plot. The distortions decrease systematically when increasing ΔV. To quantify the effect independently of the interaction rate, a linear fit of the data of each ΔV setting is performed in the region of the exponential increase. The data is then compared to the fit of $\Delta V = 90$ V in the right plot of Fig. 5.43. It shows the average ratio between the data points and the fit as a function of ΔV. The statistical uncertainty is between 4 % and 6 % and it is limited by the number of runs, each data point in the left plot corresponding to one run. The distortions decrease to 79 % and 63 % at ΔV of 110 V and 120 V, respectively. These results are validated by a dedicated scan during pp collisions at 750 kHz interaction rate in 2018. The TPC gas was Ar-CO_2 and it is the same as in 2015. This scan was already performed with new settings of decreased anode high-voltage (50 V below the nominal) in OROC C06, mitigating the space-charge distortions by more than a factor two as discussed in the last paragraph. ΔV was increased to 105 V and 120 V in two consecutive runs. The correlation of the measured distortions d$r\varphi$ in OROC C06 at $|z/x| < 0.2$ between each scan and a reference run with nominal ΔV is shown in Fig. 5.44. The slope of linear fits to the data indicates the relative amount by which the distortions decrease at the given ΔV. The values of 86 % at $\Delta V = 105$ V and 66 % at $\Delta V = 120$ V are consistent with the observations in the 2015 Pb−Pb data. The combination of decreasing

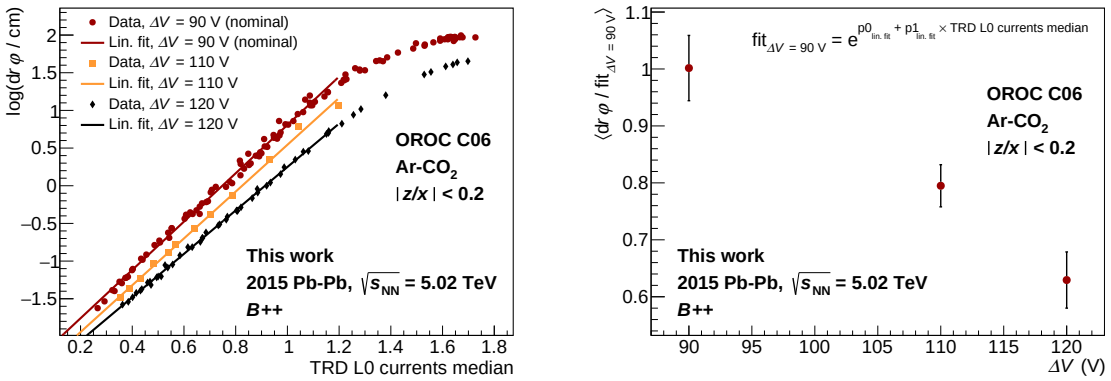

Figure 5.43: *Left:* The logarithm of the measured space-charge distortions d$r\varphi$, normalized to 1 cm, in OROC C06 as a function of the average currents in the first layer of the TRD (TRD L0 currents median) in Pb−Pb collisions of 2015 at nominal positive $\boldsymbol{B}$-field. Data at $|z/x| < 0.2$ are selected. The different colors of the markers distinguish between data with different ΔV settings of the GG wires in the OROCs. Linear fits of the data points are indicated by the solid lines. *Right:* The average ratio between the distortions in OROC C06 measured in data (d$r\varphi$) and the exponential fit of the data at $\Delta V = 90\,\mathrm{V}$ ($\mathrm{fit}_{\Delta V=90\mathrm{V}}$), using the fit parameters (p0, p1) obtained from the linear fit in the *left* plot, as a function of ΔV. The same data as in the *left* plot are selected.

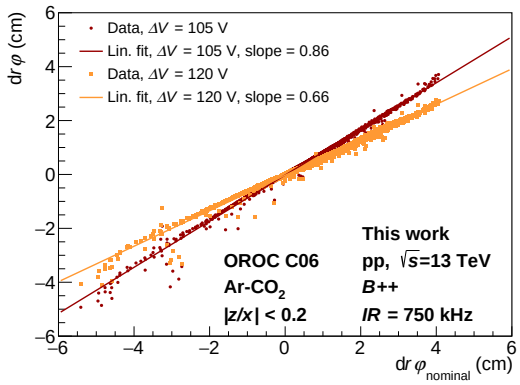

Figure 5.44: The correlation between measured space-charge distortions d$r\varphi$ in OROC C06 in runs with different ΔV, represented by markers in different colors, and the distortions $\mathrm{d}r\varphi_{\mathrm{nominal}}$ in a reference run at nominal ΔV of 90 V. The data are shown at $|z/x| < 0.2$ and they were taken during pp collisions at 750 kHz interaction rate at nominal positive magnetic field in 2018. A linear fit of the data is performed, indicated by the solid lines. The slope of the fit is quoted in the legend.

the high-voltage in OROC C06 by 50 V and increasing the ΔV of the GG in all OROCs by 30 V results in a mitigation of the space-charge distortions in OROC C06 by more than a factor of three, expecting a factor of 2.1 from the lower high-voltage and a factor 1.5 from the increased ΔV.

5.8 Final Mitigation

Thorough investigations and studies of the large local space-charge distortions in the IROCs and OROC C06 of the TPC were performed during LHC Run 2. The results and

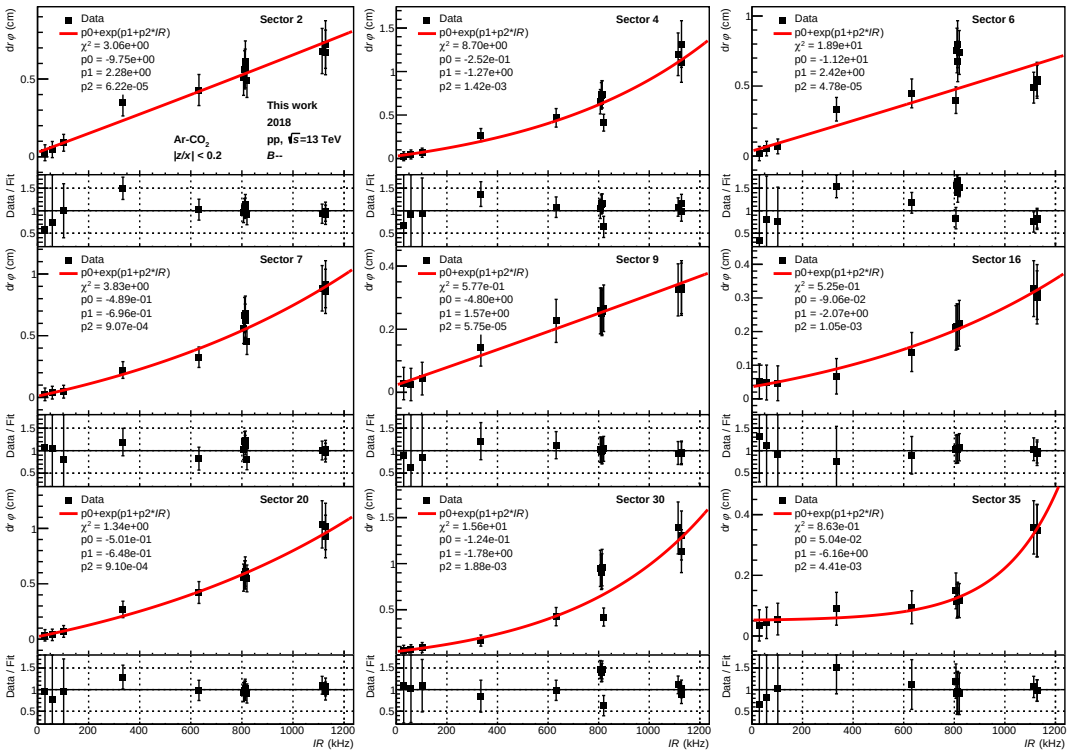

Figure 5.45: The measured space-charge distortions d$r\varphi$ with new cover-electrode voltage settings as a function of the interaction rate at different sector boundaries. The data were taken with nominal negative $\boldsymbol{B}$-field during pp collisions in 2018 while Ar-CO_2 was used as the TPC gas mixture. The full markers represent the data at $|z/x| < 0.2$. The error bars estimate uncertainties from cluster resolution, ITS-TRD-TOF track extrapolation and space-charge density fluctuations. An exponential fit is illustrated by the red line and the fit function and parameters are quoted in the legend. The ratio between the data points and the fit is plotted in the lower panel of each plot.

conclusions presented in this chapter provided an understanding of the mechanisms which led to the unexpected accumulation of space charge as well as solutions to mitigate the amount of space charge which is created at the ROCs in the first place.

The cover electrode voltage V_{cover} in all IROCs is changed from their nominal value of $-180\,\text{V}$, which matches the potential of the nominal drift field, to $+180\,\text{V}$. With this change, ionization electrons close to the edges of an IROC are deflected from their nominal path towards the cover electrode, i.e. the drift lines from the drift volume are deflected away from the 3 mm gap between two ROCs. As the space charge is created inside this gap by gas amplification at single or few anode wire tips sticking out at the outside edge of given IROCs, the decreased amount of ionization electrons entering the gap directly leads to a decrease of space-charge density and smaller local space-charge distortions. A dedicated scan was performed during pp collisions in 2018 to study the space-charge distortions with the new cover-electrode voltage settings as a function of the interaction rate and to compare them to those observed in previous scans with the old nominal settings (see Section 5.2.2). The results of the scan are shown in Fig. 5.45 which plots the measured space-charge distortions as a function of the interaction rate at the different sector boundaries. As previous measurements indicate a significant spread of the measurements at a constant interaction rate mostly due to space-charge density fluctuations, the uncertainty of the data points is estimated and visualized with vertical error bars. The total uncertainty is composed of a constant value of 0.01 cm for the

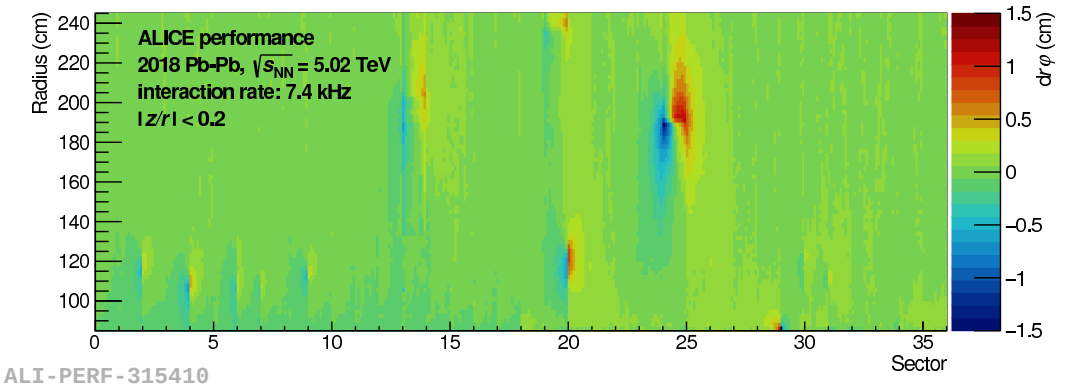

Figure 5.46: The measured space-charge distortions $\mathrm{d}r\varphi$ at $|z/x| < 0.2$ as a function of the sector and the radius. The data were taken during Pb−Pb collisions at an interaction rate of 7.4 kHz with nominal positive magnetic field. The TPC was filled with an Ar-CO_2 gas mixture.

cluster resolution, a constant extrapolation error of 0.05 cm of the ITS-TRD-TOF track segments used to measure the TPC space-point distortions, and an additional factor of 20 % of the measured space-charge distortions at given interaction rate to account for space-charge density fluctuations. The data are fitted with an exponential and the ratio between the data points and the fit are shown in the bottom panel of each plot. While in Pb−Pb data with nominal negative magnetic field and the old cover-electrode voltage settings the distortions are as large as 4 cm at some of the sector boundaries at 7.5 kHz interaction rate (Fig. 5.11), they decrease down to or even below 0.5 cm at all sectors at the corresponding pp interaction rate of about 700 kHz with the new cover-electrode voltage. At sectors 4, 7, 16, 20, 30 and 35, the exponential increase of the distortions with the interaction rate, which is expected for small amounts of space charge, becomes evident. The space-charge density with old cover-electrode voltage settings and Ar-CO_2 is substantially higher so that the exponential rise is exceeded and the dependence on the interaction rate transitions into a slow saturation.

In OROC C06, amplification ions leak through the GG into the TPC drift volume due to two adjacent floating GG wires. The effect was mitigated for the last Pb−Pb campaign of Run 2 at the end of 2018 by decreasing the high voltage of the anode wires in this particular ROC and by increasing the GG ΔV of the OROCs.

The final result of the mitigation strategies for the space-charge distortions in the IROCs and OROC C06 is demonstrated by Fig. 5.46. It shows the measurement of the space-charge distortions close to the CE in Pb−Pb data at 7.4 kHz interaction rate, taken in 2018 with nominal positive $\boldsymbol{B}$-field and with Ar-CO_2 as the TPC gas mixture. It can directly be compared to the Pb−Pb data shown in Fig. 5.6, which was taken in 2015. The improvement at the IROC sector boundaries is substantial as the space-charge distortions are of the order of 0.5 cm and slightly larger at sector 20. In OROC C06, they decrease from close to 6 cm to around 1 cm. As the scale of the space-charge distortions significantly decreased in Fig. 5.46, the effects of the other single floating GG wires in the OROCs of sectors 13 and 19 become visible in this representation. In addition to the maximum size of the space-charge distortions, it also becomes evident that the spatial extent of the different distortion spots significantly decreases after the mitigation. In the IROCs, instead of a range of two or more full sectors in some cases, the space charge only extends over a narrow region in φ. While, in any case, a large fraction of the TPC volume was unaffected by space charge before, the affected fraction is strongly decreased by the mitigation. Furthermore, the unexpected presence of large local space-charge

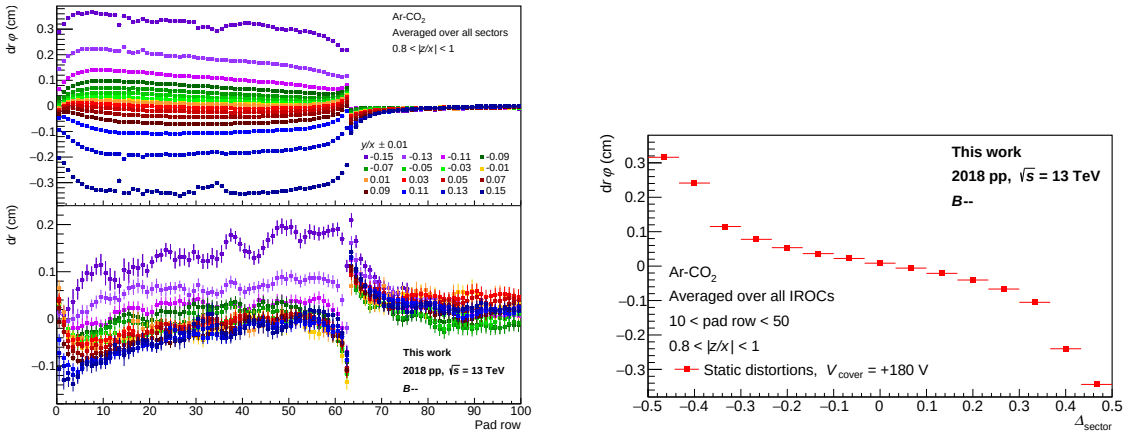

Figure 5.47: The static distortions introduced by changing the cover-electrode voltage from the nominal $-180\,\mathrm{V}$ to $+180\,\mathrm{V}$. *Left:* $\mathrm{d}r\varphi$ and $\mathrm{d}r$ averaged over all sectors as a function of the pad row and $|y/x|$ for data at $0.8 < |z/x| < 1.0$. *Right:* $\mathrm{d}r\varphi$ averaged over pad rows between 10 and 50 of all IROCs as a function of Δ_{sector} for data at $0.8 < |z/x| < 1.0$.

distortions pushed the early development of the calibration procedure initially planned for the Run 3 TPC upgrade and outlined in Section 4.6.1. Applying this calibration, the remaining space-point distortions are corrected and the initial space-point and tracklet resolution of the TPC of 200 µm are fully restored.

5.8.1 Static Distortions at the Sector Edges of IROCs

The modified cover-electrode potential chosen to mitigate the creation of space charge at the IROCs deviates from the potential of the nominal drift field by 360 V. The cover electrode fully surrounds the IROC by design. Consequently, distortions of the nominal drift field are expected in the region covered by the IROCs. The left plot of Fig. 5.47 shows the measured distortions $\mathrm{d}r\varphi$ and $\mathrm{d}r$ averaged over all sectors as a function of the pad row and $|y/x|$, where $|y/x| = 0$ and $|y/x| = 0.15$ correspond to the middle of a sector and the edge of a sector in azimuthal direction, respectively. The data were taken in pp collisions during the scan of cover-electrode voltages in 2018 (Section 5.6.2) at low interaction rate (15 kHz) to be unaffected by space-charge distortions. The distortions due to the changed cover-electrode potential are calculated by subtracting the measurement with the nominal value of $-180\,\mathrm{V}$ from the measurement with the modified value of $+180\,\mathrm{V}$. While the distortions in the OROCs at pad rows higher than 75 are close to zero, $|\mathrm{d}r\varphi|$ in the IROCs increases with the distance from the center of the chambers up to 0.36 cm at the edges. As a selection of $0.8 < |z/x| < 1.0$ is made on the data, the minor linear dependence on the pad row, which is observed in this representation, corresponds to a dependence on z rather than the radius. The azimuthal distortions also add a contribution to the radial distortions $\mathrm{d}r$ due to $\boldsymbol{E}\times\boldsymbol{B}$. At the radial boundaries of the IROCs, radial distortions of the order of 0.1 cm are observed because of the mismatch of potentials between the IROC cover electrodes and, respectively, the inner field cage (pad row = 0) and the OROC cover electrodes (pad row = 63). The right plot of Fig. 5.47 shows the distortions $\mathrm{d}r\varphi$ averaged over pad rows between 10 and 50 of all IROCs as a function of the distance to the azimuthal sector center Δ_{sector} expressed in units of one sector. The distortions around the center of the IROCs within an interval of $\Delta_{\mathrm{sector}} \pm 0.3$ are smaller than 0.1 cm. Towards the edges of the chamber, the distortions and the gradient of the distortions significantly increase. The static nature of these distortions, i.e. they are constant over time and free of fluctuations, and their absolute size of only around 0.3 cm allow to correct them while preserving the

initial TPC performance and resolution. However, several issues arise due to the increasing gradients towards the sector boundaries. First of all, the high gradients require sufficient azimuthal granularity during the extraction of the correction in order to not underestimate the correction due to averaging over a large range of distortions. Furthermore, transverse diffusion of primary and secondary ionization is strongly affected in the regions of the high gradients, effectively increasing the diffusion width and decreasing the maximum of the deposited charge. As a consequence, a fraction of charge is lost either as it ends up outside the active readout area or as it falls below the signal threshold. Cluster properties are directly affected, observing a decrease of the average total and maximum charge as well as the number of clusters in the regions of high distortion gradients compared to data with nominal cover-electrode voltage. While there is no possibility to correct these effects in the data, they are accounted for in Monte Carlo simulations to avoid biases in efficiency calculations.

6 Summary and Outlook

The gas mixture of the ALICE TPC was changed from Ne-CO_2 (90-10) to Ar-CO_2 (88-12) for the start of LHC Run 2 in order to assure even more stable and reliable operation of the ROCs. With the new gas mixture, large distortions of the measured space points were observed in small and localized regions of the TPC in high-luminosity data, which were not evident in Run 1 with Ne-CO_2 and at lower interaction rates. The work presented in this thesis was dedicated to investigating the origin of the unexpected space-point distortions, to understanding their differences between Run 1 and Run 2 operating conditions and to finding mitigation strategies which would decrease the size and the extent of the distortions as well as restore the intrinsic tracking performance of the TPC.

A newly implemented calibration procedure, originally foreseen for the upgrade of the TPC in LHC Run 3, provides the measurement of the space-point distortions in the TPC using the interpolation of external track segments from ITS, TRD and TOF and it allows to study the distortions as a function of numerous TPC and beam parameters. Two different effects are observed and studied independently. First, there are large distortions at the boundaries between certain IROCs, specifically at sector positions 2, 4, 6, 7, 9, 16, 20, 29, 30, 31 and 35, which are of the order of up to several cm at 7.5 kHz interaction rate in Pb−Pb collisions. These distortions appear only around certain radii which are different at each sector. Second, two adjacent floating GG wires in the OROC of sector 24 make the GG locally inefficient for blocking both electrons and ions, which leads to a constant ion backflow and space-charge distortions of up to 6 cm at 7.5 kHz interaction rate in Pb−Pb collisions.

A first analysis of the position dependence of the distortions in the IROCs already demonstrates that also here, the distortions are caused by space charge in the drift volume as the measured distortions linearly increase with the drift length of the electrons. For such a scenario, the space charge needs to be created by gas amplification at the ROCs from where it drifts back over the full length of the drift volume to the CE. A comparison to space-charge distortions calculated numerically from a space-charge density with the shape of a narrow column along full z at fixed radius and φ confirms the assumption. The shape of the measured distortions in the transverse plane is also qualitatively reproduced by the simulations. With Ar-CO_2, the space-charge distortions increase close to linearly with the interaction rate, although the slope decreases at the largest interaction rates, both in Pb−Pb and pp, and the effect starts to saturate. The size of the distortions can also significantly change when the orientation of the $\boldsymbol{B}$-field is reversed which points towards an asymmetry in φ of the origin of the space charge. The exact dependence on both the interaction rate and the polarity of the $\boldsymbol{B}$-field are individual to each affected sector. The space-charge distortions with Ar-CO_2 are compared to those measured with Ne-based gas mixtures, using reprocessed p−Pb data from Run 1 and pp data from the one year of Run 2 for which the gas was changed back to Ne-CO_2-N_2. Observed differences of the distortions between Run 1 and Run 2 data taken with Ne-based gas mixtures are reduced to the differences in collision systems, collision energies and exact gas composition, concluding that the measurements are in agreement. With Ne-based mixtures, the local space-charge distortions reach only a few mm up to 1 cm at the highest interaction rates in Run 2, which explains why they went unobserved in Run 1. The interaction rate dependence is also significantly different than

with Ar-CO_2 and it can be parameterized with an exponential function. Taking into account only the gas properties, i.e. total ionization and ion mobility, the relative difference in space-charge density between the Ne and Ar-based mixtures should be around a factor of 3.4. An additional difference of 20 % in the density comes from differences in the ROC gain which also affects the amount of ion backflow. Comparing the local space-charge distortions with different gas mixtures at corresponding interaction rates, one finds that the distortions with Ar-CO_2 are larger by about an order of magnitude than those with Ne-based mixtures, significantly exceeding the expectations from simple considerations of gas properties. However, assuming that the positive ions are created via gas amplification within a very narrow region at the ROCs and taking into account the resulting shape of the space-charge density in the form of a narrow column of ions, it becomes clear that the distortions increase not only with the total ionization determined by the interaction rate but also with the space-charge distortions themselves. With increasing space-charge density, electrons from further and further away are focused towards the small region at the ROCs where space charge is created. Therefore, an exponential increase of the distortions is expected, which is confirmed by data taken with Ne. Due to $\boldsymbol{E}\times\boldsymbol{B}$-effects which affect the drift paths of the electrons and their arrival points w.r.t. the region where the space charge is produced, the increase of space-charge density starts to cease at a given point and the dependence of the distortions on the interaction rate becomes linear and starts to saturate.

Studies of the distortions as function of the high voltage applied at the anode wires show an exponential increase of the space-charge distortions with the high voltage. This proves that, indeed, the positive ions are created via gas amplification at the anode wires. The slope of the dependence, however, is much weaker than that of the nominal gain, implying characteristic differences to the nominal gas amplification or additional effects. By switching off the high voltage of every second IROC with either even or odd sector index and measuring the distortions with the adjacent ROCs, it was possible to identify those IROCs responsible for the production of space charge as the distortions disappeared when they were turned off. This confirmed the hypothesis of an φ-asymmetric effect as the origin of the space charge is shifted from the middle between two IROCs towards one chamber. Further measurements show an invariance of the distortions to changes of the GG trigger rate and they validate the full efficiency of the GG in the full TPC, except those regions where it was known before that GG wires are floating. It is finally proven that the space charge is created inside the gap between two IROCs by fitting the measured distortions to a physical model based on a line charge-density. The fit parameters contain the charge density and its position in radial and φ-direction. The φ-position is constant over the full data set which was fitted and it evidently is within the gap for all sectors. Furthermore, it favors the side of the gap facing those IROCs which were identified to be the source of the space charge. The sum of all observations and studies suggests that tips of a single or few anode wires stick out at the outside edge of the ROCs, locally generating high electric fields in which ionization is amplified. This assumption was confirmed in Long Shutdown 2 (2019–2021) when the MWPCs were extracted and surveyed. As there is no structure which blocks electrons from entering or ions from escaping the volume in the gap between two chambers, space charge created there naturally enters the active drift volume of the TPC and distorts the nominal $\boldsymbol{E}$-field. After identifying the origin of the effect, a mitigation strategy is formulated. The cover electrodes are mounted on top of the wire ledges of the ROCs and they are set to the nominal potential of the drift field at their position (-180 V) to minimize static distortions at the chamber boundaries. By changing their potential to more positive values or by applying a bias potential with alternating polarity on adjacent electrodes, the amount of ionization electrons that may enter the volume between two ROCs can be decreased. Therefore, the amount of positive ions created via gas

amplification and escaping into the drift volume also decreases. Electrostatic simulations are performed to systematically study the relative fraction of electrons entering the gap w.r.t. nominal voltage settings as a function of the potential at the cover electrodes. After confirming the desired effect of modified cover-electrode voltages, data with the same settings are taken and they agree well with the simulations within systematic uncertainties. A wide range of possible settings is investigated in simulations and measurements to find the final configuration by minimizing the measured distortions on average. The best results are obtained for $V_{\text{cover}} = +180\,\text{V}$, decreasing the measured space-charge distortions down to 30 %. With the new settings, the distortions in the IROCs were below 1 cm at the highest interaction rates of the final Pb−Pb data taking period of Run 2. As a side effect of the modified cover-electrode voltage, static distortions of the order of a few mm are introduced at the edges of the IROCs. While they are small compared to space-charge distortions and they can be corrected for with high precision, they affect the occupancy and measured charge at the chamber boundaries which has to be accounted for also in Monte Carlo simulations.

The mitigation of the space-charge distortions in the OROC of sector 24 (OROC C06) was more straight-forward than for the IROCs since the origin was known to be ion backflow due to two adjacent floating GG wires. Two approaches were studied and combined in the end. First, the high voltage of the anode wires is decreased in order to decrease the gain and, therefore, the amount of ions drifting back into the drift volume. A decrease of the gain by a factor of two (decrease of the high voltage by 50 V) leads to the corresponding decrease of the space-charge distortions by the same factor. Second, the voltage settings of the GG were adjusted to decrease the transparency for ions. Although two adjacent wires are floating, the potential at the wires next to them still affects the transparency. The ΔV of the GG is increased from the nominal value of 90 V to 120 V to achieve a further 34 % reduction of the distortions. In total, the space-charge distortions in OROC C06 were decreased by more than a factor of 3, down to the order of 1 cm at the highest interaction rate in Pb−Pb collisions.

In summary, by extensively studying the observed space-charge distortions and working out mitigation strategies both in the IROCs and in OROC C06, the fraction of the TPC volume affected by significant space-charge distortions was brought down to a minimum. The early development and application of calibration procedures foreseen for the TPC upgrade allowed to correct the remaining space-point distortions, restoring the intrinsic tracking performance of the detector. For the TPC upgrade in Run 3, even larger space-charge densities in the full phase space of the TPC are expected. The upgrade from MWPCs to readout chambers with GEM foils will introduce constant ion backflow since there is no more mechanism like the GG to prevent amplification ions from entering the drift volume. The upgrade to GEM-based readout enables continuous readout of data without triggers, potentially increasing the amount of data and collected statistics by orders of magnitude. The resulting space-charge distortions are larger than in Run 2 and they cover a significant part of the TPC phase space. In addition, the space-charge density follows fluctuations of event pile-up, multiplicities and charge deposition of particles. The relevant time scales for the calibration in order to account for these fluctuations are of the order of 1–10 ms. Regarding these challenges for Run 3, valuable experience in detector operation with distortions as well as in calibration of space-charge distortions was collected in Run 2. Prototypes of calibration algorithms planned for the TPC upgrade were already implemented and successfully applied in Run 2 but have to be adjusted for the correction of average space-charge distortions in Run 3, since the full readout scheme and many detector sub-systems have also undergone upgrade programs. Furthermore, more complex calibration algorithms are in development to account for fluctuations of the distortions on the level of ms. These algorithms rely on the

parameterization of distortion fluctuations with data-driven physical and machine-learning models, using estimators, extracted from data, for the density fluctuations and the average density as input variables.

Appendix A

ALICE Coordinate System

The global coordinate system of ALICE is illustrated in Fig. A.1. It is a right-handed coordinate system with the origin in the collision point. The z-axis runs along the beam axis and it points away from the muon arm. As the TPC is divided into two sides by the CE, the side with positive z is called A side and the one with negative z is called C side. The x-axis points towards the center of the LHC ring and the y-axis points upwards in order to define a right-handed coordinate system. The azimuthal angle φ in the xy-plane starts at the positive x-axis and it increases counter-clockwise when looking from the A side to the C side. The polar angle θ starts at the positive z-axis and it increases towards the positive y-axis.

Due to the periodicity of the sectors in φ, a local coordinate system is employed in the calibration and reconstruction software. The local coordinate system shares the z-axis with the global coordinate system. The xy-plane is rotated by the angle α so that the local x-axis is in the middle of a given sector (Fig. A.2), pointing outwards along the direction of the pad rows. Consequently, the y-axis points along the direction of the pads in a given pad row. Coordinates or residuals in local y-direction are also denoted as $r\varphi$.

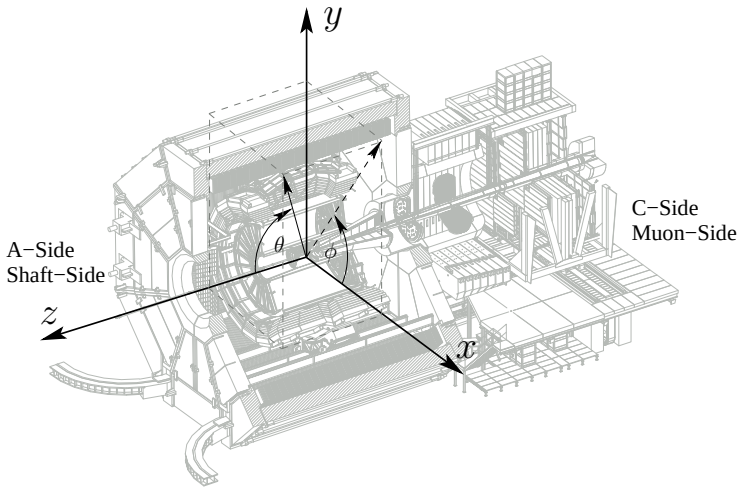

Figure A.1: A sketch of the global coordinate system of ALICE [18].

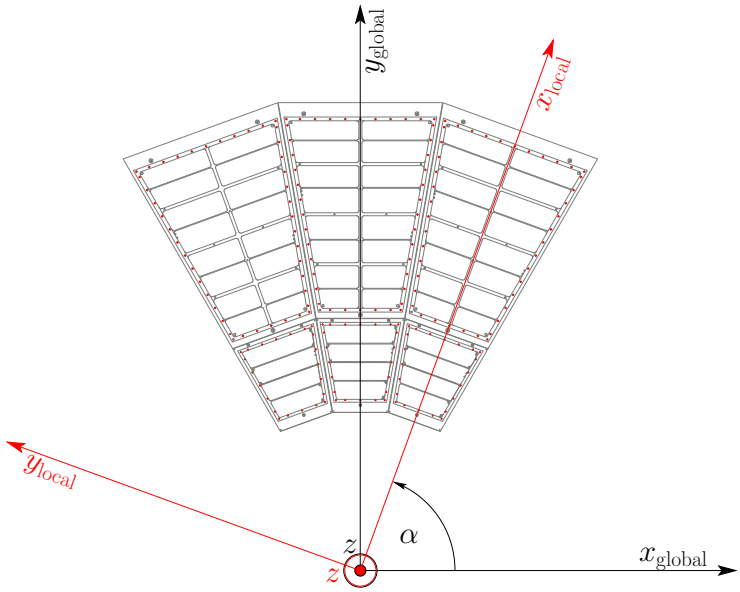

Figure A.2: The local coordinate system (red) employed during calibration and reconstruction is rotated by α so that the x-axis runs through the middle of a given sector [18].

Bibliography

[1] Photos on cover page © 2002-2023 CERN.

[2] ATLAS Collaboration. Observation of a new particle in the search for the Standard Model Higgs boson with the ATLAS detector at the LHC. *Physics Letters B*, 716(1):1–29, 2012. doi:10.1016/j.physletb.2012.08.020.

[3] CMS Collaboration. Observation of a new boson at a mass of 125 GeV with the CMS experiment at the LHC. *Physics Letters B*, 716(1):30–61, 2012. doi:10.1016/j.physletb.2012.08.021.

[4] C. P. Burgess and G. D. Moore. *The Standard Model: A Primer*. Cambridge Univeristy Press, 2007.

[5] J. Bartke. *Introduction to Relativistic Heavy Ion Physics*. World Scientific Publishing Co. Pte. Ltd., 2009.

[6] I. Arsene *et al.* (BRAHMS). Quark–gluon plasma and color glass condensate at RHIC? The perspective from the BRAHMS experiment. *Nuclear Physics A*, 757(1):1–27, 2005. doi:10.1016/j.nuclphysa.2005.02.130.

[7] B.B. Back *et al.* (PHOBOS). The PHOBOS perspective on discoveries at RHIC. *Nuclear Physics A*, 757(1):28–101, 2005. doi:10.1016/j.nuclphysa.2005.03.084.

[8] J. Adams *et al.* (STAR). Experimental and theoretical challenges in the search for the quark–gluon plasma: The STAR Collaboration's critical assessment of the evidence from RHIC collisions. *Nuclear Physics A*, 757(1):102–183, 2005. doi:10.1016/j.nuclphysa.2005.03.085.

[9] K. Adcox *et al.* (PHENIX). Formation of dense partonic matter in relativistic nucleus–nucleus collisions at RHIC: Experimental evaluation by the PHENIX Collaboration. *Nuclear Physics A*, 757(1):184–283, 2005. doi:10.1016/j.nuclphysa.2005.03.086.

[10] ALICE Collaboration. The ALICE experiment – A journey through QCD. 2022. doi:10.48550/arxiv.2211.04384.

[11] ALICE Collaboration. ALICE : Physics Performance Report, Volume I. *Journal of Physics G: Nuclear and Particle Physics*, 30(11):1517–1763, 2004. doi:10.1088/0954-3899/30/11/001.

[12] Lyndon Evans and Philip Bryant. LHC Machine. *Journal of Instrumentation*, 3(08):S08001, 2008. doi:10.1088/1748-0221/3/08/S08001.

[13] J. Letessier and J. Rafelski. *Hadrons and Quark-Gluon Plasma*. Cambridge Univeristy Press, 2005.

[14] Paolo Giubellino. The ALICE detector at LHC. *Nuclear Instruments and Methods in Physics Research Section A: Accelerators, Spectrometers, Detectors and Associated Equipment*, 344:27–38, 1994. doi:10.1016/0168-9002(94)90647-5.

[15] ALICE Collaboration. The ALICE experiment at the CERN LHC. *Journal of Instrumentation*, 3:S08002, 2008. doi:10.1088/1748-0221/3/08/s08002.

[16] ALICE Collaboration. ALICE : Physics Performance Report, Volume II. *Journal of Physics G: Nuclear and Particle Physics*, 32(10):1295–2040, 2006. doi:10.1088/0954-3899/32/10/001.

[17] The ALICE Collaboration. Technical Design Report for the Upgrade of the ALICE Inner Tracking System. Technical Report CERN-LHCC-2013-024, ALICE-TDR-017, 2013. URL: https://cds.cern.ch/record/1625842, doi:10.1088/0954-3899/41/8/087002.

[18] The ALICE Collaboration. Upgrade of the ALICE Time Projection Chamber. Technical Report CERN-LHCC-2013-020, ALICE-TDR-016, 2013. URL: http://cds.cern.ch/record/1622286.

[19] The ALICE Collaboration. Addendum to the Technical Design Report for the Upgrade of the ALICE Time Projection Chamber. Technical Report CERN-LHCC-2015-002, ALICE-TDR-016-ADD-1, 2015. URL: http://cds.cern.ch/record/1984329.

[20] The ALICE Collaboration. Technical Design Report for the Muon Forward Tracker. Technical Report CERN-LHCC-2015-001, 2015. URL: https://cds.cern.ch/record/1981898.

[21] The ALICE Collaboration. Upgrade of the ALICE Readout & Trigger System. Technical Report CERN-LHCC-2013-019, ALICE-TDR-015, 2013. URL: https://cds.cern.ch/record/1603472.

[22] The ALICE Collaboration. Technical Design Report for the Upgrade of the Online-Offline Computing System. Technical Report CERN-LHCC-2015-006, ALICE-TDR-019, 2015. URL: https://cds.cern.ch/record/2011297.

[23] ALICE Collaboration. Upgrade of the ALICE Experiment: Letter Of Intent. *Journal of Physics G: Nuclear and Particle Physics*, 41(8):087001, 2014. doi:10.1088/0954-3899/41/8/087001.

[24] Jerome Jung on behalf of the ALICE Collaboration. Dielectron Production in pp Collisions at $\sqrt{s} = 13$ TeV Measured in a Dedicated Low Magnetic-Field Setting with ALICE. *Proceedings*, 10(1):50, 2019. doi:10.3390/proceedings2019010050.

[25] ALICE Collaboration. First results of the ALICE detector performance at 13 TeV. ALICE-PUBLIC-2015-004, 2015. URL: https://cds.cern.ch/record/2047855.

[26] ALICE Collaboration. ALICE Technical Design Report of the Inner Tracking System. Technical Report CERN-LHCC-99-012, Geneva, 1999. URL: http://cds.cern.ch/record/391175.

[27] ALICE Collaboration. ALICE Technical Design Report of the Time Projection Chamber. Technical Report CERN-LHCC-2000-001, Geneva, 2000. URL: https://cds.cern.ch/record/451098.

[28] ALICE Collaboration. ALICE Technical Design Report of the Transition Radiation Detector. Technical Report CERN-LHCC-2001-021, Geneva, 2001. URL: https://cds.cern.ch/record/519145.

[29] ALICE Collaboration. The ALICE Transition Radiation Detector: construction, operation, and performance. *Nucl. Instrum. Meth. A*, 881:88–127, 2018. doi:10.1016/j.nima.2017.09.028.

[30] ALICE Collaboration. ALICE Technical Design Report of the Time-Of-Flight system (TOF). Technical Report CERN-LHCC-2000-012, Geneva, 2000. URL: https://cds.cern.ch/record/430132.

[31] ALICE Collaboration. ALICE Time-Of Flight system (TOF): addendum to the Technical Design Report. Technical Report CERN-LHCC-2002-016, Geneva, 2002. URL: https://cds.cern.ch/record/545834.

[32] ALICE Collaboration. ALICE Technical Design Report of the High-Momentum Particle Identification Detector. Technical Report CERN-LHCC-98-019, Geneva, 1998. URL: https://cds.cern.ch/record/381431.

[33] ALICE Collaboration. ALICE Technical Design Report of the Photon Spectrometer (PHOS). Technical Report CERN-LHCC-99-004, Geneva, 1999. URL: https://cds.cern.ch/record/381432.

[34] ALICE Collaboration. Performance of the ALICE electromagnetic calorimeters in LHC Runs 1 and 2 and upgrade projects. *JINST*, 15(03):C03025, 2020. arXiv:2001.02928, doi:10.1088/1748-0221/15/03/C03025.

[35] ALICE Collaboration. ALICE Technical Design Report of the Electromagnetic Calorimeter. Technical Report CERN-LHCC-2008-014, ALICE-TDR-14, 2008. URL: https://cds.cern.ch/record/1121574.

[36] ALICE Collaboration. ALICE DCal: An Addendum to the EMCal Technical Design Report Di-Jet and Hadron-Jet correlation measurements in ALICE. Technical Report CERN-LHCC-2010-011, ALICE-TDR-14-add-1, 2010. URL: https://cds.cern.ch/record/1272952.

[37] A. Fernández et al. ACORDE a Cosmic Ray Detector for ALICE. *Nucl. Instrum. Meth. A*, 572:102–103, 2007. arXiv:physics/0606051, doi:10.1016/j.nima.2006.10.336.

[38] ALICE Collaboration. ALICE Technical Design Report of the dimuon forward spectrometer. Technical Report CERN-LHCC-99-022, Geneva, 1999. URL: https://cds.cern.ch/record/401974.

[39] ALICE Collaboration. ALICE dimuon forward spectrometer: addendum to the Technical Design Report. Technical Report CERN-LHCC-2000-046, Geneva, 2000. URL: https://cds.cern.ch/record/494265.

[40] ALICE Collaboration. ALICE Technical Design Report of the Zero-Degree Calorimeter (ZDC). Technical Report CERN-LHCC-99-005, Geneva, 1999. URL: https://cds.cern.ch/record/381433.

[41] ALICE Collaboration. ALICE Technical Design Report of the Photon Multiplicity Detector (PMD). Technical Report CERN-LHCC-99-032, Geneva, 1999. URL: https://cds.cern.ch/record/451099.

[42] ALICE Collaboration. ALICE Photon Multiplicity Detector (PMD): addendum to the Technical Design Report. Technical Report CERN-LHCC-2003-038, Geneva, 2003. URL: https://cds.cern.ch/record/642177.

[43] ALICE Collaboration. ALICE Technical Design Report of the forward detectors: FMD, T0 and V0. Technical Report CERN-LHCC-2004-025, Geneva, 2004. URL: https://cds.cern.ch/record/781854.

[44] G Herrera Corral. Diffractive Physics with ALICE at the LHC: the control of quantum collisions. *J. Phys.: Conf. Ser.*, 624(1):012008. 8 p, 2015. URL: https://cds.cern.ch/record/2159119, doi:10.1088/1742-6596/624/1/012008.

[45] W. Blum, W. Riegler, and L. Rolandi. *Particle Detection with Drift Chambers*. Springer-Verlag Berlin Heidelberg, 2008.

[46] Y. Kalkan, M. Arslandok, A.F.V. Cortez, Y. Kaya, İ Tapan, and R. Veenhof. Cluster ions in gas-based detectors. *JINST*, 10(07):P07004, 2015. doi:10.1088/1748-0221/10/07/P07004.

[47] M. Mager, S. Rossegger, and J. Thomas. The Langevin Equation expanded to 2nd order and comments on using the equation to correct for space point distortions in a TPC. ALICE Internal Note, ALICE-INT-2010-016, 2010.

[48] J. Alme et al. The ALICE TPC, a large 3-dimensional tracking device with fast readout for ultra-high multiplicity events. *Nucl. Instrum. Meth. A*, 622:316–367, 2010. arXiv:1001.1950, doi:10.1016/j.nima.2010.04.042.

[49] ALICE TPC collaboration. The upgrade of the ALICE TPC with GEMs and continuous readout. *Journal of Instrumentation*, 16(03):P03022, mar 2021. doi:10.1088/1748-0221/16/03/P03022.

[50] J. Alme et al. RCU2 - The ALICE TPC readout electronics consolidation for Run2. *JINST*, 8:C12032, 2013. doi:10.1088/1748-0221/8/12/C12032.

[51] A. Deisting, C. Garabatos, and A. Szabo. Ion mobility measurements in $Ar - CO_2$, $Ne - CO_2$, and $Ne - CO_2 - N_2$ mixtures, and the effect of water contents. *Nucl. Instrum. Meth. A*, 904:1–8, 2018. arXiv:1804.10288, doi:10.1016/j.nima.2018.07.008.

[52] M. Arslandok. *Event-by-Event Identified Particle Ratio Fluctuations in Pb–Pb Collisions with ALICE*. PhD thesis, Goethe-Universität Frankfurt, 2017. URL: http://cds.cern.ch/record/2308311.

[53] Y. Belikov, M. Ivanov, K. Safarik, and J. Bracinik. TPC tracking and particle identification in high density environment. *eConf*, C0303241:TULT011, 2003. arXiv:physics/0306108.

[54] I. Belikov, P. Hristov, M. Ivanov, T. Kuhr, and K. Safarik. Track reconstruction in high density environment. In *14th International Conference on Computing in High-Energy and Nuclear Physics*, pages 399–402, 2005. doi:10.5170/CERN-2005-002.399.

[55] Marten Ole Schmidt. Space-point calibration of the ALICE TPC with track residuals. In *24th International Conference on Computing in High Energy and Nuclear Physics*, 2020. arXiv:2003.03174.

[56] H. Bichsel. A method to improve tracking and particle identification in TPCs and silicon detectors. *Nucl. Instrum. Meth. A*, 562:154–197, 2006. doi:10.1016/j.nima.2006.03.009.

[57] Christian Lippmann. Particle identification. *Nucl. Instrum. Meth. A*, 666:148–172, 2012. arXiv:1101.3276, doi:10.1016/j.nima.2011.03.009.

[58] S. Rossegger. *Simulation and Calibration of the ALICE TPC including innovative Space Charge Calculations*. PhD thesis, Technische Universität Graz, 2009. URL: http://cds.cern.ch/record/1217595.

[59] Magboltz - transport of electrons in gas mixtures. URL: http://magboltz.web.cern.ch/magboltz/.

[60] E. Hellbär. Ion Movement and Space-Charge Distortions in the ALICE TPC. Master's thesis, Goethe-Universität Frankfurt, 2015. URL: https://www.uni-frankfurt.de/59428504/Hellbaer_Masterarbeit.pdf.

[61] M. Mager, S. Rossegger, and J. Thomas. Composed correction framework for modeling the TPC field distortions in AliRoot. ALICE Internal Note, ALICE-INT-2010-018, 2011.

[62] H. Appelshäuser, M. Arslandok, C. Garabatos, E. Hellbär, M. Ivanov, C. Lippmann, J. Wiechula, K. Schweda, and R. Shahoyan. Space-charge distortion measurements and their calibration in the ALICE TPC. ALICE Analysis Note, 2018.

[63] S. Rossegger and J. Thomas. Space-charge effects in the ALICE TPC: a comparison between expected ALICE performance and current results from the STAR TPC. ALICE Internal Note, ALICE-INT-2010-017, 2011.

[64] ALICE Software Framework in Run 1 and Run 2. URL: `https://github.com/alisw/AliRoot`.

[65] J. Wiechula. *Commissioning and Calibration of the ALICE-TPC*. PhD thesis, Goethe-Universität Frankfurt, 2008. URL: `http://cds.cern.ch/record/1295506`.

[66] A. Kalweit. *Production of light flavor hadrons and anti-nuclei at the LHC*. PhD thesis, Technische Universität Darmstadt, 2012. URL: `https://tuprints.ulb.tu-darmstadt.de/3063/1/PhDThesis.pdf`.

[67] Jens Wiechula, private communication, 2016.

[68] Marian Ivanov, private communication, 2016.

[69] ALICE Collaboration. Pseudorapidity and transverse-momentum distributions of charged particles in proton–proton collisions at $\sqrt{s} = 13$ TeV. *Phys. Lett. B*, 753:319–329, 2016. `arXiv:1509.08734`, `doi:10.1016/j.physletb.2015.12.030`.

[70] ALICE Collaboration. Multiplicity dependence of the average transverse momentum in pp, p-Pb, and Pb-Pb collisions at the LHC. *Phys. Lett. B*, 727:371–380, 2013. `arXiv:1307.1094`, `doi:10.1016/j.physletb.2013.10.054`.

[71] ALICE Collaboration. Pseudorapidity density of charged particles in p + Pb collisions at $\sqrt{s_{NN}} = 5.02$ TeV. *Phys. Rev. Lett.*, 110(3):032301, 2013. `arXiv:1210.3615`, `doi:10.1103/PhysRevLett.110.032301`.

[72] Marian Ivanov, private communication, 2017.

[73] Chilo Garabatos, private communication, 2019.

[74] Garfield - simulation of gaseous detectors. URL: `https://garfield.web.cern.ch/garfield/`.

[75] A nearly exact Boundary Element Method. URL: `http://nebem.web.cern.ch/nebem/`.

[76] Chilo Garabatos, private communication, 2018.

[77] Marian Ivanov, private communication, 2018.

Acknowledgements

First and foremost, I would like to thank my doctoral supervisor Harald Appelshäuser. You have opened the door to the ALICE TPC for me and you have given me the opportunity to be part of such an exciting project and to work with such an amazing group of people. Thank you for your guidance and supervision, your ideas, your patience and your positive affirmation throughout all those years.

I would also like to thank Christoph Blume who happily agreed to read this thesis as a second reviewer. Furthermore, I am grateful for the discussions with Marcus Bleicher during my HGS-Hire PhD committees, both about the TPC and event-by-event fluctuations. Thank you, Kai and Benjamin, for proof-reading this thesis and giving me your comments and honest feedback. I really appreciate it.

Marianne, Claudia and Sylke deserve a very special and big thank you for their kind and considerate help with all organizational matters.

I would like to thank the TPC group at Frankfurt University, former and present, Jens, Rainer, Michael, Fabian, Matthias, Christoph, and many more. It has been a pleasure to work with all of you on the same project and to have many interesting discussions which have led to new ideas and views. I especially thank Jens, Rainer and Raphaelle for good and funny times in our office. I also thank everybody from the working group in Frankfurt for all the conversations in the hallway, coffees, experiences at conferences, and more, especially Pascal, Mario, Flo, Esther, Basti, Stefan, Behruz and Jerome.

Now let me express my deepest gratitude to Marian and Jens. You have always provided the guidance and help I needed, and you have shared all of your knowledge with me, or at least as much as I could take. You have been a major influence in shaping the technical skill set I have today. For all of this and much more, I would like to thank you from the bottom of my heart. I also thank you, Mesut, for all the time we spent together in Frankfurt, Heidelberg and CERN, working on TPC, Garfield and the analysis of event-by-event fluctuations, and for all the coffees, Falafels and pool matches. I would also like to thank Ruben and Chiara for all their help with the ALICE calibration and reconstruction framework as well as Rob for his willingness to help out with questions about Garfield.

I would like to send a big and very special thank you to the (present and former) colleagues from the TPC team at CERN, especially Christian, Chilo, Robert, Danilo, Alex and Lars, who put their heart into the project so that it can produce so much nice data, as for example those presented in this thesis. Thank you also for all your knowledge you so willingly shared with me.

I also send a big shout-out to Pascal, Mario and Ola for all the fun with Flachwitz- and Falafel-Freitag, and for so much more. Thank you Tim and Alex for being true companions on this scientific journey from day one and for being good friends.

GOETHE
UNIVERSITÄT
FRANKFURT AM MAIN

Publiziert unter der Creative Commons-Lizenz Namensnennung (CC BY) 4.0 International.
Published under a Creative Commons Attribution (CC BY) 4.0 International License.
https://creativecommons.org/licenses/by/4.0/